Modern Topics in scalar field Cosmology

by
Cari Powell

Swansea University
Prifysgol Abertawe

A thesis submitted in fulfillment of the requirements for the degree of Doctor of Philosophy

in the
College of Science
Department of Physics

April 2020

Abstract

College of Science
Department of Physics

Doctor of Philosophy

by Cari Powell

Swansea University
Prifysgol Abertawe

The aim of this research is to use modern techniques in scalar field Cosmology to produce methods of detecting gravitational waves and apply them to current gravitational waves experiments and those that will be producing results in the not too distant future. In the first chapter we discuss dark matter and some of its candidates, specifically, the axion. We then address its relationship with gravitational waves. We also discuss inflation and how it can be used to detect gravitational waves. Chapter 2 concentrates on constructing a multi field system of axions in order to increase the mass range of the ultralight axion, putting it into the observation range of pulsar timing arrays. Chapter 3 discusses non-attractor inflation which is able to enhance stochastic background gravitational waves at scales that allows them to be measured by gravitational wave experiments. Chapter 4 uses a similar method to chapter 3 and applies it to 3-point overlap functions for tensor, scalar and a combination of the two polarisations.

Declaration of Authorship

Declaration

This work has not previously been accepted in substance for any degree and is not being concurrently submitted for a degree.

I, Cari Powell, declare that this thesis titled, 'Multi Field evolution during cosmological inflation' and the work presented in it are my own. I confirm that:

- Where any part of this thesis has previously been submitted for a degree or any other qualification at this University or any other institution, this has been clearly stated.
- Where I have consulted the published work of others, this is always clearly attributed.
- Where I have quoted from the work of others, the source is always given. With the exception of such quotations, this thesis is entirely my own work.
- I have acknowledged all main sources of help.
- Where the thesis is based on work done by myself jointly with others, I have made clear exactly what was done by others and what I have contributed myself.

Signed: [redacted] .....(candidate)

Date: 17/04/2020 .....

Statement 1

This thesis is the result of my own investigations, except where otherwise stated. Where correction services have been used, the extent and nature of the correction is clearly marked in a footnote(s). Other sources are acknowledged by footnotes giving explicit references. A bibliography is appended.

Signed: [redacted] .....(candidate)

Date: 17/04/2020 .....

Statement 2

I hereby give consent for my thesis, if accepted, to be available for photocopying and for inter-library loan, and for the title and summary to be made available to outside organisations.

Signed: [redacted] .....(candidate)

Date: 17/04/2020 .....

Acknowledgements

This thesis and the completion of my PhD would not be possible without the help of the following people:

My supervisor Dr. Gianmassimo Tasinato for all of his guidance throughout the course of my PhD *"Grazie di tutto, Gianmassimo."*

My advisor Prof. Graham Shore for his continued support and invaluable advice.

My friends and family for their constant love and support.

David - for keeping me sane throughout my three degrees and for many years to come!

All the PhD physics students I've met during my time in Swansea, I couldn't have asked for better people to share offices with.

Contents

List of Figures

List of Tables

Dedicated to my late Grandmother Joyce Kemeys.
"I did it, Gran!"

Chapter 0

Introduction

The observable Universe is only 5% of the total content of the Universe and only 20% of its mass. The rest of its mass is made of invisible matter known as Dark Matter, which, is one of the greatest mysteries of the Universe. Although, it has not yet been detected we are aware of its existence through the observation of its gravitational effects, i.e. the rotation of galaxies. Despite its composition being, as of yet, unknown there are many candidates that have been proposed and are currently being searched for by various experiments. One of the most popular is from beyond the Standard Model, a hypothetical particle known as the axion. An example of this particle is the cosmological ultralight axion. It is able to resolve some of the issues surrounding cold dark matter which makes it a prime candidate. It can be detected indirectly through the detection of gravitational waves.

In this Thesis we study modern topics in scalar field cosmology, focusing on axions and a specific model of inflation and how both are involved in the production of gravitational waves which then can be detected by experiments.

In the first chapter we discuss dark matter and some of the possible candidates from the standard model and beyond. We concentrate on a hypothetical pseudoscalar called the axion explaining how it is a viable dark matter

candidate. The detection methods for the particle are then explored, this includes direct detection where the axion would decay into a pair of photons which can then be observed by the experiment. Indirect detection is also discussed which indicates that axions act like a pressureless dust and they are able to produce their own gravitational oscillations which are then detected by gravitational wave experiments such as LIGO and pulsar timing arrays. From here, we move on to discussing inflation and how it alleviates the major problems that are associated with the Big Bang Theory. This then, leads into describing how inflation can be involved in the detection of gravitational waves.

The second chapter consists of unpublished work. This concentrates on constructing a multi field system of axions in order to increase the mass range of the ultra light cosmological axion. An uncoupled system of two pseudoscalars is explored first before moving on to a coupled system. Finally, an attempt is made to model magnetised ultra-light dark matter by formulating a coupled system which couples dark matter and dark energy. As mentioned previously, axions are able to induce gravitational oscillations of their own which may allow them to be detected by pulsar timing arrays and increasing the mass of the axion which would allow it to enter the observation range of these experiments.

Chapter 3 consists of the paper [1] in which we discuss a specific type of inflation, dubbed as non-attractor inflation, which is a mechanism that enhances and amplifies the stochastic background primordial gravitational wave at frequencies and scales which allows them to be detected by interferometers and pulsar timing arrays. Moreover, non-attractor inflation also amplifies gravitational wave non-Gaussianities. This allows us to understand the early universe and the beginning of the creation of the large scale structures which exist in the universe today.

In Chapter 4, which consists of the paper [2], we introduce the concept of stationary graviton non-Gaussianity (nG), an observable that can be

probed in terms of 3-point correlation functions of a stochastic gravitational wave (GW) background. When evaluated in momentum space, stationary nG corresponds to folded bispectra of graviton nG. We determine 3-point overlap functions for testing stationary nG with pulsar timing array GW experiments, and we obtain the corresponding optimal signal-to-noise ratio. For the first time, we consider 3-point overlap functions including scalar graviton polarizations (which can be motivated in theories of modified gravity); moreover, we also calculate 3-point overlap functions for correlating pulsar timing array with ground based GW detectors. The value of the optimal signal-to-noise ratio depends on the number and position of monitored pulsars. We build geometrical quantities characterizing how such ratio depends on the pulsar system under consideration, and we evaluate these geometrical parameters using data from the IPTA collaboration. We quantitatively show how monitoring a large number of pulsars can increase the signal-to-noise ratio associated with measurements of stationary graviton nG.

In our Conclusions, we summarise all of our main results, we discuss them critically and we highlight possible directions for future research.

Chapter 1

The Production of Gravitational Waves

In this chapter we discuss a possible dark matter candidate; hypothetical particles known as axions, and how they could possibly produce gravitational waves. We also discuss how gravitational waves could be produced via inflation.

1.1 Dark Matter and Axions

As we are aware, the visible Universe is only 5% of the total content of the Universe, and 20% of the total mass. The other 80% is comprised of unseen, or invisible matter, dubbed "Dark Matter" by Fritz Zwicky in his paper *On the Masses of Nebulae and Clusters of Nebulae* [3]. Although we have not been able to detect it directly we are aware of its existence due to its gravitational effects. A prime example of this involves the rotational velocity of galaxies. If galaxies were only made of visible matter, as the distance from the center of the galaxy increased, the orbital velocity of matter would decrease. However, the velocity in fact remains relatively constant after initially increasing with distance from the centre of the galaxy.

Despite knowing that dark matter exists, from gravitational effects, its composition is still a great cosmological mystery. Many candidates have been proposed as a solution to dark matter, including MACHOs (Massive Compact Halo Objects). MACHOs are composed of visible matter but reflect little to no light, therefore they can be considered as dark matter candidates. Types of MACHOs include: neutrons stars, white dwarfs, brown dwarfs [1]. They can be detected as the result of gravitational lensing. When light from a distant star passes near the MACHO the large gravitational pull of the object bends the light and focuses it towards the observer on Earth. This causes a sudden brightening of the distant star. The issue with this candidate is that they are not abundant enough as they consist of visible matter, which, as we know, is only 20% of the mass of the Universe. In order to find more appropriate candidates we need to look beyond the Standard Model. One of the most popular solutions are called WIMPS (Weakly Interacting Massive Particles) which are hypothetical particles that have masses in the range of $10 - 10^4 GeV$ (which makes them of the order or a couple of orders larger than the proton). They do not interact with the electromagnetic force, which explains why they appear to be largely invisible in space. WIMPs interact with the weak force and the gravity of surrounding matter. They can be detected as they interact with charged particles on the Earth and recoil to create photons. Despite them being such a strong candidate, WIMPs have not, as yet, been detected.

The standard model (SM) of particle physics is not a complete theory of nature as it does not include gravitational interactions (as described by General Relativity (GR)) so it must be extended or embedded in another theory. This was the state of the SM a few decades ago, since then other issues have appeared from observations of the Universe from cosmology which are not part of the SM and cannot be explained by it. They are however explained well by Einstein's GR. It describes the Universe as expanding homogeneously, arising from primordial inhomogeneities and these

[1] Sometimes known as failed stars. They have not undergone nuclear fusion as there is not enough mass for the process to start

grew out of tiny quantum fluctuations caused by the accelerated expansion that occurred within the first second of the existence of the Universe. This process is known as inflation [4]. For these conditions to occur, then particles which are not part of the SM are required, this includes Dark Matter - it acts as cold gas made of weakly interacting particles, when under gravity. There is also Dark Energy which tends towards Einstein's cosmological constant, Λ. As well as this a new field is also needed whose potential energy drives inflation before turning into the radiation that dominates the energy density of the Universe during the process of Big Bang Nucleosynthesis. Of these elements, Dark Matter is the most important in the process of finding a new species of particle. It has been demonstrated that the majority of dark matter is comprised of something which is not part of the SM (e.g. abundance of MACHOs as mentioned above) [5].

There are other reasons that suggest that SM is not a complete theory of nature. This includes the lack of symmetry that the could be rectified at high energy scales. Examples of which include the grand unification theory (GUT). The couplings can be related at high energy scales but lose their unified character at low energies because they run with the energy scale. High energy scales seem to be of more importance in finding new physics. However, if this is above the electroweak scale, it would be difficult to reach these scales with future accelerators. Yet, some of these high energy mechanisms also have important consequences at low energy scales. An essential example of this, gravity (which is associated with physics at the Planck scale) has considerable effects at low energy scales. Other examples include the neutrino and the role of other particles in astrophysics and cosmology. The small masses of these particles, as compared with the electroweak scale, avoid the hierarchy problem because the quantum corrections made to their masses are protected by symmetries. Therefore this gives us a reason to look at low mass particles which are associated with symmetries at high energies and the effects these particles have on cosmology, in astrophysics, and in experiments at high intensity, precision frontier

[5]. This is discussed as the *low energy frontier of particle physics* in [6].

A good example of a new physics at the low energy scales is the QCD axion which was proposed by Roberto Peccei and Helen Quinn [7–11] as a solution for the strong Charge-Parity (CP) problem of the SM (the absence of CP violating terms in strong interactions). In [9, 10] the axion was identified as a pseudo Nambu Goldstone boson of a new spontaneously broken global symmetry that Peccei and Quinn had postulated (known PQ symmetry). The axion mass, m_A is inversely proportional to the symmetry breaking scale, f_A. This means that the larger the value of f_A, the smaller m_A, resulting in weaker couplings. The first axion models proposed by [9, 10] gave values of f_A at the order of the electroweak scale which were swiftly ruled out by experiments. It was soon discovered that the f_A had the possibility of corresponding to a much higher energy scale which results in very weakly coupled, dubbed *invisible* axions [5].

Pseudo Nambu Goldstone bosons can be embedded in extensions of the SM at high energies by invoking new fields and symmetries. The PQ mechanism can also be embedded, easily, into supersymmetry (SUSY) [12], GUTs[13] and string theory in a way that is model-independent [14, 15]. This predicts the existence of many axion-like particle (ALP), candidates, which include the QCD axion, however other ALPs could be useful in a phenomenological capacity [16].

The phenomenology of axions and ALPs are determined by their low mass, very weak self interactions and their interactions with gravity. They could affect the evolution of stars [17, 18] and cosmology [19] behaving in a similar way to thermal neutrinos (neutrinos are classed as weakly interacting sub-eV particles or WISPs). As a result of these effects, there is a constraint put on the symmetry breaking energy scale $f_A \gg 10^7$ GeV. Despite this constraint, they could potentially be detected at the low-energy, high intensity frontier as they could mediate new long range forces [20]. This includes allowing rare decays to occur which would appear after passing

through thick walls during a beam-dump experiment (this is known as the *light-shining-through-walls* (LSW) experiment) [21]. They could also be produced thermally in large amounts inside the Sun which then could be detected on Earth [22]. Consequently, we can see that the axion would make an excellent candidate for dark matter. They are weakly interacting particles, they are mainly produced non-thermally in the early Universe, via the vacuum realignment mechanism [23–25] and the decay of topological defects (axion strings and domain walls) [26, 27]. They are particles produced with tiny dispersion velocities which means that we have *very* cold dark matter fitting neatly into the requirements of the ΛCDM model that accurately describes large scale structures of the Universe [5].

Most particle physics experiments involve accelerators and high energy collisions which caused the exclusion of the first electroweak-scale axion models. The large values of f_A needed in order to prevent astrophyscial and cosmological bounds made it essentially impossible to detect the axion with these types of experiments. This problem was addressed by two techniques that were proposed in [22] by Peter Sikivie for the search for invisible axions: *axion helioscopes* which detect large amounts of axions emitted from within the Sun and the *axion haloscopes* which were proposed to detect axions from the dark matter halo that surrounds galaxies. As a consequences of the exceedingly large fluxes of natural axions, haloscopes and helioscopes are far more sensitive to axions and ALPs than laboratory experiments [5]. We discuss these experiments in more detail in the next section.

The QCD Lagrangian violates charge conjugate parity symmetry

$$\mathcal{L}_{\theta\,QCD} = \frac{\theta_{QCD}}{32\,\pi^2} Tr\, G_{\mu\nu}\,\tilde{G}^{\mu\nu}. \tag{1.1.1}$$

where G is the gluon field strength tensor, $\tilde{G}^{\mu\nu} = \epsilon^{\alpha\beta\mu\nu}\,G_{\alpha\beta}$ is the dual and the trace runs over the colour $SU(3)$ indices [28]. This produces CP-violating interactions such as the neutron electric dipole moment (EDM), d_n, which is computed in [29] to be

$$d_n \approx 3.6 \times 10^{-10}\, \theta_{QCD}\, e\, cm, \tag{1.1.2}$$

where d_n is the charge on the electron. The permanent, static dipole moment is constrained to $|d_n| < 3.0 \times 10^{-26}\, e\, cm$ (with a 90% confidence level) [30], implying $\theta_{QCD} \lesssim 10^{-10}$.

If there were only strong interactions which are CP-conserving then the θ_{QCD} term could be set to zero by symmetry. In reality there are also weak interactions to take in to consideration which violate CP [31].

Axions are pseudoscalar particles which were devised as the solution to the strong CP problem in quantum chromodynaics by R.D. Peccei and Helen R. Quinn [7] (as well as Weinberg [9] and Wilczek [2] [10]). The axion field replaces the theta parameter in the QCD Lagrangian by a dynamical quantity, $\theta_A(x) = \frac{A(x)}{f_A}$ relaxes spontaneously to zero, $< \theta_A >= 0$ thus describing why CP violation is not observed. [7–11]. Axions have a shift symmetry:

$$\phi \to \phi + \text{const.}, \tag{1.1.3}$$

This makes the axion field massless to all orders of perturbation theory [32].

There are types of axions, other than the QCD axion [7–11, 23–25, 33–38], lighter axions can be used in cosmology. For certain regimes they affect the expansion rate of the Universe and the growth rate of cosmological perturbations [39]. These ultra-light ($10^{-33}\, eV < m_A < 10^{-22}\, eV$), stable axions or axion-like particles (ALPs) which interact weakly with the SM are potential cold dark matter candidates [28, 40, 41]. The reason for this particular mass range for dark matter is that, at a larger mass range, tuning would be needed which results in not enough dark matter being produced and if the mass range was smaller there would still be tuning needed as there would be too much dark matter (anthropic principle). As a result it

[2] Wilczek named the particle the 'axion' after a famous detergent.

is the only mass range which gives *invisible* axions. It also confirms with the value of $|\theta|$ given by the Strong CP Problem. ALPs have no couplings to gluons, however, they do have a non-zero coupling to photons. In the case of this non-zero coupling, the axion mass (m_A) is independent of the scale of symmetry breaking (f) [42–44]. Ultra-light scalar fields can resolve the problems with cold dark matter (ΛCDM) on sub-galactic scales (Fuzzy Cold Dark Matter) [45].

Axion are produced via the misalignment mechanism or vacuum realignment. This is dependent on the axion field being associated with spontaneous symmetry breaking and being a pseudo Nambu Goldstone Boson [32]. The homogeneous mode of the axion field is frozen at some random initial value, $A(t_i) = \theta_i f_A$, resulting from cosmic expansion. This is true as long as time (t) $t \lessapprox \frac{1}{m_A}$. At later times, $t > \frac{1}{m_A}$, the axion field oscillates around zero [23, 25, 46]. Cold axions can be produced by two other methods: string decay [26, 47–56] and domain wall decay [27, 56, 57].

There are two main criteria that axions need to satisfy to be seen as a viable dark matter candidate [58]. In order for axions to be observed through cosmological effects they must have a prominent effect on the energy density of the Universe. Since cosmological axions have such small masses there must therefore be a large number (non-relativistic population) of them to achieve this [32]. Due to this larger occupation number, the collection of ultra-light dark matter particles take on the behaviour of a classical scalar field [59]. Axions can be considered effectively collisionless. This means the only collisions that occur are significantly long range and gravitational [58].

Axions meet these criteria naturally without the need for additional modifications. They are cold, non-baryonic particles that couple extremely weakly to normal matter, and are dominated by gravitational forces. It is predicted that the axion forms a Bose-Einstein condensate and this could, potentially, distinguish it from other cold dark matter candidates through

their phase space structure (galactic halo dark matter), as supported by astronomical observation.

1.1.1 Direct detection Methods

Since axions have become a popular dark matter candidate there are many experiments which are currently searching for them and more have been proposed for the future. The past couple of decades have been very fruitful in the the arena of axion detection experiments and the fact that WIMPs have not been detected by underground detectors, has contributed to the increased interest in axions in recent years [5]

As mentioned previously, axion haloscopes are one such type of experiment. These includes the Axion Dark Matter eXperiment (ADMX) at the University of Washington [60, 61] and The Haloscope at Yale Sensitive to Axion Cold dark matter (HAYSTAC) at Yale University[62–66]. ADMX contains a strong magnetic field which aims to convert dark matter axions into microwave photons which can be detected. The magnetic field is produced by a large superconducting magnet housed within a resonant microwave cavity. If the photon's frequency corresponds to the cavity's resonant frequency then the conversion rate is enhanced. There is also a competing haloscope in Kyoto, Japan named CARRACK (Cosmic Axion Research with Rydberg Atoms in resonant Cavities in Kyoto)[5].[3]

Axion helioscopes including the Tokyo Axion Helioscope based at the University of Tokyo [67–76], CERN's helioscopes, CAST (CERN Axion Solar Telescope) [77] and IAXO (International Axion Observatory). Their purpose is to detect axions that are produced in the solar core [78–81]. CAST uses a 9 T (Tesla) test magnet from the Large Hadron Collider which is

[3]In Italy there is a Fabry-Perot optical cavity experiment PVLAS (Polarizzazione del Vuote con LASer (Polarization of the vacuum with laser)) used to test quantum electrodynamics and aims to detect dark matter, including axions.

directed towards the Sun. The strong magnetic field converts the solar axions into x-ray photons that can be recorded by X-ray detectors.

The Xenon experiments (Xenon10, Xenon100 and Xenon1T) operating from the Italian Gran Sasso National Laboratory [82–84] and LUX (Large Underground Xenon) [85, 86] operating at Sanford Laboratory are experiments with xenon nucleus active targets. Cosmic rays hit the earth, not all are able to travel through the rock to reach the xenon experiments. The axions reach the xenon which causes the electrons to recoil leaving us with photons.

LSW ("Light shining through a wall") experiments such as Any Light Particle Search (previously ALPS I (2007-2010) and now II (2013 - present)) based at DESY (Deutshches Elektronen-Synchrotron which is a research centre of the Helmholtz association) are looking for WISPs (Weakly interacting sub-eV particles) of which the axion is the most famous [87–94]. LSW experiments consists of light from a strong laser being shone inside an optical cavity into a strong magnetic field. The light then can be converted into WISPs in front of a light-blocking barrier (production region) before being reconverted into photons behind the barrier (regeneration region).

The above experiments involve the direct detection of axions. There are other ongoing experiments which could, potentially, be used to detect them indirectly. Axions could possibly produce their own gravitational oscillations so it may be possible to detect them in the same way as gravitational waves are currently being detected.

1.1.2 Indirect detection methods

It has been suggested that axions, or in a more general sense, pseudoscalars could be detected through the use of pulsar timing arrays [95]. The motivation for this detection method arose from observations of pulsars by telescopes (Pulsar Timing Arrays (PTAs)). They rotate with very precise

periods of the order of milliseconds, however what the PTAs observe is a frequency shift when photons from the pulsars reach the detector. The question is what causes this? The main suspect is gravitational waves. The entirety of spacetime is filled with background gravitational waves which are the product of large astrophyiscal events such as two massive merging black holes. However, the suggestion made by Rubakov and Khmelnitsky [95] is that the gravitational oscillations that cause the frequency shift of the pulsar observations are, in fact, due to axions. They state that the axion (ultra-light non-interacting dark matter) behaves as a perfect fluid with oscillating pressure, which averages to zero at time scales greater than the oscillation period, and is usually treated as a pressureless dust. However, it seems to have been overlooked that the oscillations produced by the axions induce oscillations in gravitational potentials, that are, in principle, observable.

In their paper [95] they show the pulsar timing signal for scalar field dark matter for a range of scalar masses.

Pulsar timing arrays experiments are conducted throughout the world. These include the European Pulsar Timing Arrays (EPTA) [4] which along with the Parkes PTA [96] in Australia and NANOGrav (North American Nanohertz Observatory for Gravitational Waves) [5] make up the International PTA and the Five hundred metre Aperture Spherical Telescope (China). In the near future (building will take place within the next decade) the Square Kilometre Array (SKA) based in Australia and South Africa will also be taking data [97].

[4] which consists of Effelsberg Radio Telescope in Effelsberg, Germany, Nançay Decimetre Radio Telescope in Nançay, France, Lovell Telescope in Cheshire, England, Sardina Radio Telescope in Sardina, Italy and Synthesis Radio Telescope in Westerbork, the Netherlands.

[5] which is comprised of the Aricebo (Puerto Rico) and Green Bank Telescopes (West Virgina, USA)

Axion could also be detected by interferometers such as LIGO (Laser Interferometry Gravitational-Wave Observatory) and LISA (Laser Interferometer Space Antenna) if they are able to sufficiently deform the arms of these experiments. If the signal is too weak to do this effectively a solution can be found to rectify the problem [98].

Axion interferometry [42, 99]. The effect of axion dark matter is to change the velocity of circularly polarised light. Therefore, the natural solution is to build an interferometer where one arm has only left circularly polarised light and the other has right. The presence of axion dark matter would produce a difference in phase velocity between the two arms, thus generating an interference pattern. Extra wave plates can be added to Michelson interferometers to preserve polarisation. The same paper also proposed an interferometer where the same mirrors are used to form both cavities. Two quarter wave plates and a half wave plate are used to maintain circular polarisation of light [42].

The plots below show the differences between axion and gravity interferometers.

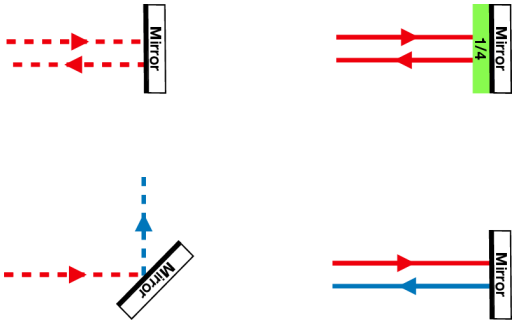

FIGURE 1.1: *Left: Reflections from mirrors between axion interferometers. Right: The same with gravity wave interferometers. [42].*

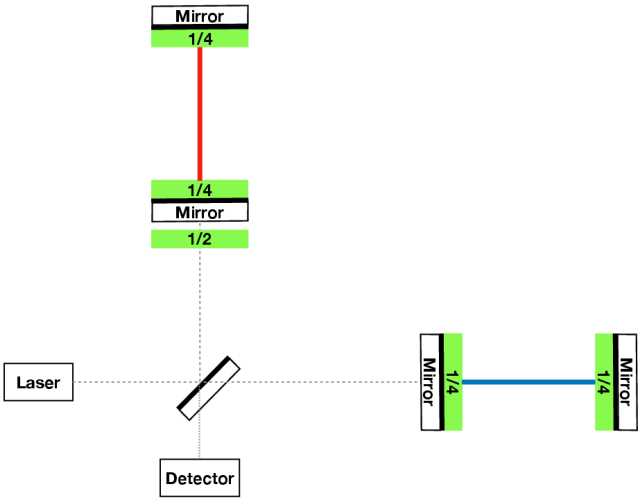

FIGURE 1.2: *Proposed alterations to a Michelson interferometer in order to observe axion oscillations [42].*

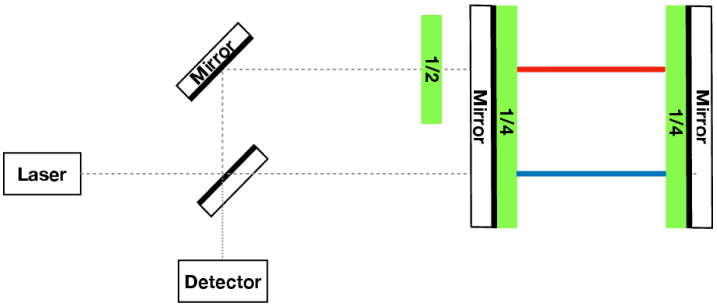

FIGURE 1.3: *Proposed axion interferometer where the same mirror is used to form both cavities. Red line indicates left circular polarised light and blue is right circular polarised light. In order for the circular polarised light to be maintained, two quarter waveplates are added. The dashed lines indicate linearly polarised light and the coloured lines are circularly polarised light. Before the large mirror a half waveplate is added in order to change the handedness of the light giving both left and right circularly polarised light [42].*

In the 2030s we expect to be able to observe pulsar timing arrays using the space interferometer LISA (Laser Interferometer Space Antenna) which consists of three spacecrafts which will each sit at a Lagrange point between the Earth and the Sun arranged in a triangle. The arms are 2.5 million kms in length A mirror is contained within each spacecraft. LISA's observational range lies between that of the ground based interferometers and

the telescopes used for the PTA experiments (10^{-4} - 10^{-1} Hz). As a result many more gravitational waves can be detected [98].

Superradiance is the process whereby a wave which scatters from a rotating black hole is able to escape its environment with a larger amplitude than that of the incoming wave. This type of amplification happens for matter and light waves.[100][101]. Supposing that an axion field exists around a rotating black hole, some of the field would be absorbed by the black hole but an "axion cloud" would be created as the axion field forms a quasi-bound state [102]. If the axions are close to but do not cross the event horizon the black hole's spin will cause the particles to receive a boost of energy. As the axion is a quantum particle the boost will create more axions. This process could generate a vast number of particles. As a quantum particle, it is also able to act like a wave and as it is a light particle, it has a very long wavelength. The wavelength of the axion is required to be the same width as the black hole in order for superradiance to occur. There are a few ways in which axions could be seen from this mechanism. The most likely outcome involves the collisions between axions within the cloud annihilating one another and creating gravitons which could then be detected as gravitational waves by interferometers such as LIGO, VIRGO (named after the Virgo Cluster[6]) and KAGRA (Kamioka's Gravitational-Wave Detector).

In these two sections we discussed axions as a suitable dark matter candidate considering how they are an alternative to other particles such as WIMPS. We then moved on to discussing how axions could possibly be detected (both directly and indirectly) and how, via indirect detection methods, axions may be able to produce gravitational waves.

Gravitational waves (more specifically primordial gravitational waves) could also be produced, in this case via inflation which we will discuss in the next sections. We begin with a recap on inflation then we move on to discuss an

[6]Which is found in the Virgo constellation.

inflationary model which enhances and amplifies primordial gravitational waves thus enabling detectors to observe the early Universe.

1.2 Inflation

Some of this section is taken from [103] which I submitted in fulfilment of the requirement for the degree of Master of Science.

1.2.1 The Problems with Big Bang Cosmology

The SM of the Big Bang is very successful, but does not address the Horizon and Flatness Problem [4]. The Horizon problem relates to how the Universe appears to be homogeneous and isotropic on large scales. Different regions of space have approximately the same temperature and density, which is not explained by the Big Bang theory. The Flatness problem comes from the observation that the total density of the Universe is approximately one, which means that it appears to be spatially flat [4] [104].

1.2.1.1 The Horizon Problem

The horizon problem comes from the existence of the particle horizon in Friedmann-Robertson-Walker cosmology. There is a finite amount of time since the Big Bang singularity and, therefore, a finite distance that photons travel during the lifetime of the Universe. This is the reason why the Horizon exists [105]. Observationally, microwave photons, which are emitted from opposite ends of the sky, appear to be in thermal equilibrium at almost the same temperature. As the horizon is a finite size, there is no time for these regions to interact before the photons are emitted. These two patches of sky could not have originated from the same point and are therefore not in causal contact. Hence the SM cannot explain why

the temperature is correlated. Big Bang Cosmology cannot explain this phenomenon however, inflation resolves this problem by stating that the present Universe looks spatially flat.

The Friedmann-Robertson-Walker metric is defined as follows:

$$\boxed{ds^2 = -dt^2 + a^2(t)\left[\frac{dr^2}{1-k\,r^2} + r^2\left(d\theta^2 + \sin^2\theta\, d\phi^2\right)\right],} \tag{1.2.1}$$

where $a(t)$ is the scale factor, κ is the curvature parameter, r,θ,ϕ are coordinates which in the case of this equation are comoving coordinates. When κ has a value of $+1$ for positive curvature, $\kappa = 0$ is the flat spacetime and $\kappa = -1$ is a negative curvature.

From the metric we arrive at the following equation:

$$\int_{t_*}^{t_{dec}} \frac{dt}{a\,(t)} \ll \int_{t_{dec}}^{t_0} \frac{dt}{a\,(t)}. \tag{1.2.2}$$

where t_{dec} is the time when decoupling occurs (when the CMB was formed), t_0 is present time and t_* is the initial time at which the light began to travel (Big Bang).

(1.2.2) shows that the distance light travels before the CMB is released is much smaller than the present horizon distance. Any regions that are separated by more than approximately 2 degrees in the sky today are causally separated at decoupling in the Big Bang theory [106, 107]. There is no explanation in the Big Bang theory detailing why the Universe appears to be homogeneous (same in all locations) [108]. Also it does not explain how the Universe is also isotropic (same in all directions). So, the horizon problem states that, in standard cosmology, there is no physical explanation as to why the Universe appears to be smooth on large scales [109, 110].

The second integral in (1.2.2) is known as the particle horizon (distance photons can travel in between two times (t_0 and t)) which can also be

written in terms of conformal time τ. Conformal time is defined as:

$$\tau = \frac{dt}{a}$$

$$\chi_{ph}(\tau) = \tau - \tau_0 = \int_{t_0}^{t} \frac{dt}{a(t)}, \tag{1.2.3}$$

where χ_{ph} is the conformal particle horizon, τ is the conformal time at the time of the Big Bang and τ is the conformal time at the present time of the Universe.

The particle horizon can be rewritten as follows:

$$\chi_{ph}(\tau) = \int_{t_0}^{t} \frac{dt}{a(t)} = \int_{a_0}^{a} \frac{da}{a\dot{a}} = \int_{ln\, a_0}^{ln\, a} (a\,H)^{-1} d\, ln\, a, \tag{1.2.4}$$

where $(a\,H)^{-1}$ is the comoving Hubble radius, $a_0 = 0$ corresponds to the Big Bang singularity. We can link the causal structure of spacetime to the comoving Hubble radius. Assuming that the equation of state $\omega = \frac{p}{\rho}$

$$(a\,H)^{-1} = H_0^{-1}\, a^{\frac{1}{2}(1+3\omega)}, \tag{1.2.5}$$

where H is the Hubble parameter as a function of time and H_0 is the Hubble parameter at present time. In standard cosmology $\chi_{ph} \simeq (a\,H)^{-1}$. We can therefore, refer to the particle horizon and the Hubble radius as the "Horizon".

Approximately 380,000 years after the Big Bang, the Universe cooled. This allowed hydrogen atoms to be formed and the decoupling of primordial plasma, which is known as the Cosmic Microwave Background (CMB). We are able to observe it thanks to the Wilkinson Microwave Anisotropy Probe (WMAP) and the Planck satellites [111].

During our description of the horizon problem we haven't addressed the issue of the increasing Hubble sphere in Big Bang cosmology. We can therefore suppose that in the early Universe we are using a decreasing

Hubble radius,

$$\frac{d}{dt}(a\,H)^{-1} < 0. \tag{1.2.6}$$

Essentially, the horizon problem boils down to the fact that the CMB is isotropic to a high level of precision even though widely separated points on the last scattering surface are completely outside each others' horizons [112].

Inflation is a period of accelerated expansion of the Universe which occurred within the first second following the Big Bang. Before inflation took place, regions that are now more than 2 degrees apart were in causal contact [111]. Causal physics is able to produce a large smooth thermalised region, encompassing a volume, which is far in excess of the present observable Universe. Causal processes are also able to generate anisotropies in the Universe on large enough scales as to exceed the present observable Universe [108].

1.2.1.2 The Flatness Problem

The flatness problem originates from considering the Friedmann equation in the following form:

$$|\Omega - 1| = \frac{|k|}{H^2\,a^2}, \tag{1.2.7}$$

where Ω is the total density parameter, a is the scale factor and H is the Hubble parameter. Differentiating by the scale factor causes the equation to becomes:

$$\frac{d\Omega}{da} = (1 + 3\,\omega)\,\frac{\Omega\,(\Omega - 1)}{a}. \tag{1.2.8}$$

The density parameter is approximately equal to 1 [112]. During the evolution of the Universe, a^2H^2 is decreasing so Ω moves away from 1:

$$\text{Matter domination}: |\Omega - 1| \;\alpha\; t^{\frac{2}{3}},$$
$$\text{Radiation domination}: |\Omega - 1| \;\alpha\; t.$$

So $\Omega = 1$ is a critical point. Since Ω today is within an order of magnitude of 1 so it must have been much closer in the past. The total density is defined as follows:

$$\Omega = \Omega_m + \Omega_d + \Omega_\Lambda, \tag{1.2.9}$$

where Ω is the total density parameters, Ω_m is the matter density parameter, Ω_d is the dark matter density parameter and Ω_Λ is the dark energy density parameter.

The WMAP satellite determined precise values for these cosmological parameters.

Parameter	**WMAP parameter**	**What is it?**
Ω	1.02 ± 0.02	total density
Ω_Λ	0.73 ± 0.04	dark energy density
Ω_d	0.27 ± 0.04	dark matter density
Ω_m	0.044 ± 0.004	matter density

TABLE 1.1: Values of density parameters determined by WMAP [113]

Planck has produced more accurate results for these parameters in 2013 [114, 115] then again in 2015 [116, 117].

In terms of spacetime curvature, the early Universe is incredibly close to being flat.

$$\begin{aligned} \text{nucleosynthesis}\,(t \approx 1\,\text{sec}): \ |\Omega - 1| \ &< \ \mathcal{O}\,(10^{-16}), \\ \text{electro-weak scale}\ (t \approx 10^{-11}\,\text{sec}): \ |\Omega - 1| \ &< \ \mathcal{O}\,(10^{-27}), \end{aligned}$$

The value of Ω has important implications. Either the Universe will swiftly re-collapse, or will rapidly expand and cool below $3K$ within its first second of existence [108].

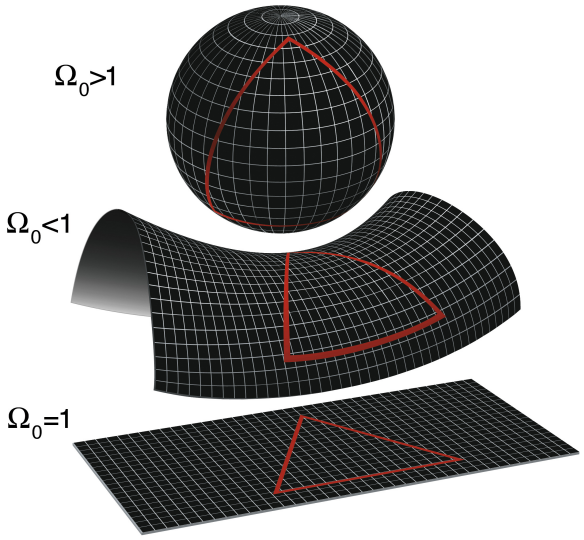

FIGURE 1.4: Curvature of the Universe for different values of Ω. $\Omega > 1$ is the Universe with a positive curvature which is the case where the Universe will expand forever, $\Omega < 1$ is the negative curvature where the Universe will collapse in on itself and $\Omega = 1$ is a flat Universe which represents our Universe [4].

The problem with the hot Big Bang model is that aH is always decreasing. This causes Ω to deviate from 1.

1.2.1.3 Inflation

Inflation solves these problems. In cosmology, inflation is defined as the rapid expansion that took place in the early Universe at high energy $\ddot{a} > 0$ [104, 108]. This acceleration leads to the expansion of a small region of space to enormous scales, diminishing spatial curvature in the process, making the Universe approximately flat. This explains how Ω was much smaller than 1 at early times in the life of the Universe. Another result of this sudden expansion is that the horizon is greatly increased which means distant points on opposite ends of the CMB are still within the horizon, therefore, they remain in causal contact [112]. As the critical matter density is so close to 1, and has remained approximately 1, even today, despite deviating away from this during the post-inflationary period [108].

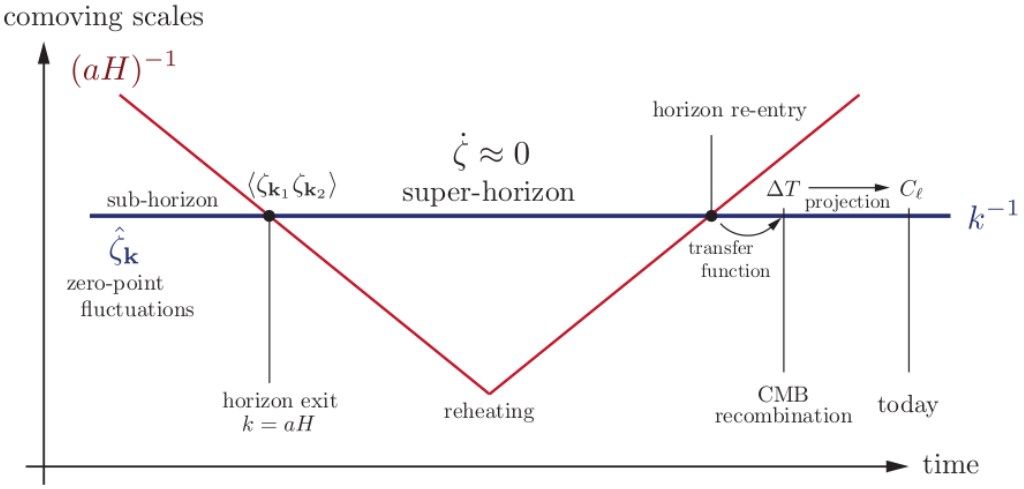

FIGURE 1.5: Curvature perturbation during and after inflation.The comoving horizon $(a\,H)^{-1}$ shrinks during inflation and grows in the resultant FRW evolution. This implies that the comoving scale k^{-1} exits the horizon at early times and re-enters the horizon at late times [111].

We define the Hubble parameter [118]:

$$H = \frac{\dot{a}}{a}, \tag{1.2.10}$$

where H is the derivative of the scale factor a over the scale factor $\dot{a}$.

The shrinking Hubble radius is related to the acceleration and pressure of the Universe via the Friedmann Equations which we arrive at from the FRW metric.

$$\boxed{H^2 \equiv \left(\frac{\dot{a}}{a}\right)^2 = \frac{1}{3}\rho - \frac{k}{a^2}}, \tag{1.2.11}$$

and

$$\boxed{\dot{H} + H^2 = \frac{\ddot{a}}{a} = -\frac{1}{6}(\rho + 3p)}. \tag{1.2.12}$$

where p is the pressure and ρ is the mass density.

The conditions we require for inflation are the following:

- Decreasing comoving horizon:-

A decreasing Hubble sphere which is defined as:

$$\frac{d}{dt}\left(\frac{H^{-1}}{a}\right) < 0. \tag{1.2.13}$$

This directly relates to the horizon and flatness problems.

- Accelerated expansion

From (1.2.11) we can produce the relation:

$$\frac{d}{dt}\left(\frac{H^{-1}}{a}\right) = \frac{-\ddot{a}}{(a\,H)^2}. \tag{1.2.14}$$

As a consequence of the shrinking Hubble radius we can see that this suggests accelerated expansion

$$\frac{d^2\,a}{dt^2} > 0. \tag{1.2.15}$$

This demonstrates why inflation is described as a period of rapid expansion.

- Negative pressure

If we look at the second Friedmann equation (remember $\ddot{a} > 0$ for this to be true) we need the following condition:

$$p < -\frac{1}{3}\rho. \tag{1.2.16}$$

So, along the shrinking Hubble radius, accelerated expansion is required. As a consequence we need a negative pressure [111, 119].

1.2.2 Scalar Fields

We introduce a scalar field, known as an inflaton. The Lagrangian for a scalar field ϕ has the usual form of a kinetic term minus a potential term:

$$\mathcal{L} = \frac{1}{2} g^{\mu\nu} \left(\partial_\mu \phi\right) \left(\partial_\nu \phi\right) - V\left(\phi\right). \tag{1.2.17}$$

$\mathcal{L}$ is the Lagrangian density of a generic scalar field $g^{\mu\nu}$ is the metric and $V(\phi)$ is the potential of the scalar field. The corresponding field equation from the Euler-Lagrange equation:

$$\Box^2 \phi + \frac{dV}{d\phi} = 0, \tag{1.2.18}$$

where $\Box^2$ is the covariant d'Alembertian operator [106]. A simple example is a free scalar field of mass m, for which the potential is $V(\phi) = \frac{1}{2} m^2 \phi^2$ and the field equation becomes the covariant Klein-Gordon equation,

$$\Box^2 \phi + m^2 \phi = 0. \tag{1.2.19}$$

For the moment we ignore the interactions ϕ may have with other fields in this theory. The stress-energy tensor $T^{\mu\nu}$ for ϕ is:

$$T^{\mu\nu} = \partial^\mu \phi \partial^\nu \phi - \mathcal{L}\, g^{\mu\nu}. \tag{1.2.20}$$

1.2.2.1 Single Field Inflation

Inflation becomes a natural idea as the negative pressure condition can be met with a single scalar field, ϕ, minimally coupled to gravity. The action for such a system is given by

$$S_\phi = -\int dx^4\sqrt{-g}\left[\frac{1}{2}\,g^{\mu\nu}\,\partial_\mu\,\phi\,\partial_\nu\,\phi + V(\phi)\right]. \tag{1.2.21}$$

The physical nature of the inflation field is still unknown which allows $V(\phi)$ to have different shapes. From our action we can derive the energy-momentum tensor $T^{\phi}_{\mu\nu}$ for ϕ,

$$T^{\phi}_{\mu\nu} = \partial_\mu\phi\,\partial_\nu\phi + g_{\mu\nu}\left[-\frac{1}{2}\,g^{\rho\sigma}\partial_\rho\phi\,\partial_\sigma + V(\phi)\right]. \tag{1.2.22}$$

ϕ must be homogeneous and can only be time dependent since FRW space-times are homogeneous and isotropic at background level. In this case the energy-momentum tensor is expressed as follows:

$$T_{\mu\nu} = \rho\,u_\mu\,u_\nu + \frac{p}{a^2}g_{\mu\nu}, \tag{1.2.23}$$

where $g_{\mu\nu}$ is the inverse metric, ρ and p are two constants which are only time dependent while u_μ is the four velocity for a comoving observer for whom space is homogeneous and isotropic.

ρ and p are defined as follows:

$$\rho = \frac{\dot{\phi}^2}{2} + V, \tag{1.2.24}$$

$$p = \frac{\dot{\phi}^2}{2} - V. \tag{1.2.25}$$

As a result of this we achieve our second condition for inflation where $\rho + 3p < 0$ when $\dot{\phi} \ll V$. This is what we need in order for inflation to take place. Inflation occurs if the scalar field slowly rolls down the potential. Consequently, the kinetic energy is dominated by the potential energy.

Dynamics of ϕ are found by plugging the solutions of ρ and p into the momentum conservation equation $\dot{\phi} + 3H(\rho + p) = 0$ resulting in the Klein-Gordon equation [104, 120].

$$\ddot{\phi} + 3H\dot{\phi} + V' = 0. \tag{1.2.26}$$

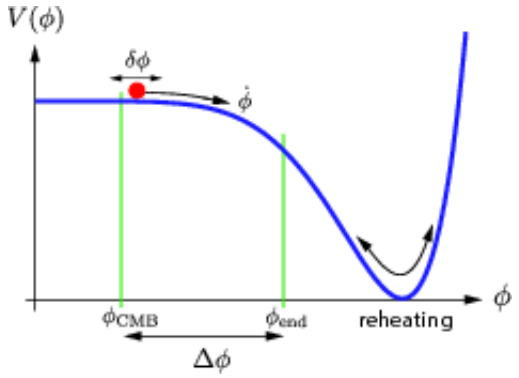

FIGURE 1.6: An example of a slow-roll potential. Acceleration occurs when the potential energy of the field, $V(\phi)$, dominates over the kinetic energy term $\frac{1}{2}\dot{\phi}^2$. Inflation ends at ϕ_{end} when the kinetic energy increases to be approximately equal to the potential term, $\frac{1}{2}\dot{\phi}^2 \approx V$. CMB fluctuations are created by quantum fluctuations $\delta\phi$ about 60 e-folds (e-fold is time interval in which a quantity grows exponentially increases by a factor of e) before the end of inflation. At the point of reheating, the energy density of the inflation is converted into radiation [121].

1.2.3 Non-attractor inflation and the Production of primordial gravitational waves

A key prediction of inflation is the production of background stochastic gravitational waves. The single field, slow-roll inflation scenario produces tensor fluctuations of the metric, also known as primordial gravitational waves, which are characterised by a near scale-invariant power-spectrum on super-horizon scales [122].

Non-attractor inflation can be used to enhance stochastic background primordial tensor fluctuations (or gravitational waves) at frequencies and scales that can be measured with gravitational wave experiments such as

LISA, LIGO and SKA. Moreover this type of inflation has the potential to amplify gravitational wave non Gaussianities [1]. This allows us to understand more of the early Universe and the what led to the creation of large scale structures.

In single field inflation the action is given as follows

$$S = \int d\eta\, d^3x\, \frac{z_S}{2}[\mathcal{R}'^2 - (\vec{\nabla}\mathcal{R})^2] \tag{1.2.27}$$

with:

$$z_S \equiv a\frac{\dot{\phi}}{H}, \tag{1.2.28}$$

where ϕ is the homogeneous scalar field, z_s is called the scalar pump field and $\mathcal{R}$ is the scalar fluctuations. In the case where the scalar pump field is in an increasing function of time - such as in slow roll regime, where the scalar field and Hubble parameter are approximately constant which results in inflation entering into an *attractor phase*, $\mathcal{R}$ is conserved at superhorizon scales and its spectrum is almost scale invariant. However, if the opposite occurs and z_s is in a rapidly decreasing function of time, albeit briefly, this means that the inflationary evolution is no longer an attractor. What we would expect is that the decaying mode of the curvature perturbation becomes dominant resulting in the power spectrum of the modes leaving the horizon during this *non-attractor phase*. It can be enhanced by several orders of magnitude in a short time interval [123].

In slow roll inflation, in the equation of motion for the scalar field, the second derivative of the scalar field, becomes unimportant and is ignored but in non-attractor inflation, the potential term becomes negligible, and the second derivative term becomes important.

To sum up, in this chapter we discussed a possible candidate for dark matter, axions, and how it is a more suitable than other particles, such as WIMPS. The detection methods for this pseudoscalar, both direct and

indirect, were discussed and how axions have the potential to produce gravitational waves (indirect detection of axions). In the next section we discussed inflation and how a particular model of inflation is able to amplify primordial gravitational waves from the early universe which then can be detected by various detectors (LIGO, LISA, SKA etc).

In the next chapter, we will discuss the indirect detection of axions using PTAs (detecting gravitational oscillations produced by axions) and how, using a multi-field set-up, the mass range of axions could be increased allowing them to be detected by more experiments.

In the third chapter we move on to discussing non-attractor inflation and how it can amplify primordial gravitational waves from the early universe allowing us to observe them with detectors.

Finally, in the fourth chapter, building on chapter 3, we discuss the detection of 3pt tensor, scalar and a combination of both functions by PTA and LIGO.

Chapter 2

Multi-field Scalar field condensates as Dark Matter

One of the biggest mysteries in modern cosmology concerns the unknown nature of Dark Matter. Many candidates have been suggested to solve this problem including an ultra-light scalar field with a mass range between $10^{-22}eV$ and $10^{-33}eV$. Ultra-light scalar fields/ultra-light axions are able to address the issues that arise with heavier dark matter candidates, such as the cuspy halo problem. Axions induce oscillations which may be able to be detected by pulsar timing arrays.

Returning to what was discussed in subsection 1.1.2 from the previous chapter we know that pulsar timing arrays study the periods of pulsars/the arrival time of their pulses. Pulsar periods are very precise; to the point that they can rival atomic clocks. However the results from the arrays indicate that the arrival times of the pulses do not match up with previously recorded periods (take longer to arrive at the detectors). This suggests that something is causing this effect and an option for this may be an ultra-light axion. Massive astrophysical events, such as the merging or two supermassive black holes, generate background gravitational waves which spread throughout all spacetime. As previously stated, the axions are able

to induce oscillations in its pressure which could contribute to the increase in pulse arrival time.

Andrei Khmelnitsky and Valery Rubakov first discussed this method of dark matter detection in [95] using a single field approach. In this chapter we are discussing a multi field case, we begin with two, uncoupled, scalar fields before moving on to the coupled case. In each scenario we aim to explore if our system could possibly be considered as dark matter and whether or not it could be detected by present/future pulsar timing arrays.

2.1 Multi field system uncoupled

We begin with two scalar fields, ϕ and χ which are composed of a background field and the perturbations around it:

$$\phi = \phi_c(\eta) + \varphi(\eta, \mathbf{x}), \tag{2.1.1}$$

$$\chi = \chi_c(\eta) + \Theta(\eta, \mathbf{x}), \tag{2.1.2}$$

where ϕ_c and χ_c are the background fields and φ and Θ denote the perturbations around the background fields.

The background fields are expressed as follows

$$\phi_c = u_\phi(\eta)\cos[m_\phi t(\eta)] + w_\phi(\eta)\sin[m_\phi t(\eta)], \tag{2.1.3}$$

$$\chi_c = u_\chi(\eta)\cos[m_\chi t(\eta)] + w_\chi(\eta)\sin[m_\chi t(\eta)], \tag{2.1.4}$$

where u_ϕ, u_χ, w_ϕ and w_χ are slowly varying functions of conformal time. u_ϕ and u_χ are leading order and w_ϕ and w_χ are subleading order. The leading order functions are defined as

$$u_\phi(\eta) = \frac{C_\phi}{a^{\frac{3}{2}}}, \tag{2.1.5}$$

$$u_{\chi}(\eta) = \frac{C_{\chi}}{a^{\frac{3}{2}}}, \tag{2.1.6}$$

where C_{ϕ} and C_{χ} are constants.

The perturbations around the background field are denoted by

$$\varphi = B_{\phi}(\eta, \mathbf{x}) \sin\left[m_{\phi} t(\eta)\right] + A_{\phi}(\eta, \mathbf{x}) \cos\left[m_{\phi} t(\eta)\right], \tag{2.1.7}$$

$$\Theta = B_{\chi}(\eta, \mathbf{x}) \sin\left[m_{\chi} t(\eta)\right] + A_{\chi}(\eta, \mathbf{x}) \cos\left[m_{\chi} t(\eta)\right], \tag{2.1.8}$$

where A_{ϕ}, A_{χ}, B_{ϕ} and B_{χ} are slowly varying functions of conformal time.

In this system the energy densities of the two scalars (ρ_{ϕ} ρ_{χ}) are taken to be of approximately the same order:

$$\rho_{\phi} \simeq \rho_{\chi}.$$

The following conditions are set to facilitate this: one of the masses, m_{ϕ}, is given a much larger value than the other, m_{χ}, which itself is much larger value than the Hubble parameter, H.

$$m_{\phi} \gg m_{\chi} \gg H. \tag{2.1.9}$$

Consequently, the scalar field, with the smaller mass, χ is larger than the scalar with the larger mass, ϕ

$$\chi \gg \phi, \tag{2.1.10}$$

The above condition also applies to the constants of the two scalar fields

$$C_{\chi} \gg C_{\phi}. \tag{2.1.11}$$

This allows the mass of the scalar multiplied by its constant to be approximately the same order as the other

$$m_{\phi} C_{\phi} \simeq m_{\chi} C_{\chi}. \tag{2.1.12}$$

Which, in turn, leads to the condition needed for ρ_ϕ and ρ_χ to be of the same order

$$C_\chi = \left(\frac{m_\phi}{m_\chi}\right) C_\phi. \tag{2.1.13}$$

The metric, which both scalar fields interact with, can be decomposed into a slowly varying part $\bar{\Phi}$ and an oscillating part Φ_{osc}. $\bar{\Phi}$ is of order $O(m^0)$ as it receives contributions from all cosmic medium and Φ_{osc} is of order $O(m^{-1})$ [124].

$$\Phi = \bar{\Phi} + \Phi_{osc}. \tag{2.1.14}$$

Our present task is to demonstrate whether Φ follows one field or the other or perhaps it depends on both. In order to answer this question the field equations for the system need to be solved. Before we can do this, we need the solutions for the energy momentum tensor.

Energy Density perturbations:

$$\delta\rho_{\varphi\Theta} = -\frac{1}{a^2}\left(\phi_c'\right)^2\Phi + \frac{1}{a^2}\phi_c'\varphi' + m_\phi^2\,\phi_c\,\varphi - \frac{1}{a^2}\left(\chi_c'\right)^2\Phi + \frac{1}{a^2}\chi_c'\Theta' + m_\phi^2\,\phi_c\,\Theta, \tag{2.1.15}$$

Velocity:

$$\left[-\left(\rho + p\right)v\right]_{\varphi\Theta} = \frac{1}{a^2}\phi_c'\varphi' + m_\phi^2\,\chi_c\,\Theta, \tag{2.1.16}$$

Pressure perturbations:

$$\delta p_{\varphi\Theta} = -\frac{1}{a^2}\left(\phi_c'\right)^2\Phi + \frac{1}{a^2}\phi_c'\varphi' - m_\phi^2\,\phi_c\,\varphi - \frac{1}{a^2}\left(\chi_c'\right)^2\Phi + \frac{1}{a^2}\chi_c'\Theta' - m_\phi^2\,\phi_c\,\Theta. \tag{2.1.17}$$

The order of each component is now given before writing out the field equations for the system

$$u_\phi(\eta) = O\left(m^{-1}\right)$$
$$u_\chi(\eta) = O\left(m^{-1}\right)$$
$$w_\phi(\eta) = O\left(m^{-2}\right)$$
$$w_\chi(\eta) = O\left(m^{-2}\right)$$

$$B_\phi(\eta,\mathbf{x}) = O\left(m^{-1}\right)$$
$$B_\chi(\eta,\mathbf{x}) = O\left(m^{-1}\right)$$
$$A_\phi(\eta,\mathbf{x}) = O\left(m^{-2}\right)$$
$$A_\chi(\eta,\mathbf{x}) = O\left(m^{-2}\right)$$
$$\Phi = O\left(m^{0}\right)$$
$$\bar{\Phi} = O\left(m^{0}\right)$$
$$\Phi_{osc} = O\left(m^{-1}\right)$$
$$\bar{\Phi}' = O\left(m^{0}\right)$$
$$\Phi'_{osc} = O\left(m^{0}\right)$$
$$\Psi = O\left(m^{0}\right)$$
$$\bar{\Psi} = O\left(m^{0}\right)$$
$$\Psi_{osc} = O\left(m^{-1}\right)$$
$$\bar{\Psi}' = O\left(m^{0}\right)$$
$$\Psi'_{osc} = O\left(m^{0}\right)$$
$$\rho_\phi = O\left(m^{0}\right)$$
$$\rho_\chi = O\left(m^{0}\right)$$
$$m_\phi = O\left(m^{1}\right)$$
$$m_\chi = O\left(m^{1}\right)$$
$$C_\phi = O\left(m^{-1}\right)$$
$$C_\chi = O\left(m^{-1}\right)$$

The field equations for the system are written to order $O(m^0)$ ϕ:

$$\varphi'' + 2\,\frac{a'}{a}\,\Psi' + k^2\,\Psi + m_\phi^2\,a^2\,\Psi - 4\,\phi_c'\,\Phi' + 2\,a^2\,m_\phi^2\,\phi_c\,\Phi = 0, \tag{2.1.18}$$

where a is the scale factor and Ψ and Φ are the gravitational potentials.

Setting the equation to order $O(m^1)$ gives the following : $B'_\phi + \frac{3\,a'}{2\,a}\,B_\phi + m_\phi\,a\,u_\phi\,\Phi = 0$. χ:

$$\Theta'' + 2\,\frac{a'}{a}\,\Psi' + k^2\,\Psi + m_\phi^2\,\Psi - 4\,\phi_c'\,\Phi' + 2\,a^2\,m_\phi^2\,\phi_c\,\Phi = 0. \tag{2.1.19}$$

Setting equation to order $O(m^1)$: $B'_\chi + \frac{3\,a'}{2\,a}\,B_\chi + m_\chi\,a\,u_\chi\,\Phi = 0$.

Now that the expressions for the field equations have been given, we set the $O(m^1)$ equations to zero and solve B'_ϕ and B'_χ. Once the solutions for these slowly varying functions have been found they are substituted into the energy momentum (EM) tensor. Finally, we average the components of the EM tensor over a period (larger period: $\frac{2\pi}{m_\chi}$ (smaller mass $\rightarrow$ larger period)).

The solutions for B'_ϕ and B'_χ are put back in to (2.1.15) giving the following expression for the pressure perturbation component of the EM tensor.

$$\begin{aligned}\overline{\delta\,p_{\varphi\Theta}} = &-\frac{C_\phi\,m_\phi\,m_\chi\,B_\phi(\eta)}{4\pi\,a(\eta)^{\frac{3}{2}}} + \frac{C_\phi\,m_\phi\,m_\chi\,B_\phi(\eta)\,\cos\left[4\,\frac{m_\phi}{m_\chi}\,\pi\right]}{4\pi\,a(\eta)^{\frac{3}{2}}} \\ &- \frac{C_\phi\,m_\phi\,m_\chi\,A_\phi(\eta)\,\sin\left[4\frac{m_\phi}{m_\chi}\pi\right]}{4\pi\,a(\eta)^{\frac{3}{2}}} - \frac{3\,C_\phi\,m_\chi\,B_\phi(\eta)\,H(\eta)\,\sin\left[4\frac{m_\phi}{m_\chi}\,\pi\right]}{8\,\pi\,a(\eta)^{\frac{3}{2}}} \\ &+ \frac{m_\phi\,m_\chi\,B_\phi(\eta)\,\sin\left[4\frac{m_\phi}{m_\chi}\pi\right]}{4\pi}.\end{aligned} \tag{2.1.20}$$

Since we have set $m_\phi \gg m_\chi$, the Cosine function becomes 1 and the two $O(m^1)$ terms cancel if m_ϕ is an integer multiple of m_χ. The Sine function also vanishes in the $O(m^0)$ terms which leaves us with a pressureless system.

We support this statement by using different periods. When averaged over the small period $\frac{2\,\pi}{m_\phi}$ we are also able to obtain a pressureless system (if the condition, $m_\phi \gg m_\chi$, is a followed and as a result, m_ϕ is an integer multiple of m_χ). Since the system appears to be pressureless it can be considered to be a dark matter candidate (at least in this regime). This gives us the

following expression for the pressure pertubations

$$\overline{\delta\, p_{\varphi\Theta_{small}}} = -\frac{C_\phi\, m_\phi^2\, B_\chi(\eta)}{4\pi\, a(\eta)^{\frac{3}{2}}} + \frac{C_\phi\, m_\phi^2\, B_\chi(\eta)\, \cos\left[4\frac{m_\chi}{m_\phi}\pi\right]}{4\pi\, a(\eta)^{\frac{3}{2}}} - \frac{C_\phi\, m_\phi^2\, A_\chi^2(\eta)\, \sin\left[4\frac{m_\chi}{m_\phi}\pi\right]}{4\pi\, a(\eta)^{\frac{3}{2}}} - \frac{3\, C_\phi\, m_\phi^2\, B_\chi(\eta)\, H(\eta)\, \sin\left[4\,\frac{m_\chi}{m_\phi}\,\pi\right]}{8\, m_\chi\, \pi\, a(\eta)^{\frac{3}{2}}} + \frac{m_\chi\, m_\phi\, B_\chi(\eta)\, w_\chi(\eta)\, \sin\left[4\frac{m_\chi}{m_\phi}\pi\right]}{4\,\pi}. \quad (2.1.21)$$

The process is repeated for the density and velocity components.

Velocity component when averaged over the longer period:

$$\overline{[(\rho+p)\, v]}_{\varphi\Theta} = -\frac{C_\phi\, m_\phi\, B_\phi(\eta)}{2\, a(\eta)^{\frac{5}{2}}} - \frac{C_\phi\, m_\phi\, B_\chi(\eta)}{2\, a(\eta)^{\frac{5}{2}}} + \frac{C_\phi\, m_\chi\, B_\chi(\eta)\, \sin\left[4\frac{m_\phi}{m_\chi}\pi\right]}{8\,\pi\, a(\eta)^{\frac{5}{2}}}, \quad (2.1.22)$$

Velocity component when averaged over the shorter period:

$$\overline{[(\rho+p)\, v]}_{\varphi\Theta_{small}} = -\frac{C_\phi\, m_\phi\, B_\phi(\eta)}{2\, a(\eta)^{\frac{5}{2}}} - \frac{C_\phi\, m_\phi\, B_\chi(\eta)}{2\, a(\eta)^{\frac{5}{2}}} + \frac{C_\phi\, m_\phi^2\, B_\chi(\eta)\, \sin\left[4\frac{m_\chi}{m_\phi}\pi\right]}{8\, m_\chi\, \pi\, a(\eta)^{\frac{5}{2}}}. \quad (2.1.23)$$

Energy density perturbations averaged over the longer period:

$$\overline{\delta\, \rho_{\varphi\Theta}} = \frac{C_\phi\, m_\phi^2\, A_\phi(\eta)}{a(\eta)^{\frac{3}{2}}} + \frac{C_\phi\, m_\phi\, m_\chi\, A_\chi(\eta)}{a(\eta)^{\frac{3}{2}}} + m_\chi^2\, B_\chi(\eta)\, w_\chi(\eta) - \frac{3\, C_\phi\, m_\chi\, B_\phi(\eta)\, H(\eta)\, \sin\left[4\,\frac{m_\phi}{m_\chi}\pi\right]}{8\,\pi\, a(\eta)^{\frac{3}{2}}} + m_\phi^2\, B_\phi(\eta)\, w_\phi(\eta), \quad (2.1.24)$$

Energy density perturbations averaged over the shorter period:

$$\overline{\delta\, \rho_{\varphi\Theta_{small}}} = \frac{C_\phi\, m_\phi^2\, A_\phi(\eta)}{a(\eta)^{\frac{3}{2}}} + \frac{C_\phi\, m_\phi\, m_\chi\, A_\chi(\eta)}{a(\eta)^{\frac{3}{2}}} + m_\chi^2\, B_\chi(\eta)\, w_\chi(\eta) - \frac{3\, C_\phi\, m_\phi^2\, B_\chi(\eta)\, H(\eta)\, \sin\left[4\,\frac{m_\chi}{m_\phi}\pi\right]}{8\,\pi\, a(\eta)^{\frac{3}{2}}} + m_\phi^2\, B_\phi(\eta)\, w_\phi(\eta). \quad (2.1.25)$$

Now that we have a pressureless system/ potential dark matter candidate for the case where m_ϕ is much larger than m_χ we want to check whether the system is still pressurelss when this is not the case. This can be done by averaging over an even longer period.

2.1.1 Averaging over an even longer period

For the case where m_ϕ is not an integer multiple of m_χ we choose a longer period which corresponds to the shortest distance required before the plots of both scalar fields intersect. This period is called M and m_ϕ and m_χ are integer multiples of it. This gives the following condition

$$M \ll m_\chi \ll m_\phi.$$

With this condition we can check if the EM components have a similar form to the previous conditions. Below we have the EM tensor components when averaged over the longest period M.

Energy density perturbations:

$$\begin{aligned}\overline{\delta\,\rho_{\varphi\Theta_{longest}}} &= \frac{C_\phi\, m_\phi^2\, A_\phi(\eta)}{a(\eta)^{\frac{3}{2}}} + \frac{C_\phi\, m_\phi\, m_\chi\, A_\chi(\eta)}{a(\eta)^{\frac{3}{2}}} + m_\chi^2 B_\chi(\eta)\, w_\chi(\eta) \\ &- \frac{3\, C_\phi\, M\, B(\eta)\, H(\eta)\, \sin[4\frac{m_\phi}{M}\pi]}{8\,\pi\, a(\eta)^{\frac{3}{2}}} - \frac{3\, C_\phi\, M\, m_\phi\, B_\phi(\eta)\, H(\eta)\, \sin[4\frac{m_\chi}{M}\pi]}{8\, m_\chi\, \pi\, a(\eta)^{\frac{3}{2}}} \\ &+ m_\phi^2\, B_\phi(\eta)\, w_\phi(\eta). \end{aligned} \tag{2.1.26}$$

Velocity:

$$\begin{aligned}\overline{[-(\rho+p)\,v]_{\varphi\Theta_{longest}}} &= -\frac{C_\phi\, m_\phi\, B_\phi(\eta)}{2\, a(\eta)^{\frac{5}{2}}} - \frac{C_\phi\, m_\phi\, B_\chi(\eta)}{2\, a(\eta)^{\frac{5}{2}}} \\ &+ \frac{C_\phi\, M\, B_\chi(\eta)\, \sin[4\frac{m_\phi}{M}\pi]}{8\,\pi\, a(\eta)^{\frac{5}{2}}} + \frac{C_\phi\, M\, m_\phi\, B_\chi(\eta)\, \sin[4\frac{m_\chi}{M}\pi]}{8\, m_\chi\, \pi\, a(\eta)^{\frac{5}{2}}}. \end{aligned} \tag{2.1.27}$$

Pressure perturbations:

$$\overline{\delta p_{\varphi\Theta_{longest}}} = -\frac{C_\phi M m_\phi B_\phi(\eta)\,\sin^2[2\frac{m_\phi}{M}\pi]}{2\pi a(\eta)^{\frac{3}{2}}} - \frac{C_\phi M m_\phi A_\phi(\eta)\sin[4\frac{m_\phi}{M}\pi]}{4\pi a(\eta)^{\frac{3}{2}}}$$
$$- \frac{3C_\phi M B_\phi(\eta) H(\eta)\sin[4\frac{m_\phi}{M}\pi]}{8\pi a(\eta)^{\frac{3}{2}}} - \frac{C_\phi M m_\phi B_\chi(\eta)\,\sin^2[2\frac{m_\chi}{M}\pi]}{2\pi a(\eta)^{\frac{3}{2}}}$$
$$- \frac{C_\phi M m_\phi C_\chi(\eta)\,\sin[4\frac{m_\chi}{M}\pi]}{4\pi a(\eta)^{\frac{3}{2}}} - \frac{3C_\phi M m_\phi B_\chi(\eta) H(\eta)\,\sin[4\frac{m_\chi}{M}\pi]}{8 m_\chi \pi a(\eta)^{\frac{3}{2}}}$$
$$+ \frac{M m_\chi B_\chi(\eta) w_\chi(\eta)\,\sin[4\,\frac{m_\chi}{M}\pi]}{4\pi} + \frac{M m_\phi B_\phi(\eta)\,\sin[4\frac{m_\phi}{M}\pi] w_\phi(\eta)}{4\pi}. \tag{2.1.28}$$

The solutions for the EM tensor, when averaged over an even longer period, correspond to the previous case. As a result at leading order the system is pressureless due to m_ϕ and m_χ being integer multiples of M. The system can still be considered a dark matter candidate at this point.

Another test will done to check whether the system can still be considered a valid dark matter candidate/ pressureless system. In this next case, we will obtain the components of the EM tensor for larger distances.

2.1.2 $k^2 = O(m_\chi) \ll m_\phi$ (large distances)

The same system is considered as in the previous section, however the conformal momentum is assigned to be of order $O(m_\chi)$. This means we are considering this system over larger distances. All terms are of the same order as previously discussed except for one notable exception. The functions B_ϕ, B_χ, A_ϕ and A_χ are now all of the same order ($O(m^0)$).

The EM tensor components are stated to leading order

Energy density perturbations:

$$\overline{\delta\,\rho_{\varphi\Theta}} = m_\phi^2\,A_\phi\,(\eta)\;u_\phi\,(\eta) + m_\chi^2\,(\eta)\;A_\chi\,(\eta)\;u_\chi\,(\eta) + m_\phi^2\,B_\phi\,(\eta)\;w_\phi\,(\eta) \\ -\frac{1}{2}m_\phi^2\,u_\phi^2\,(\eta)\;\Phi\,(\eta) - \frac{m_\phi\,u_\phi\,(\eta)\;B_\phi'\,(\eta)}{2\,a\,(\eta)} - \frac{m_\phi\,B_\phi\,(\eta)\;u_\phi'\,(\eta)}{2\,a\,(\eta)}. \tag{2.1.29}$$

Velocity:

$$\left[(\rho+p)v\right]_{\varphi\chi} = -\frac{C_\phi\,m_\phi\,\pi\,B_\phi(\eta)}{m_\chi\,a^{\frac{5}{2}}(\eta)} - \frac{C_\phi\,m_\phi\,\pi\,B_\chi(\eta)}{m_\chi\,a^{\frac{5}{2}}(\eta)} \\ + \frac{C_\phi\,B_\phi(\eta)\,\sin\left[4\frac{m_\phi}{m_\chi}\pi\right]}{4\,a^{\frac{3}{2}}(\eta)}. \tag{2.1.30}$$

Solution for pressure perturbations:

$$\overline{\delta\,p_{\varphi\Theta}} = -\frac{1}{2}\,m_\phi^2\,u_\phi\,(\eta)^2\;\Phi\,(\eta) - \frac{1}{2}\,m_\chi^2\,u_\chi\,(\eta)^2\;\Phi\,(\eta) - \frac{m_\phi\,u_\phi\,(\eta)\;B_\phi'\,(\eta)}{2\,a\,(\eta)} \\ -\frac{m_\chi\,u_\chi\,(\eta)\;B_\chi'\,(\eta)}{2\,a\,(\eta)} + \frac{m_\phi\,u_\phi'\,(\eta)\;B_\phi\,(\eta)}{2\,a\,(\eta)} + \frac{m_\chi\,u_\chi'\,(\eta)\;B_\chi\,(\eta)}{2\,a\,(\eta)}. \tag{2.1.31}$$

As we have set the following condition, $k \simeq m_\chi$ and because the slowly varying functions are now all of the same order $O(m^0)$ the two field equations produce three equations when written at order $O(m^1)$. This is because A_χ and A_ϕ are no longer suppressed as they are now the same order as the other functions.

$$B_\phi'\,(\eta) + \frac{3\,a\,(\eta)'}{2\,a\,(\eta)}B_\phi + m_\phi\,a\,(\eta)\;u_\phi\,(\eta) + \frac{k^2}{2\,m_\phi\,a\,(\eta)} = 0, \tag{2.1.32}$$

$$B_\chi'\,(\eta) + \frac{3\,a\,(\eta)'}{2\,a\,(\eta)}B_\chi + m_\chi\,a\,(\eta)\;u_\chi\,(\eta) + \frac{k^2}{2\,m_\chi\,a\,(\eta)} = 0, \tag{2.1.33}$$

$$A_\chi'\,(\eta) + \frac{3\,a\,(\eta)'}{2\,a\,(\eta)}A_\chi - \frac{k^2}{2\,m_\chi\,a\,(\eta)}\,B_\chi = 0. \tag{2.1.34}$$

We make use of (2.1.32) and (2.1.33) and put them back into the pressure perturbations solutions giving us a simplified solution.

$$\delta\, p_{\varphi\Theta} = \frac{u_\chi\,(\eta)\; k^2\, A_\chi\,(\eta)}{4\, a\;(\eta)^2}. \tag{2.1.35}$$

In this set up ($k \simeq m_\chi$) the pressure perturbations expression is now of order $O(m^0)$ which suggests that the pressure is no longer negligible as it had been in the previous scenarios.

The sound speed squared for a system of two scalar fields at large distances ($k \simeq m_\chi \ll m_\phi$) is the pressure perturbations divided by the energy density perturbations.

$$u_s^2 \equiv \frac{\delta\, p_{\varphi\Theta}}{\delta\, \rho_{\varphi\Theta}}. \tag{2.1.36}$$

The expressions (2.1.32) and (2.1.33) are rearranged to define $B'_\phi(\eta)$ and $B'_\chi(\eta)$ respectively. The conditions for the leading order slowly varying functions $u_\phi(\eta)$ (2.1.5) and $u_\chi(\eta)$ (2.1.6) are put back into (2.1.36)

$$u_s^2 = \frac{C_\chi\, k^2\, A_\chi(\eta)}{4\, a(\eta)^2 \left(C_\chi\, m_\chi^2\, A_\chi(\eta) + m_\phi^2 \left(C_\phi\, A_\phi(\eta) + a(\eta)^{\frac{3}{2}}\, B_\phi(\eta)\, w_\phi(\eta)\right)\right)}. \tag{2.1.37}$$

Since the system is pressureless at leading order (pressure is negligible compared with energy density) it can at least be considered as a potential dark matter candidate at $O(m^0)$. For each case the system realised the criteria needed to be regarded as a potential candidate. Now that we have shown this we can move to our discussion of detecting scalar field dark matter via pulsar timing arrays.

2.2 Pulsar timing: Two scalar fields

Following the work of [95] we aim to show that in the coming years it will be possible for the pulsar timing arrays to detect a system of multiple

ultra-light scalar fields.

Our system as previously stated involves two uncoupled ultra-light scalar fields

$$\phi(\mathbf{x},t) = A_\phi(\mathbf{x})\cos\left(m_\phi t + \alpha_\phi(\mathbf{x})\right), \tag{2.2.1}$$

$$\chi(\mathbf{x},t) = A_\chi(\mathbf{x})\cos\left(m_\chi t + \alpha_\chi(\mathbf{x})\right), \tag{2.2.2}$$

where A_ϕ and A_χ are the amplitudes of the scalar fields and α_ϕ and α_χ are their phases.

We give the expression for the energy-momentum tensor in order to obtain the expressions for the energy density and pressure.

$$T_{\mu\nu} = \partial_\mu\phi\partial_\nu\phi + \partial_\mu\chi\partial_\nu\chi - \frac{1}{2}g_{\mu\nu}\left((\partial\phi)^2 - m_\phi^2\phi^2 + (\partial\chi)^2 - m_\chi^2\chi^2\right). \tag{2.2.3}$$

When the expressions for scalar fields (2.2.1) and (2.2.2) are put into the energy-momentum tensor we can see that the energy density T_{00} has a dominant time-independent component.

$$\rho_{DM} \equiv T_{00} = \frac{1}{2}m_\phi^2 A_\phi^2 + \frac{1}{2}m_\chi^2 A_\chi^2. \tag{2.2.4}$$

The EM tensor also has an oscillating part which is proportional to $(\nabla\phi)^2 + (\nabla\chi)^2 \sim \frac{k^2}{m_\phi^2} + \frac{k^2}{m_\chi^2}$

$$\rho_{DM}^{osc} \sim \frac{k^2}{m_\phi^2}\rho_{DM}^{\phi} + \frac{k^2}{m_\chi^2}\rho_{DM}^{\chi} = v_\phi^2\,\rho_{DM}^{\phi} + v_\chi^2\,\rho_{DM}^{\chi}. \tag{2.2.5}$$

However, the dominant term of T^{ij} (spatial components) oscillates in time with frequency

$$\omega_\phi = 2m_\phi, \tag{2.2.6}$$

$$\omega_\chi = 2m_\chi, \tag{2.2.7}$$

and the amplitude of the scalar fields are of order of the energy density, ρ_{DM}:

$$T_{ij} = -\left(\frac{1}{2}m_\phi^2 A_\phi^2 \cos\left(\omega_\phi t + 2\alpha_\phi\right) + \frac{1}{2}m_\chi^2 A_\chi^2 \cos\left(\omega_\chi t + 2\alpha_\chi\right)\right)\delta_{ij} \equiv p\left(\mathbf{x}, t\right)\delta_{ij}. \tag{2.2.8}$$

When we average the pressure of the period, it is zero, to leading order the system is pressureless.

However oscillating pressure is not negligible as it induces oscillations in the gravitational potentials which can lead to observable effects.

In order to find a solution for the gravitational field produced by scalar field dark matter in the galactic halo we use the Newtonian gauge. The metric now takes the following form:

$$ds^2 = \left(1 + 2\Phi\left(\mathbf{x}, t\right)\right)dt^2 - \left(1 - 2\Psi\left(\mathbf{x}, t\right)\right)\delta_{ij}dx^i dx^j. \tag{2.2.9}$$

Ψ and Φ contain the dominant time-independent parts and the parts that oscillate with frequencies which are multiples of ω_ϕ and ω_χ. With only the leading order oscillating terms taken into consideration the gravitational potentials take the following form:

$$\begin{aligned}\Psi\left(\mathbf{x}, t\right) \simeq \Psi_0\left(\mathbf{x}\right) + \Psi_c^\phi\left(\mathbf{x}\right)\cos\left(\omega_\phi t + 2\alpha_\phi\left(\mathbf{x}\right)\right) + \Psi_c^\chi\left(\mathbf{x}\right)\cos\left(\omega_\chi t + 2\alpha_\chi\left(\mathbf{x}\right)\right) \\ + \Psi_s^\phi\left(\mathbf{x}\right)\cos\left(\omega_\phi t + 2\alpha_\phi\left(\mathbf{x}\right)\right) + \Psi_s^\chi\left(\mathbf{x}\right)\cos\left(\omega_\chi t + 2\alpha_\chi\left(\mathbf{x}\right)\right).\end{aligned} \tag{2.2.10}$$

Using the same method we are able to find Φ which takes a similar form.

$$\begin{aligned}\Phi\left(\mathbf{x}, t\right) \simeq \Phi_0\left(\mathbf{x}\right) + \Phi_c^\phi\left(\mathbf{x}\right)\cos\left(\omega_\phi t + 2\alpha_\phi\left(\mathbf{x}\right)\right) + \Phi_c^\chi\left(\mathbf{x}\right)\cos\left(\omega_\chi t + 2\alpha_\chi\left(\mathbf{x}\right)\right) \\ + \Phi_s^\phi\left(\mathbf{x}\right)\cos\left(\omega_\phi t + 2\alpha_\phi\left(\mathbf{x}\right)\right) + \Phi_s^\chi\left(\mathbf{x}\right)\cos\left(\omega_\chi t + 2\alpha_\chi\left(\mathbf{x}\right)\right).\end{aligned} \tag{2.2.11}$$

The expressions for Ψ and Φ were found with the use of the linearised Einstein equations. The time independent component of Einstein equations, T_{00} is written as

$$\Delta\Psi = 4\pi G T_{00} = 4\pi G \rho_{DM}. \tag{2.2.12}$$

We are now able to find the solution for $\Psi_0(\mathbf{x})$ (time independent part). Since density on RHS has no time dependence to leading order we are able to suppress Ψ_s and Ψ_c w.r.t. Ψ_0.

From the trace part of spatial components of Einstein equations the oscillating parts can be found

$$-6\ddot{\Psi} + 2\nabla(\Psi - \Phi) = 8\pi G T_{kk} = 24\pi G p(\mathbf{x}, t). \tag{2.2.13}$$

Now we can plug in $\Psi(\mathbf{x}, t)$ in order to separate five terms with different time dependence.

Note that the relationship between the gravitational potentials is as follows: $\Psi = -\Phi$, $\Psi_0(\mathbf{x}) = \Phi_0(\mathbf{x})$.

As one is equal to the negative of the other the time independent parts $\Psi_0(\mathbf{x})$ and $\Phi_0(\mathbf{x})$ are equal to one another

If the frequencies ω_ϕ and ω_χ are significantly different $\sin(\omega_\phi t + 2\alpha_\phi) + \sin(\omega_\chi t + 2\alpha_\chi)$ give $\Psi_s = 0$ to leading order.

This is what remains of the gravitational potential Ψ:

$$\Psi(\mathbf{x}, t) = \Psi_c^\phi(x)\cos(\omega_\phi t + 2\alpha_\phi(\mathbf{x})) + \Psi_c^\chi(x)\cos(\omega_\chi t + 2\alpha_\chi(\mathbf{x})). \tag{2.2.14}$$

Looking at the functions $\cos(\omega_\phi t + 2\alpha_\phi(\mathbf{x})) + \cos(\omega_\chi t + 2\alpha_\chi(\mathbf{x}))$ we arrive at the following results for the amplitudes Ψ_c^ϕ and Ψ_c^χ

$$\begin{aligned}\Psi_c^\phi &= \frac{1}{2}\pi G A_\phi(\mathbf{x})^2 = \pi\frac{G\rho_{DM}^\phi(\mathbf{x})}{m_\phi^2},\\ \Psi_c^\chi &= \frac{1}{2}\pi G A_\chi(\mathbf{x})^2 = \pi\frac{G\rho_{DM}^\chi(\mathbf{x})}{m_\chi^2}.\end{aligned} \tag{2.2.15}$$

Now that we have the values for the amplitude of the gravitational potential we are able to move on and investigate how a scalar field system is able, possibly, to effect pulsar timing.

2.2.1 How a multi-field scalar system could have an effect on pulsar timing

Pulsars are highly magnetised, rotating neutron stars that emit beams of EM radiation. They are very dense with short periods of rotation. However, there is a delay in arrival time of the pulses when observed. This could be due to the presence of the ultra-light scalar fields slowly oscillating with the pulse passing through these oscillations causing them to be perturbed.

The expression for the gravitational potential (2.2.14) includes time dependent terms which induce oscillations, that, in turn cause a time-dependent frequency shift resulting in a time delay for any propagating signal. Some factors must be taken into account before we can attribute the variation of the signal arrival time to the propagation derived from time-dependent metric. These factors include the motion of the laboratory frame w.r.t. the Solar System barycentre, the motion of the pulsars in the galactic rest frame (or peculiar motion), how the interstellar medium is dispersed and the intrinsic variation of the pulsar period [125].

We begin by estimating the time-dependent part of the timing residuals for our case where a multi-field system of ultra-light scalar fields is the major component of the dark matter halo of the galaxy. The change in arrival time of a pulse at time t as an integral of the relative change in the arrival frequency of the pulse is given the following form:

$$\Delta t\left(t\right) = -\int_0^t \frac{\Omega\left(t'\right) - \Omega_0}{\Omega_0} dt', \tag{2.2.16}$$

where $\Omega(t)$ is pulse arrival frequency at the detector at a time t, and Ω_0 is frequency when there is no time variation of the metric, which corresponds to the emission frequency of the pulse at the pulsar. As can be seen, the frequency shift is proportional to gravitational potentials Ψ and Φ. For signal emitted with frequency Ω_0 at point $\mathbf{x}_p$ at the moment t' and detected

at point $\mathbf{x}$ at moment t the frequency shift is given by

$$\frac{\Omega(t') - \Omega_0}{\Omega_0} = \Psi(\mathbf{x}, t) - \Psi(\mathbf{x}_p, t') - \int_{t'}^{t} n_i \partial_i \left(\Psi(\mathbf{x}'', t'') + \Phi(\mathbf{x}'', t'')\right). \quad (2.2.17)$$

Most of the pulsars used in pulsar timing measurements are found at distances $D \gtrsim 100\,pc \gg m^{-1}$. This results in the integrand being unimportant in this instance since it is a fast oscillating function over the integration interval. Only the gravitational point at the detector, $\Psi(\mathbf{x}, t)$, contributes to the time delay so the oscillating part of $\Phi(\mathbf{x}, t)$ does not need to be calculated. Since Ψ_0 only induces a time-independent frequency shift which is not detected/measured by the pulsar timing arrays, the frequency shift takes the form

$$\begin{aligned}\frac{\Omega(t') - \Omega_0}{\Omega_0} = {} & \Psi_c^{\phi}\left((\mathbf{x})\cos\left(\omega_\phi t + 2\alpha_\phi(\mathbf{x})\right) - \cos\left(\omega_\phi(t - D) + 2\alpha_\phi(\mathbf{x}_p)\right)\right) \\ & + \Psi_c^{\chi}\left((\mathbf{x})\cos\left(\omega_\chi t + 2\alpha_\chi(\mathbf{x})\right) - \cos\left(\omega_\chi(t - D) + 2\alpha_\chi(\mathbf{x}_p)\right)\right).\end{aligned} \quad (2.2.18)$$

By plugging (2.2.18) into the equation for the change in arrival time (2.2.16) and subtracting the average value of the period, we are able to arrive at the expression for the time-dependent part of the timing residual at time t:

$$\begin{aligned}\Delta t(t) = {} & \frac{2\Psi_c^{\phi}}{\omega_\phi}\sin\left(\frac{\omega_\phi D}{2} + \alpha_\phi(\mathbf{x}) - \alpha_\phi(\mathbf{x}_p)\right) \\ & \times\cos\left(\omega_\phi t + \alpha_\phi(\mathbf{x}) + \alpha_\phi(\mathbf{x}_p) - \frac{\omega_\phi D}{2}\right) \\ & + \frac{2\Psi_c^{\chi}}{\omega_\chi}\sin\left(\frac{\omega_\chi D}{2} + \alpha_\chi(\mathbf{x}) - \alpha_\chi(\mathbf{x}_p)\right) \\ & \times\cos\left(\omega_\chi t + \alpha_\chi(\mathbf{x}) + \alpha_\chi(\mathbf{x}_p) - \frac{\omega_\chi D}{2}\right).\end{aligned} \quad (2.2.19)$$

In contrast with [95], this time residual is oscillating in time with two frequencies, ω_ϕ and ω_χ. As a result, we can now find the amplitudes of the system:

$$\Delta t(t) = A_\phi \cos\left(\omega_\phi t + \alpha_\phi(\mathbf{x})\right) + A_\chi \cos\left(\omega_\chi t + \alpha_\chi(\mathbf{x}_p)\right), \quad (2.2.20)$$

where,
$A_\phi = \frac{2\Psi_c^\phi}{\omega_\phi} \sin\left(\frac{\omega_\phi D}{2} + \alpha_\phi(\mathbf{x}) - \alpha_\phi(\mathbf{x}_p)\right)$ and
$A_\chi = \frac{2\Psi_c^\chi}{\omega_\chi} \sin\left(\frac{\omega_\chi D}{2} + \alpha_\chi(\mathbf{x}) - \alpha_\chi(\mathbf{x}_p)\right)$ are the amplitudes of the two scalars.

The time residual is averaged over a period which is equivalent to the minimum point where the plots of the two scalar fields intersect. If the largest period $P = \frac{2\pi}{W}$ is an integer multiple of the periods of the scalar fields ($\frac{2\pi}{\omega_\phi}$ and $\frac{2\pi}{\omega_\chi}$) then the amplitude is [1]

$$\Delta t_{DM} = \sqrt{A_\phi^2 + A_\chi^2}\,, \tag{2.2.21}$$

which gives

$$\Delta t_{DM} = \left[\left(\frac{2\Psi_c^\phi}{\omega_\phi} \sin\left(\frac{\omega_\phi D}{2} + \alpha_\phi(\mathbf{x}) - \alpha_\phi(\mathbf{x}_p)\right)\right)^2 + \left(\frac{2\Psi_c^\chi}{\omega_\chi} \sin\left(\frac{\omega_\chi D}{2} + \alpha_\chi(\mathbf{x}) - \alpha_\chi(\mathbf{x}_p)\right)\right)^2\right]^{\frac{1}{2}}. \tag{2.2.22}$$

We can compare the signals from the dark matter halo and gravitational wave background by averaging the square of the amplitude of the time residual over the distance to the pulsar, D:

$$\sqrt{<\Delta t_{DM}^2>} = \sqrt{\frac{2\,\Psi_c^{\phi^2}}{\omega_\phi^2} + \frac{2\,\Psi_c^{\chi^2}}{\omega_\chi^2}}. \tag{2.2.23}$$

Since (2.2.19) takes the form of the time delay that implies that the correct frequency for of the mode, $\bar{\omega}$ is the common divisor of $(\omega_\phi, \omega_\chi)$. This is associated with smaller mass $\bar{m}$. Where n_ϕ and n_χ are numbers, as a result here are some definitions: $\omega_\phi = 2\,n_\phi\,\bar{\omega}$; $\omega_\chi = 2\,n_\chi\,\bar{\omega}$; $2\,\bar{m} = \bar{\omega}$

[1] (2.2.21) is true if ω_ϕ an ω_χ are different. If $\omega_\chi = \omega_\phi$ then we have

$$\frac{\pi\left(A_\phi^2 + A_\chi^2 + 2\,A_\phi\,A_\chi\cos\left(\alpha(\mathbf{x}) - \alpha(\mathbf{x}_p)\right)\right)}{\omega_\phi}.$$

It can be seen that the system is now dependent on the phases, where as when the frequencies were different there was no dependence.

The average of the square of (2.2.22) over the distance to the pulsar D gives

$$\sqrt{\langle \Delta t_{DM}^2 \rangle} = \sqrt{2}\sqrt{\frac{\Psi_c^{\phi^2}}{\omega_\phi^2} + \frac{\Psi_c^{\chi^2}}{\omega_\chi^2}} = \frac{1}{\sqrt{2}\,\bar{\omega}}\sqrt{\frac{\Psi_c^{\phi^2}}{n_\phi^2} + \frac{\Psi_c^{\chi^2}}{n_\chi^2}}. \tag{2.2.24}$$

Going back to (2.2.15) we see that it gives us the relation between the amplitude of the scalars and the energy density of the system resulting in the expression for the energy density

$$\frac{m_\phi^2}{2} A_\phi^2 + \frac{m_\chi^2}{2} A_\chi^2 \simeq \#\left(m_\phi^2\, \Psi_c^{\phi^2} + m_\chi^2\, \Psi_c^{\chi^2}\right). \tag{2.2.25}$$

This implies the following expression

$$\Psi_c^{\phi^2} = \frac{\rho_{DM}}{m_\phi^2}\left(1 + \frac{n_\chi^2}{n_\phi^2}\frac{\Psi_c^{\chi^2}}{\Psi_c^{\phi^2}}\right)^{-1}. \tag{2.2.26}$$

When coupling the system with a gravitational wave, we get the solution for the characteristic strain of the gravitational wave, h_c, also known as its amplitude

$$h_c = \frac{1}{\sqrt{2}}\sqrt{\frac{\Psi_c^{\phi^2}}{n_\phi^2}\frac{\Psi_c^{\chi^2}}{n_\chi^2}} = \frac{1}{\sqrt{2}}\frac{\Psi_c^{\phi^2}}{n_\phi}\sqrt{1 + \frac{\Psi_c^{\phi^2}}{\Psi_c^{\chi^2}}\frac{n_\phi^2}{n_\chi^2}}, \tag{2.2.27}$$

$$h_c \simeq \frac{\rho_{DM}}{\bar{\omega}^2}\frac{1}{n_\phi^3}\left[1 + \frac{n_\chi^2}{n_\phi^2}\frac{\Psi_c^{\chi^2}}{\Psi_c^{\phi^2}}\right]^{-1}\left(1 + \frac{\Psi_c^{\phi^2}}{\Psi_c^{\chi^2}}\frac{n_\phi^2}{n_\chi^2}\right)^{\frac{1}{2}}. \tag{2.2.28}$$

Now that we have successfully found the solution for the characteristic strain of the system, we want to compare it with the result for the single field case published in the paper by Khmelnitsky and Rubakov [95]. The following cases are plotted for different values of n_ϕ and n_χ

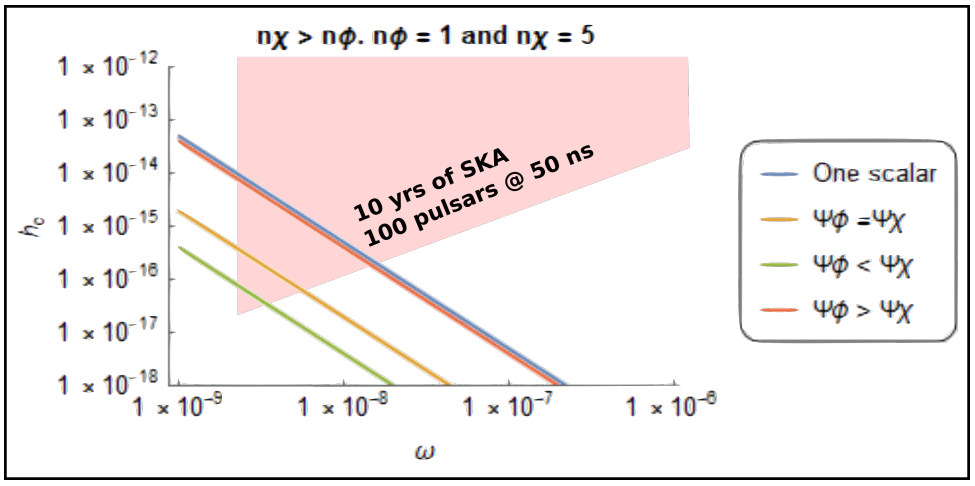

FIGURE 2.1: Characteristic strain (h_c) vs frequency ω. Comparing with single field case when $n_\phi = 1$ and $n_\chi = 5$ when changing the values of $\Psi_c^{\phi^2}$ and $\Psi_c^{\chi^2}$. It is also compared with the observation range of the Square Kilometre Array (SKA).

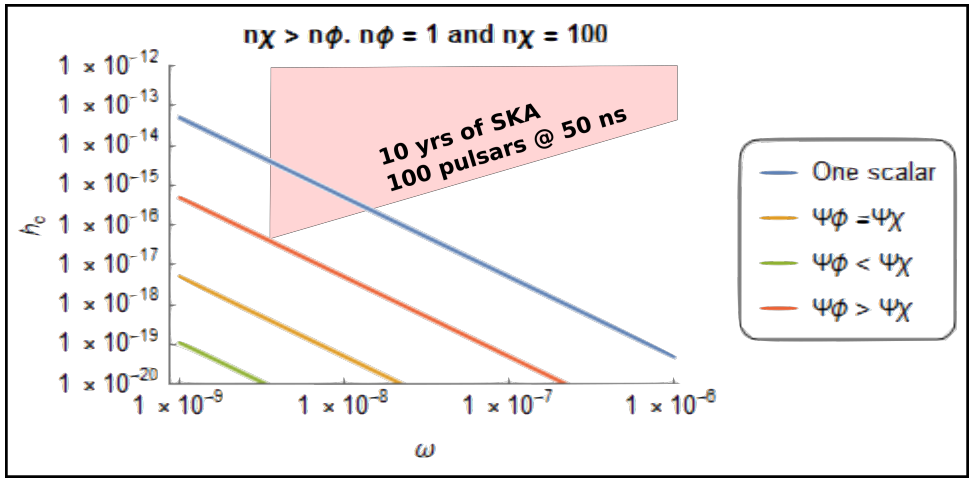

FIGURE 2.2: Characteristic strain (h_c) vs frequency ω. Comparing with single field case when $n_\phi = 1$ and $n_\chi = 100$. When changing the values of $\Psi_c^{\phi^2}$ and $\Psi_c^{\chi^2}$. It is also compared with the observation range of the Square Kilometre Array (SKA).

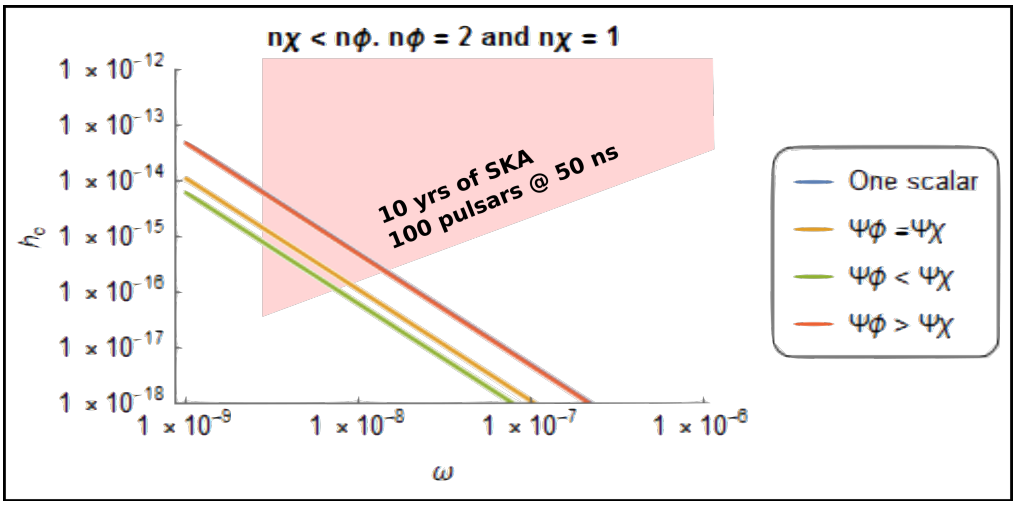

FIGURE 2.3: Characteristic strain (h_c) vs frequency ω. Comparing with single field case when $n_\phi = 2$ and $n_\chi = 1$. When changing the values of $\Psi_c^{\phi^2}$ and $\Psi_c^{\chi^2}$. It is also compared with the observation range of the Square Kilometre Array (SKA).

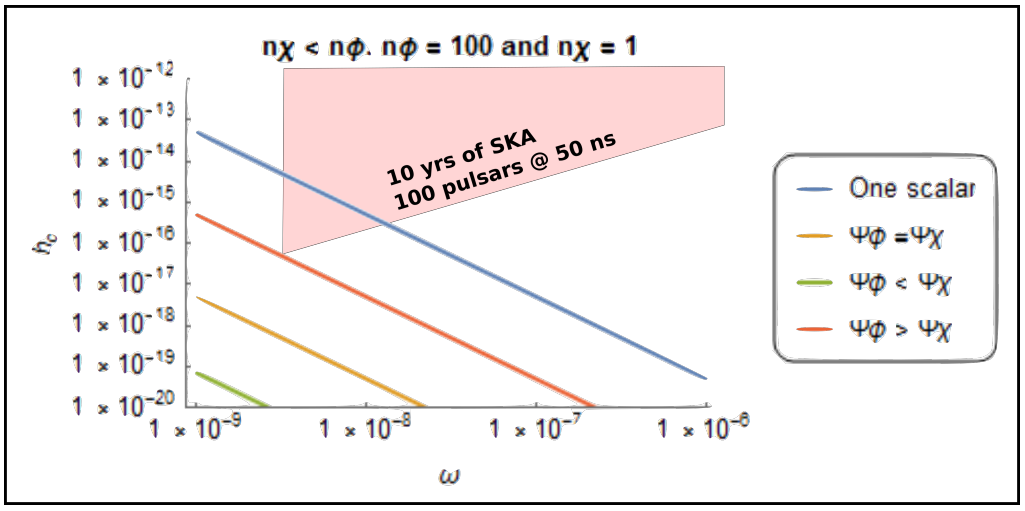

FIGURE 2.4: Characteristic strain (h_c) vs frequency ω. Comparing with single field case when $n_\phi = 100$ and $n_\chi = 1$. When changing the values of $\Psi_c^{\phi^2}$ and $\Psi_c^{\chi^2}$. It is also compared with the observation range of the Square Kilometre Array (SKA).

Unfortunately *FIGURE 2.3* shows the best solution that the multi-field system was able to achieve. The case where $\Psi_\phi > \Psi_\chi$ (red) gives the highest values for the characteristic strain. It almost matches the single scalar solution (blue). Unfortunately, none of our results were able to better the solution provided by Khmelnitsky and Rubakov. Looking at the original paper [95], we can see that the scalar field dark matter solution crosses

through a proposed future limit which would be achieved after the Square Kilometre Array has been observing pulsars for a period of 10 years. This paper was produced in 2013 therefore the current limit is perhaps out of date. The current limit given by SKA is shown on the figures above. Some of the lines do cross into the observable regions however, the purpose was to improve on the original result by increasing the characteristic strain. As a decoupled system is unable to achieve this, we now aim to improve upon the original result, by proposing a coupled system.

2.3 Magnetised ultra-light dark matter. Coupling Dark Matter to Dark Energy

In this section, we will expand on the multi-field system that was used previously but now it is a coupled system. The coupled system we wish to construct consists of magnetised ultra-light dark matter. This is achieved by attempting to couple dark matter to dark energy. If successful, not only would we have a good candidate for dark matter, but we would also be furthering our understanding of the even more mysterious universal entity, Dark Energy.

2.3.1 Motivations

Our coupled system is motivated by ultra-light scalars, e.g. axions, which are an attractive candidate for dark matter as we have stated previously in this chapter. In particular, the mass range $m_a \simeq 10^{-23} - 10^{-24}$ eV is interesting as it is able to mimic warm dark matter through fuzzy quantum effects as discussed in [45, 126]. As was described earlier, the warm dark matter could possibly be detected through pulsar timing variations [95]. We explore the possibility that such scalars couple to dark energy with lower dimensional operators. This fact changes their dynamics, in an interesting

way. In particular providing a 'see-saw' mechanism to reduce axion mass and enlarging the mass range that makes them interesting for dark matter.

2.3.2 System under consideration

The system we are considering consists of two scalar fields φ, χ. They span an internal two dimensional field space, with flat metric $g_{ab} = \delta_{ab}$. They can be conveniently expressed in components as

$$\Phi_a = (\varphi, \chi) \tag{2.3.1}$$

The two scalars have two masses m_φ, m_χ, which we consider comparable (of the same order).

Additionally, we consider a preferred vector direction u^μ, whose vacuum expectation value is controlled by its own dynamics that we do not control, and with time-like component turned on

$$u^\mu = (B, 0, 0, 0)' \tag{2.3.2}$$

where u^μ is a Lorentz-violating time-like unit vector field which satisfies the condition

$$g_{\mu\nu} u^\mu u^\nu = -1. \tag{2.3.3}$$

Such a condition can be enforced by a Lagrange multiplier. There are many examples of this in the literature e.g. time-like vectors, from Einstein-aether to chronon inflation [127]. These scenarios can be well motivated are exciting and motivate us to pursue the Dark Energy problem. We shall consider the following action

$$\mathcal{S} = \int d^4x \sqrt{-g} \left[\frac{M_P^2}{2} R - \mathcal{L} \right], \tag{2.3.4}$$

with the scalar action given by

$$\mathcal{L} = \frac{g^{\mu\nu}}{2}\,\partial_\mu\Phi_a\,\partial_\nu\Phi_b\,\delta^{ab} + \frac{1}{2}\,\epsilon^{ab}\,(\partial_\mu\Phi_a)\;\Phi_b\,u_\nu\,g^{\mu\nu} + \frac{m^2}{2}\,\Phi_a\;\Phi_b\,\delta^{ab}. \tag{2.3.5}$$

This action is strongly motivated by [128]. The system is placed in FRW geometry, $ds^2 = -dt^2 + a^2(t)d\vec{x}^2$. Consider homogeneous scalars, $\varphi = \varphi(t)$, $\chi = \chi(t)$. Then the energy momentum tensor for the homogeneous system results

$$T_{00} = \frac{1}{2}\dot{\Phi}_a\,\dot{\Phi}_b\,\delta^{ab} + \frac{B}{2}\,\epsilon^{ab}\,\dot{\Phi}_a\,\Phi_b + \frac{m^2}{2}\,\Phi_a\;\Phi_b\,\delta^{ab}, \tag{2.3.6}$$

$$T_{ij} = \frac{1}{2}\dot{\Phi}_a\,\dot{\Phi}_b\,\delta^{ab} + \frac{B}{2}\,\epsilon^{ab}\,\dot{\Phi}_a\,\Phi_b - \frac{m^2}{2}\,\Phi_a\;\Phi_b\,\delta^{ab}. \tag{2.3.7}$$

We shall use this expression for the energy momentum tensor, for solving calculations analogous to Rubakov [95]. The homogeneous equations for the two fields (φ and χ) are more conveniently expressed in terms of complex field, Γ

$$\Gamma(t) = \varphi(t) + i\,\chi(t). \tag{2.3.8}$$

We get the following equation of motion

$$\ddot{\Gamma} + 3H\dot{\Gamma} - i\,B\,\dot{\Gamma} + m^2\,\Gamma = 0, \tag{2.3.9}$$

Now we shall redefine the field

$$\Gamma(t) = \frac{e^{\frac{i}{2}\,B\,t}}{a^{3/2}}\,Q(t). \tag{2.3.10}$$

Putting the redefinition of gamma back into (2.3.8) reduces the equation as follows

$$\ddot{Q} + \left[m^2 + \frac{B^2}{4} + \frac{3i}{2}\,B\,H - \frac{9}{4}\,H^2 + 6\,\epsilon_H\,H^2\right] Q = 0. \tag{2.3.11}$$

Suppose that we impose the condition $m, B \gg H$ on the system. This results in all terms that include H becoming negligible. In this regime, the

equation of motion becomes

$$\ddot{Q} + \left[m^2 + \frac{B^2}{4}\right] Q = 0. \tag{2.3.12}$$

As we can see the solution which appears due the condition being imposed is a simple plane wave with frequency $w = \sqrt{m^2 + B^2/4}$:

$$Q = q_1\, e^{iwt+i\phi_1} + q_2\, e^{-iwt-i\phi_2}, \tag{2.3.13}$$

where $w_{1,2}$ frequencies and $q_{1,2}$ and $\phi_{1,2}$ are real constants. Then the configuration for Γ now reads

$$\Gamma = \frac{1}{a^{3/2}} \left[q_1\, e^{iw_1 t+i\phi_1} + q_2\, e^{-iw_2 t-i\phi_2}\right], \tag{2.3.14}$$

with

$$w_1 = \left(w + B/2\right), \tag{2.3.15}$$

$$w_2 = \left(w - B/2\right). \tag{2.3.16}$$

We now assume a new condition, $B \gg m$ for simplicity. Then we have

$$w_1 = w + B/2 \simeq B, \tag{2.3.17}$$

$$w_2 = w - B/2 \simeq \frac{m^2}{B}. \tag{2.3.18}$$

Since $\frac{m^2}{B} \ll 1$, the second frequency is much smaller than the first ($B >> \frac{m^2}{B}$) and we are able to decompose Γ

$$\begin{aligned}\Gamma = {} & \frac{1}{a^{3/2}} \left[q_1 \cos\left(B\, t + \phi_1\right) + q_2 \cos\left(\frac{m^2}{B}\, t + \phi_2\right)\right] \\ & + \frac{i}{a^{3/2}} \left[q_1 \sin\left(B\, t + \phi_1\right) - q_2 \sin\left(\frac{m^2}{B}\, t + \phi_2\right)\right].\end{aligned} \tag{2.3.19}$$

From the definition of Γ, we are able to obtain the solutions for our two scalar fields

$$\varphi = \frac{1}{a^{3/2}}\left[q_1 \cos\left(B\,t + \phi_1\right) + q_2 \cos\left(\frac{m^2}{B}\,t + \phi_2\right)\right], \tag{2.3.20}$$

$$\chi = \frac{1}{a^{3/2}}\left[q_1 \cos\left(B\,t + \phi_1 - \frac{\pi}{2}\right) + q_2 \cos\left(\frac{m^2}{B}.\,t + \phi_2 + \frac{\pi}{2}\right)\right]. \tag{2.3.21}$$

We now assume that B is multiple of m^2/B. Perhaps there are reasonable initial conditions which further fix some of the parameters of the scalar field solutions, for example $\dot{\varphi} = \dot{\chi} = 0$ at $t = 0$.

We can forget this in the meantime, as we first focus on φ. We assume $q_1 \ll q_2$. It is a mode with quite low frequency/long period, whose shape is slightly changed by rapidly oscillating component proportional to q_1. For χ it is the same thing, however, the phase of the mode is shifted by $\pi/2$. The benefit of this scenario is that we are able to achieve a longer period through a kind of 'see-saw' mechanism.

We have two scenarios to test for different values of B

- If $B \sim 10^{-2}eV$ (order of neutrino mass), with $m \sim 10^{-12}eV$ (lower bound on scale of QCD axion) we get $m^2/B \sim 10^{-22}eV$.
- If $B \sim 10^{9}eV$ (TeV scale of new physics) with $m \sim 10^{-6}eV$ (scale of QCD axion) we get $m^2/B \sim 10^{-22}eV$.

We first check that our axion mass ($\simeq 10^{-22}eV$) that can be obtained when B is of the same order as the neutrino mass ($\simeq 10^{-2}eV$). If we are able to obtain it with a much larger value for B. Achieving the axion mass at this range gives the possibility of new physics.

Before probing these scales we must first check the hypothesis $q_1 \ll q_2$ and work out the properties of the system. Then after showing that our system is a viable dark matter candidate we can the study the consequences for

modulation of pulsar timing. We begin in the regime $q_1 \ll q_2$, then in we study the system in general.

2.3.3 Regime $q_1 \ll q_2$

We begin with the regime where $q_1 \ll q_2$ so the scalars (2.3.20) and (2.3.21) now take the following form

$$\varphi = \frac{1}{a^{3/2}}\left[q_2 \cos\left(\frac{m^2}{B}\, t + \phi_2\right)\right], \tag{2.3.22}$$

$$\chi = \frac{1}{a^{3/2}}\left[q_2 \cos\left(\frac{m^2}{B}\, t + \phi_2 + \frac{\pi}{2}\right)\right]. \tag{2.3.23}$$

From this we are able to produce the following solutions for the energy density (which comes from the T_{00} component of energy-momentum tensor) and pressure (comes from the T_{ij} component),

$$\rho_{DM} = \frac{q_2^2}{a^3}\, m^2, \tag{2.3.24}$$

$$p = \frac{q_2^2}{2\, a^3}\frac{m^4}{B^2}. \tag{2.3.25}$$

As was mentioned previously, the condition $B \gg m$ was imposed on the system therefore the energy density is much larger than the pressure, as a result, the system can still be considered a possible dark matter candidate.

Now that the essential conditions have been established we are able to continue with the method from [95] which was used for the uncoupled system in the previous section.

In this new coupled case the gravitational potential now takes the following form:

$$\Psi(\mathbf{x}, t) = \Psi_0(\mathbf{x}) + \Psi_c^{\varphi}(\mathbf{x}) \cos(\omega\, t + \phi_2) + \Psi_c^{\chi}(\mathbf{x}) \cos\left(\omega\, t + \phi_2 + \frac{\pi}{2}\right), \tag{2.3.26}$$

where frequency ω is equivalent to mass $\frac{m^2}{B}$.

If we remember from the original case that $\Psi_0(\mathbf{x})$ is equal to zero and since both fields have the same frequency Ψ_s is non-zero. Ψ_c^{χ} is out of phase with Ψ_c^{ϕ} by $\frac{\pi}{2}$ so Ψ is rewritten as

$$\Psi(\mathbf{x},t) = \Psi_c^{\varphi}(\mathbf{x})\cos(\omega t + \phi_2) - \Psi_s^{\chi}(\mathbf{x})\cos(\omega t + \phi_2). \tag{2.3.27}$$

As we have the solution for the gravitational potential, the timing residual (2.2.16) can now be expressed

$$\begin{aligned}\Delta t(t) = -\int_0^t \Psi_c\left(\cos(\omega_2 t + 2\phi_2(\mathbf{x})) - \cos(\omega_2(t-D) + 2\phi_2(\mathbf{x}_p))\right)\\ -\Psi_s\left(\sin(\omega t + 2\phi_2(\mathbf{x})) + \sin(\omega(t-D) + 2\phi_2(\mathbf{x}_p))\right)dt'.\end{aligned} \tag{2.3.28}$$

With this expression we are able to solve the integral which leads the following result for the timing residual.

$$\begin{aligned}\Delta t(t) = \frac{2}{\omega}\sin\left(\frac{\omega D}{2} + \phi_2(\mathbf{x}) - \phi_2(\mathbf{x}_p)\right)\\ \left(\Psi_c\cos\left(\omega t + \phi_2(\mathbf{x}) + \phi_2(\mathbf{x}_p) - \frac{\omega D}{2}\right)\right.\\ \left.-\Psi_s\sin\left(\omega t + \phi_2(\mathbf{x}) + \phi_2(\mathbf{x}_p) - \frac{\omega D}{2}\right)\right).\end{aligned} \tag{2.3.29}$$

From this we obtain the solution for the amplitude of the timing residual

$$\Delta t_{DM} = \frac{2}{\omega}\sin\left(\frac{\omega D}{2} + \phi_2(\mathbf{x}) - \phi_2(\mathbf{x}_p)\right). \tag{2.3.30}$$

Similar to the uncoupled case, we can compare our signals from the dark matter galactic halo with the gravitational wave background (can be found in [95]). The root mean square of the dark matter amplitude is given as

$$\sqrt{<\Delta t_{DM}^2>} = \sqrt{\frac{(\Psi_c^2 + \Psi_s^2)}{\omega^2}}. \tag{2.3.31}$$

We now reintroduce the frequency that was defined as $\omega = \frac{m^2}{B}$ and put it back into (2.3.31)

$$\sqrt{< \Delta t_{DM}^2 >} = \sqrt{\frac{B^2 \left(\Psi_c^2 + \Psi_s^2\right)}{m^4}}. \tag{2.3.32}$$

By looking at the result we have found for the RMS of the dark matter amplitude we see that there is little reason to plot the results for the amplitude against frequency in this regime ($q_1 \ll q_2$) as we would be left with the result given in [95] and would not be able to improve upon it. This is the same issue as we had in the uncoupled case. Our aim, in this chapter, is to try and find an upper bound for the vector field in order to, perhaps, increase the mass of the axions from $10^{-22}eV$, which would therefore increase the characteristic strain of the dark matter signal (as they are of the same order). In an effort to achieve this aim we move on to the general regime where q_1 is now non-zero.

2.3.4 Regime $q_1 \neq 0$

Now that it has been shown that the system is still a dark matter candidate when $q_1 = 0$ but cannot improve on the single field case [95], the general case can be solved. The scalars are still of the same form as (2.3.20) and (2.3.21) respectively.

With $q_1 \neq 0$ we now have two masses/frequencies to deal with. The gravitational potential Ψ can be rewritten in the following form

$$\begin{aligned}\Psi(\mathbf{x}, t) = \Psi_0(\mathbf{x}) + \Psi_c^{\varphi}(\mathbf{x}) \cos(\omega_1 t + \phi_1) + \Psi_c^{\varphi}(\mathbf{x}) \cos(\omega_2 t + \phi_2) \\ + \Psi_c^{\chi}(\mathbf{x}) \cos\left(\omega_1 t + \phi_1 - \frac{\pi}{2}\right) + \Psi_c^{\chi}(\mathbf{x}) \cos\left(\omega_2 t + \phi_2 + \frac{\pi}{2}\right),\end{aligned} \tag{2.3.33}$$

where the frequencies are defined as: $\omega_1 = B$ and $\omega_2 = \frac{m^2}{B}$.

Although the structure of (2.3.33) only contains cosine functions we are still able to obtain sine functions in the expression for the gravitational

potential. This is because the cosine components that involve the scalar field χ contain $+/-\frac{\pi}{2}$, therefore they can be changed to -sine function. Resulting in a sine and cosine components for each mass. The expression for the gravitational potential now reads as follows

$$\begin{aligned}\Psi(\mathbf{x},t) &= \Psi_c(\mathbf{x})\cos(\omega_1 t+\phi_1) - \Psi_c(\mathbf{x})\cos(\omega_2 t+\phi_2)\\ &-\Psi_s(\mathbf{x})\sin\left(\omega_1 t+\phi_1-\frac{\pi}{2}\right)+\Psi_s(\mathbf{x})\sin\left(\omega_2 t+\phi_2+\frac{\pi}{2}\right).\end{aligned} \tag{2.3.34}$$

With the full solution for the gravitational potential we can now produce the expression for the change in arrival time (2.2.19) in the general regime ($q_1 \neq 0$)

$$\begin{aligned}&\Delta t(t) = -\left(\Psi_c^2+\Psi_s^2\right)\\ &\left(q_2^2\cos\left(\frac{D\,m^2}{B}+\phi_2(x)-\phi_2(\mathbf{x}_p)\right)+q_1^2\cos(\phi_1(\mathbf{x})-\phi_1(\mathbf{x}_p))-q_1^2-q_2^2\right).\end{aligned} \tag{2.3.35}$$

The expression can be further simplified by setting $\frac{B^2}{m}$ to 2π. This gets rid of the ϕ_2 phase so we only have on phase to deal with.

By taking the average over the distance to the pulsar, D this gives us the solution for the amplitude of the dark matter system

$$\Delta t_{DM} = -\left(\Psi_c^2+\Psi_s^2\right)\left(-q_1^2-q_2^2+q_1^2\cos\left(\phi_1(\mathbf{x})-\phi_1(\mathbf{x}_p)\right)\right). \tag{2.3.36}$$

Further simplification is needed as there is still a cosine term containing phases (only ϕ_1 as ϕ_2 was removed from the expression when $\frac{B^2}{m}$ was set to $2\,\pi$), so averaging over the phase and taking the square root leaves the following

$$\sqrt{<\Delta t_{DM}^2>} = \sqrt{\left(q_1^2+q_2^2\right)\left(\Psi_c^2+\Psi_s^2\right)}. \tag{2.3.37}$$

As we have previously mentioned we would like to find an upper bound for the vector field in order to perhaps increase the mass of the ultra-light cosmological axions from $10^{-22}eV$, which would increase the characteristic

strain of the dark matter signal making the axion easier to detect. In order to do this some initial conditions need to be imposed upon the system. Firstly we need to understand the misalignment mechanism that is used in the production of axions. From this understanding we will be able to discuss the possible initial conditions that could be imposed on our system.

Most of the information about the misalignment mechanism and initial conditions we are taking are from a review on axion cosmology by David J.E. Marsh [32] which presents a far more detailed discussion on the topic.

2.3.5 Misalignment and Initial Conditions

The misalignment mechanism or vacuum realignment is a model independent production mode for axions. It relies on being associated to spontaneous symmetry breaking and axions being a pseudo Nambu Goldstone Boson (pNGB). It depends only on gravitational interactions and self interactions [32].

Background evolution

We begin with the axion equation of motion

$$\ddot{\phi} + 3H\dot{\phi} + m_a^2\,\phi = 0. \tag{2.3.38}$$

From this we can obtain the background energy density and pressure expressions of the axion field (from the energy-momentum tensor):

$$\bar{\rho}_a = \frac{1}{2}\,\dot{\phi}^2 + \frac{1}{2}\,m_a^2\,\phi^2, \tag{2.3.39}$$

$$\bar{P}_a = \frac{1}{2}\,\dot{\phi}^2 - \frac{1}{2}\,m_a^2\,\phi^2. \tag{2.3.40}$$

In a matter or radiation dominated Universe the scale factor evolves as a power law, $a \propto t^p$. This gives an exact solution of the axion field ϕ from

(2.3.38):

$$\phi = a^{-\frac{3}{2}} \left(\frac{t}{t_i}\right)^{\frac{1}{2}} \left[C_1 J_n\left(m_a t\right) + C_2 Y_n\left(m_a t\right)\right], \tag{2.3.41}$$

where $n = \frac{(3p-1)}{2}$, $J_n\left(x\right)$, $Y_n\left(x\right)$ are known as Bessel functions of the first and second kind respectively, and t_i is the initial time. C_1 and C_2 are constants determined by the initial conditions. These are well defined for axions in the vacuum realignment mode when $H\left(t_i\right) \gg m_a$:

$$\phi\left(t_i\right) = f_a\, \phi_{a,i},\ \dot{\phi}\left(t_i\right) = 0. \tag{2.3.42}$$

Misalignment Production of Dark Matter Axions

By using the initial condition of (2.3.42) the misalignment production of Dark Matter axions can be calculated. At the point of symmetry breaking the Hubble rate is much larger than the axion mass and as a result the field becomes overdamped. This initially sets $\dot{\phi} = 0$. The homogeneous value of the field is specified by the scenario for when symmetry breaking occurs with respect to inflation. The term "Misalignment" refers to the case where there is an initial coherent displacement of the axion field, and"vacuum realignment" refers to the process by which this value relaxes to the potential minimum [32].

Axion-Like Particles

The constants from (2.3.38) C_1 and C_2 can be fixed with the initial condition $\dot{\phi} = 0$. At very early times ($H > m_a$) the axion field is overdamped and at its initial value is frozen by Hubble friction. At early times the equation of state is $w_a = -1$ and the axion behaves as a contribution to the vacuum energy. If the axion dominates the energy density while it is still overdamped with $w_a < -\frac{1}{3}$ it can drive a period of accelerated expansion. The period is determined by the ratio $\frac{H}{m_a}$ when the axion dominates over

the energy density. This in turn is fixed by the initial displacement of the field.

Later, when $H < m_a$, the axion field is underdamped and the oscillations begin. The equation of state will oscillate around $w_a = 0$ and the energy density scales as $\rho_a \propto, a^{-3}$. In this scenario the axion behaves like ordinary matter which allows the misaligned axions to be a valid dark matter candidate [32].

By defining a fixed value of the scale factor, a_{osc} and fixing the behaviour of $\rho_a(a)$ at late times the change in the axion equation of state can be approximated to be

$$\rho_a(a) \approx \rho_a(a_{osc}) \left(\frac{a_{osc}}{a}\right)^3 ; \ (a > a_{osc}) . \tag{2.3.43}$$

The energy density is approximately constant up until a_{osc} therefore $\rho_a(a_{osc}) \approx \frac{m_a^2 \phi^2}{2}$, which is the usual approximation required to calculate the energy density of the axion. Therefore it can be deduced that energy density in the misalignment population is fixed only by the mass and the initial displacement [32].

When $m_a \simeq H$, so $A H(a_{osc}) = m_a$ for some constant $A > 1$. This gives a definition for a_{osc}.

Using the misalignment mechanism, the constants in (2.3.20) and (2.3.21) can be fixed in order find the initial conditions of the system. At the beginning of the section where we discussed how we aim to find the upper bound for the ultra-light cosmological axion mass, we suggested some initial conditions that could be imposed on our coupled system which could potentially cause this larger mass to be found. The first condition we shall impose (as suggested earlier) is to set the first time derivative of the scalar field φ to zero when time is zero $\dot{\varphi}(t = 0) = 0$;

$$\dot{\varphi} = -\left(\frac{1}{2 B a_0^{\frac{3}{2}}}\right)\Big(3 B \left(q_1 \cos[\phi_1] + q_2 \cos[\phi_2]\right) H_0$$

$$+2\left(B^2\, q_1 \sin[\phi_1] + m^2\, q_2 \sin\left[\phi_2\right]\right)\Bigg) = 0. \tag{2.3.44}$$

In a similar fashion we also have the expression for the first time derivative of χ

$$\dot{\chi} = \left(\frac{1}{2\,B\,a_0^{\frac{3}{2}}}\right)\Bigg(2\,B^2\,q_1\,\cos[\phi_1] - 2\,m^2\,q_2\,\cos[\phi_2] \\ +3\,B\,H_0\left(-q_1\,\sin[\phi_1] + q_2\,\sin[\phi_2]\right)\Bigg) = 0. \tag{2.3.45}$$

We now impose the first of our initial conditions upon one of our scalar fields $\dot{\varphi}(t=0)=0$ to find an expression for the constant q_1

$$q_1 = -\frac{3\,B\,q_2\,\cos\left[\phi_2\right]\,H_0 + 2\,m^2\,q_2\,\sin[\phi_2]}{3\,B\,\cos[\phi_1]\,H_0 + 2\,B^2\,\sin[\phi_1]}. \tag{2.3.46}$$

With this solution for q_1 we are able to substitute it into (2.3.45). For simplicity ϕ_2 is set equal to $\frac{\pi}{2}$

$$\dot{\chi} = -\frac{q_2\left(B\,\cos[\phi_1]\left(4\,m^2 - 9\,H_0^2\right) - 6\left(B^2 + m^2\right)H_0\sin[\phi_1]\right)}{2\,B\,a_0^{\frac{3}{2}}\left(3\,\cos[\phi_1]\,H_0 + 2\,B\,\sin[\phi_1]\right) = 0}. \tag{2.3.47}$$

From our simplified expression all known solutions for the other phase, ϕ_1, can be found

$$\phi_1 = -\arccos\left[\frac{B\left(-4\,m^2 + 9\,H_0^2\right)\right)}{\sqrt{\left(4\,B^2 + 9\,H_0^2\right)\left(4\,m^4 + 9\,B^2\,H_0\right)}}\right], \tag{2.3.48}$$

$$\phi_1 = \arccos\left[\frac{B\left(-4\,m^2 + 9\,H_0^2\right)\right)}{\sqrt{\left(4\,B^2 + 9\,H_0^2\right)\left(4\,m^4 + 9\,B^2\,H_0\right)}}\right], \tag{2.3.49}$$

$$\phi_1 = -\arccos\left[\frac{B\left(4\,m^2 - 9\,H_0^2\right)\right)}{\sqrt{\left(4\,B^2 + 9\,H_0^2\right)\left(4\,m^4 + 9\,B^2\,H_0\right)}}\right], \tag{2.3.50}$$

$$\phi_1 = \arccos\left[\frac{B\left(4\,m^2 - 9\,H_0^2\right)\right)}{\sqrt{\left(4\,B^2 + 9\,H_0^2\right)\left(4\,m^4 + 9\,B^2\,H_0\right)}}\right]. \tag{2.3.51}$$

The expression for q_1 can be checked by substituting our solutions for ϕ_1 (2.3.48),(2.3.49),(2.3.50),(2.3.51) into (2.3.46) then simplify for q_1 [2]

$$q1 = -\frac{2\,m^2\,q_2\sqrt{(4\,B^2+9H_0^2)\,(4\,m^4+9B^2H_0^2)}}{3\,B^2\,H_0\,(4B^2+8m^2-9H_0^2)}. \tag{2.3.52}$$

Previous step is repeated by substituting (2.3.50) for ϕ_1 in to (2.3.46) yields the following [3]

$$q1 = -\frac{2\,m^2\,q_2\sqrt{\frac{4\,m^4+9\,B^2\,H_0^2}{4\,B^2+9\,H_0^2}}}{3\,B^2\,H_0}. \tag{2.3.53}$$

If we take our expression for the energy density (T_{00}) (2.3.6) and set it at misalignment then we arrive at the same solution that is mentioned in Chapter 4 of [32].

$$\rho(a_0) = \frac{1}{2}\,\dot{\varphi}^2 + \frac{1}{2}\dot{\chi}^2 + \frac{B}{2}\,(\dot{\varphi}\chi - \dot{\chi}\varphi) + \frac{m^2}{2}\,\left(\varphi^2+\chi^2\right). \tag{2.3.54}$$

Next we substitute our initial conditions, $\dot{\varphi} = 0$ and $\dot{\chi} = 0$, into the expression

$$\rho\,(a_0) = \frac{m^2}{2}\left(\varphi^2+\chi^2\right). \tag{2.3.55}$$

This leaves us with a much simpler expression. Going back to the start of the coupled system section, we remember the condition which was originally imposed for this system $B \gg m$. At misalignment it can be said that $B \gg H_0$, therefore:

$$B \gg (H_0, m)\,. \tag{2.3.56}$$

This condition means that the expressions that were acquired for ϕ_1 and q_1 can be simplified and then substituted into the equations for Γ (2.3.14) and $\rho(a_0)$ (2.3.55).

Under the condition (2.3.56), phase ϕ_1 simplifies to

$$\phi_1 = -\arccos\left[\frac{(4\,m^2-9\,H_0^2)}{2\,B+3\,H_0\,B}\right], \tag{2.3.57}$$

[2]Note that (2.3.49) yields the same result as (2.3.48) but the overall sign is positive.
[3]Note that (2.3.51) gives the same result as (2.3.50) but it is positive.

and constant, q_1 (2.3.52) becomes

$$q1 = \frac{m^2}{B^2}\, q_2. \tag{2.3.58}$$

These much simpler forms of q_1 (2.3.57) and ϕ_1 (2.3.58) can now be substituted back in to (2.3.55) $\rho(a_0)$ and Γ (2.3.14), which leaves us with the following expression for the energy density

$$\rho(a_0) = \frac{m^2\, q_2^2 \left(B^4 \, + m^4 + 2\, B^2\, m^2 \sqrt{1 - \frac{\left(4\, m^2 - 9\, H_0^2\right)^2}{(3\, B\, H_0 + 2\, B)^2}} \right)}{2\, a_0^3\, B^4}, \tag{2.3.59}$$

When the condition $B \gg (H_0, m)$ is imposed $\rho(a_0)$ can be further simplified to the form $B \gg (m, H_0)$:

$$\rho(a_0) = \frac{m^2\, q_2}{a_0^3}. \tag{2.3.60}$$

New forms of q_1 and ϕ_1 are substituted into Γ and our condition is implemented ($B \gg m$). Which leaves us with

$$\Gamma = \frac{q_2 \left(\frac{4\, m^4 - 9\, m^2\, H_0^2}{2 + 3\, H_0} - B\, i \left(B^2 + m^2 \sqrt{1 - \frac{\left(4\, m^2 - 9\, H_0^2\right)^2}{(2\, B + 3\, B\, H_0)^2}} \right) \right)}{a_0^{3/2} B^3}. \tag{2.3.61}$$

A lot of this expression can be cancelled which gives a very neat solution (which was also true for the energy density (2.3.60)).

$$\Gamma = \frac{-i\, q_2}{a_0^{\frac{3}{2}}}. \tag{2.3.62}$$

Although we have nice, simple solutions for Γ and $\rho(a_0)$, before continuing it is important to check the energy density (2.3.6) and pressure (2.3.7) for the system remembering that $B \gg m$. This is necessary in order to check that the system is still pressureless in the general regime and therefore the system can still be considered dark matter. Here are the two expression

before any conditions are implemented

$$\rho = \frac{1}{2}\left(B^2 + m^2\right)\left(a_1^2 + a_2^2\right), \tag{2.3.63}$$

$$\begin{aligned} p = &-\frac{1}{2}\left(B^2 + m^2\right)\left(a_1^2 + a_2^2\right)\cos\left(Bt + \phi_1\right) + \\ &\cos\left(Bt + \phi_1 - \frac{\pi}{2}\right) + \cos\left(\frac{m^2}{B} + \phi_2\right) + \cos\left(\frac{m^2}{B} + \phi_2 + \frac{\pi}{2}\right). \end{aligned} \tag{2.3.64}$$

Now we use the condition $B \gg m$ to check the pressure of our coupled system:

$$\begin{aligned} p = &\left(\frac{1}{2}B^2\left(-a_1^2 - a_2^2\right) - \frac{1}{2}m^2\left(a_1^2 + a_2^2\right)\right)\sin(B\,t + \phi_1) \\ &+\left(\frac{1}{2}B^2\left(-a_1^2 - a_2^2\right) - \frac{1}{2}m^2\left(a_1^2 + a_2^2\right)\right)\cos(B\,t + \phi_1) \\ &-\frac{1}{2}B^2\left(a_1^2 + a_2^2\right)\left(\cos(\phi_2) - \sin(\phi_2)\right) \\ &+\frac{1}{2}B\left(a_1^2 + a_2^2\right)\left(m^2\,t\sin(\phi_2) + m^2\cos(\phi_2)\right) \\ &+\frac{1}{4}\left(-a_1^2 - a_2^2\right)\left(m^4\sin(\phi_2) - m^4\,t^2\cos(\phi_2)\right) \\ &-\frac{1}{2}m^2\left(a_1^2 + a_2^2\right)\left(\cos(\phi_2) - \sin(\phi_2)\right). \end{aligned} \tag{2.3.65}$$

In order for the system to be pressureless it should have terms which depend on the lower frequency. However, in this regime there is no part of (2.3.64) which depends on the lower frequency $\frac{m^2}{B}$. The system does oscillate but only with the higher frequency B. As a result the system, unfortunately, is not pressureless and therefore it cannot be considered as a dark matter candidate. It seems that the system can only be a dark matter candidate with a constraint that sets one of the constants to zero (q_1). Otherwise we end up with a system where the energy density is not much larger than the pressure due to p having a dependence on the larger frequency. However, the case where we are confined to one constant q_2 we are unable to improve upon what was proposed by Rubakov in [95]. So we have been unable to improve the mass range of the cosmological axion. Even a system coupling

it to dark energy has not been successful - no new physics. Either a new system should be put forward to find a new upper bound or perhaps future Pulsar Timing Array experiments will improve their observation range and will be able to detect ultra-light axions in the known mass range ($10^{-22}eV$ – $10^{-33}eV$).

Conclusions

Our aim for this chapter was to create a multi field system of ultra-light scalar fields which could increase the mass range of the cosmological axion (and therefore increasing its frequency) into the observation range of current pulsar timing arrays. This required improving upon the single field solution provided by [95]. Beginning with the uncoupled system the highest characteristic strain that could be achieved was identical to the single field case from the paper we based this work on. We then attempted a system where we coupled our dark matter to dark energy (an even more mysterious component of the Universe), however when we had more than one constant to contend with (general solution) we were unable to produce an expression for the pressure perturbations (from the energy momentum tensor) which was much smaller than the energy density of the system. This meant that the system was not pressureless and therefore no longer a dark matter candidate.

In the next chapter we move on to a form an inflation which could enhance stochastic background primordial gravitational waves and tensor non-Gaussianties so they could be detected by present interferometers. From this we will apply this work to the detection of tensor and scalar polarisations in the final chapter.

Chapter 3

Squeezed tensor non-Gaussianity in non-attractor inflation

This chapter consists of this paper [1] which was published in the jounral JCAP.

We investigate primordial tensor non-Gaussianity in single field inflation, during a phase of non-attractor evolution when the spectrum of primordial tensor modes can be enhanced to a level detectable at interferometer scales. Making use of a tensor duality we introduced in [123], we analytically compute the full bispectrum of primordial tensor fluctuations during the non-attractor era. During this epoch the shape of the tensor bispectrum is enhanced in the squeezed limit, its amplitude can be amplified with respect to slow-roll models, and tensor non-Gaussianity can exhibit a scale dependence distinctive of our set-up. We prove that our results do not depend on the frame used for the calculations. Squeezed tensor non-Gaussianity induces a characteristic quadrupolar anisotropy on the power spectrum of the stochastic background of primordial tensor perturbations.

As a step to make contact with gravitational wave experiments, we discuss the response function of a ground based Michelson interferometer to a gravitational wave background with such a feature.

3.1 Introduction

The possibility to directly detect a stochastic background of primordial tensor modes with gravitational wave experiments would offer new ways to probe the physics of inflation. Such an opportunity would allow us to probe a much larger range of frequency scales than what can be tested with CMB physics. Various scenarios have been proposed for enhancing the primordial tensor spectrum at interferometer scales: from coupling the inflation to additional fields, whose dynamics are characterised by instabilities that amplify the tensor spectrum (see e.g. [129–151]), to models that break space-time symmetries during inflation, leading to a blue spectrum for primordial tensor modes (see e.g. [152–164]). See the general discussion in [165].

In this work, we focus on a third possibility, and further develop on the idea introduced in [123]. We investigate single field scenarios in which the inflationary expansion undergoes a brief phase of non-attactor dynamics that amplify the tensor modes. Non-attractor cosmological evolution is known to enhance the scalar sector of fluctuations, for example during ultra-slow roll or in constant roll inflationary systems [166–174]: this property has been exploited in models producing primordial black holes in single field inflation (see e.g. [175–177] for reviews and [178–186] for specific models). In [123] we showed that a similar behaviour can apply to the primordial tensor sector, if we non-minimally couple the inflationary scalar field with gravity during inflation. During the non-attractor phase, the amplitude of the would be decaying tensor mode becomes amplified instead of suppressed

at superhorizon scales (while the usual growing mode has constant amplitude), and the total tensor spectrum can be enhanced to a level detectable with gravitational wave experiments. Interestingly, there exists a 'tensor duality' (which generalises to the tensor sector a similar duality for the scalar sector [187]) which maps the evolution of tensor fluctuations during the non-attractor phase to the dynamics of tensor fluctuations in a slow-roll phase of expansion. We use the duality to obtain an analytic control on the physics of tensor modes during the phase of non-attractor evolution – even if we are far from a slow-roll approximation – and to *analytically compute* the properties of tensor non-Gaussianity during the non-attractor phase. Tensor non-Gaussianity is an interesting observable which can help to characterise and distinguish different scenarios of inflation that enhance tensor modes at small or large frequency scales (see e.g. [147, 150, 188–198] and the review in Section 5 of [199] for more a comprehensive reference list). In our framework, tensor non-Gaussianity is characterised by the following properties, which we are going to discuss in what follows:

- The amplitude of the tensor bispectrum during the non-attractor evolution can be enhanced with respect slow-roll inflation, and its shape is amplified in a squeezed limit. We analytically show that the tensor bispectrum exhibits a characteristic scale dependence distinctive of our scenario, which can make our model quantitatively distinguishable from other frameworks with large tensor non-Gaussianity.

- We show that our results remain the same after applying a disformal plus a conformal transformation to our system. These transformations, at quadratic level in a perturbative expansion in tensor fluctuations, render the system identical to Einstein gravity minimally coupled with a scalar field [200, 201]. On the other hand, as we shall discuss, at *cubic* level in a perturbative expansion tensor interactions include terms as $\dot{h}_{ij}^3$ which cannot be associated with contributions of standard Einstein gravity.

- The squeezed limit of the tensor bispectrum during non-attractor evolution does not satisfy Maldacena's consistency relations [188], and can be parametrically amplified with respect to standard slow-roll scenarios. This is due to the fact that the would be decaying tensor mode is also excited in our system, and the corresponding dynamics is not a 'single tensor' adiabatic system where Maldacena's arguments apply. This is analogous to what happens for models discussing non-attractor inflation in the scalar sector.

- Squeezed tensor non-Gaussianity induces a characteristic quadrupolar anisotropy on the power spectrum of the stochastic background of primordial tensor perturbations. As a step to make contact with gravitational wave experiments, we discuss the response function of a ground based Michelson interferometer to a gravitational wave background with such a feature.

Conventions

We will use natural units, $\hbar = c = 1$, with reduced Planck mass $M_{\rm pl}^2 = (8\pi G)^{-1} = 1$. Our metric signature is mostly plus $(-,+,+,+)$. The background metric is a FRW universe with line element $ds^2 = -dt^2 + a^2(t)\, d\vec{x}^2 = a^2(\tau)\, (-d\tau^2 + d\vec{x}^2)$. Throughout the paper, we adopt the following Fourier convention

$$q_{ij}(\mathbf{x}, t) = \int \frac{\mathrm{d}^3 k}{(2\pi)^3}\; q_{ij}(\mathbf{k}, t)\; e^{-i\mathbf{k}.\mathbf{x}}. \tag{3.1.1}$$

3.2 Non-attractor dynamics and tensor fluctuations

We discuss a new method [123] for enhancing tensor fluctuations during inflation, which exploits the structure of tensor kinetic terms in inflationary theories with non-minimal derivative couplings between scalars and gravity.

This Section is mainly intended as an enlightening review of the methods and results developed in [123]. We fix the notation and set the stage for the calculations of tensor non-Gaussianity in Section 3.3.

3.2.1 A mechanism for enhancing tensor fluctuations at super-horizon scales

We focus on spin-2 tensor fluctuations around a FRW cosmological background, defined as [188]

$$ds^2 = -\mathrm{d}t^2 + a^2(t)\left(e^h\right)_{ij}\mathrm{d}x^i\mathrm{d}x^j\,, \tag{3.2.1}$$

with

$$\left(e^h\right)_{ij} = \delta_{ij} + h_{ij} + \frac{1}{2}h_{ik}h_{kj} + \frac{1}{6}h_{ik}h_{kl}h_{lj} + \dots \tag{3.2.2}$$

where h_{ij} is a transverse traceless spin-2 tensor perturbation. At leading order in a derivative expansion, the quadratic action for tensor perturbations can be expressed as (see e.g. [202]. From now on, unless otherwise stated, we set $M_{\rm pl} = 1$)

$$\begin{aligned} S_T &= \frac{1}{8}\int \mathrm{d}t\,\mathrm{d}^3x\,a^3(t)\left[\mathcal{G}_T(t)\,(\partial_t h_{ij})^2 - \frac{\mathcal{F}_T(t)}{a^2(t)}\left(\vec{\nabla}h_{ij}\right)^2\right], \\ &= \frac{1}{2}\int \mathrm{d}y\,\mathrm{d}^3x\,z_T^2(y)\left[(\partial_y h_{ij})^2 - \left(\vec{\nabla}h_{ij}\right)^2\right], \\ &\underset{(z_T\,h_{ij}\equiv v_{ij})}{=} \frac{1}{2}\int \mathrm{d}y\,\mathrm{d}^3x\left[\left(v'_{ij}\right)^2 - \left(\vec{\nabla}v_{ij}\right)^2 + \frac{z''_T}{z_T}\,v_{ij}^2\right]. \end{aligned} \tag{3.2.3}$$

The first line of this formula contains two functions of time $\mathcal{G}_T$, $\mathcal{F}_T$ that characterise the tensor kinetic terms [1]. Their structure depends on non-minimal couplings of gravity to the scalar field driving inflation, and on the homogeneous scalar profile (see Subsection 3.2.2 and [202]). In the second

[1] The quadratic action for tensor mode can be recasted into a canonical 'Einstein frame' action by applying a disformal and a conformal transformation to the system [200]. Nevertheless, all our results remain the same in any frame one uses, as anticipated in [123] and explained more at length in Section 3.3 and Appendix B.2 of the present paper.

line of eq (3.2.3) we redefine the time variable as

$$\mathrm{d}t = a\left(\frac{\mathcal{G}_T}{\mathcal{F}_T}\right)^{1/2}\mathrm{d}y\,, \tag{3.2.4}$$

$$= \frac{a(y)}{c_T(y)}\,\mathrm{d}y \tag{3.2.5}$$

in order to express the action for tensor fluctuations as the one for a free field in a time dependent background. We also introduce the convenient combination

$$z_T^2(y) = \frac{a^2(y)}{4}\sqrt{\mathcal{G}_T(y)\,\mathcal{F}_T(y)}\,, \tag{3.2.6}$$

dubbed as *tensor pump field* in analogy with the nomenclature used in the literature for the scalar sector.

Focusing on super-horizon evolution, defined in Fourier space as the condition $k^2 \ll |z_T''/z_T|$, the equations of motion for tensor fluctuations associated with action (3.2.3) admits the following solution

$$h_{ij}(y) = q_1 + q_2\int^y \frac{\mathrm{d}y'}{z_T^2(y')}\,, \tag{3.2.7}$$

with q_1 and q_2 two integration constants, which can be fixed by matching with the solution at sub-horizon scales. q_1 corresponds to the usual constant mode at super-horizon scales, while the coefficient of q_2 would be the decaying mode, if z_T were an increasing function of the time variable y. On the other hand, whenever z_T becomes a *decreasing* function of y, we enter in a non-attractor phase where tensor modes can grow on super-horizon scales:

$$\frac{z_T'}{z_T} < 0 \qquad \Longrightarrow \qquad \text{Tensor modes grow on super-horizon scales}\,. \tag{3.2.8}$$

This is a *non-attractor phase* for tensor fluctuations, since the would be decaying mode actually increases and controls the amplitude of tensor fluctuations at large scales. Such behaviour for the pump field z_T usually requires a departure from a slow-roll approximation, and the evolution and

properties of fluctuations cannot be described in terms of usual slow-roll formulae. On the other hand, as shown in [123], we can make use of *tensor duality* – which generalises to the tensor spectrum the scalar duality first pointed out in [187] (see also [203–210]) – to analytically investigate the dynamics of tensor modes in the non-attractor phase.

Tensor duality is defined as follows. In the third line of eq (3.2.3) we rescale tensor modes as $h_{ij} \equiv v_{ij}/z_T$ in order to rewrite the action as a free system in flat space with a time-dependent mass term for the mode v_{ij}. The mass parameter z_T''/z_T depends on time, and its value can change during the inflationary evolution. We consider two distinct phases of cosmological expansion, each lasting for a certain time interval, characterised respectively by two regimes for the parameters z_T and $\tilde{z}_T$ related by the *duality* condition

$$\frac{\tilde{z}_T''}{\tilde{z}_T} = \frac{z_T''}{z_T} \qquad \Longrightarrow \qquad \tilde{z}_T(y) = z_T(y)\left(c_1 + c_2 \int^y \frac{\mathrm{d}y'}{z_T^2(y')}\right) \tag{3.2.9}$$

for constant values of c_1, c_2 (not to be confused with the $q_{1,2}$ of eq (3.2.7)). Then the quantity v_{ij} is described by the very same action in the two phases (the third line of eq (3.2.3)) and the corresponding mode h_{ij} is described by the same statistics in the two epochs – only the time-dependent overall normalization changes. The most useful application of such tensor duality is perhaps the tensor dual of a slow-roll phase characterised by constant functions $\mathcal{G}_T$ and $\mathcal{F}_T$, leading to the slow-roll condition $z_T = \text{const} \times a(y)$. In the dual epoch, $|\tilde{z}_T| = \text{const}/a^2(y)$: we are in a non-attractor phase of evolution, since $\tilde{z}_T$ decreases with time. On the other hand, in both phases,

$$\frac{\tilde{z}_T''}{\tilde{z}_T} = \frac{z_T''}{z_T} = \frac{2}{y^2}\,. \tag{3.2.10}$$

The corresponding spectrum of tensor modes $\tilde{h}_{ij} = \tilde{z}_T\, v_{ij}$ is scale invariant (as in slow-roll), and its amplitude increases with time at super-horizon

scales during the non-attractor phase

$$\mathcal{P}_{\tilde{h}}(t) = \left(\frac{a(t)}{a_0}\right)^6 \mathcal{P}_h \tag{3.2.11}$$

with a_0 being the value of the scale factor at the onset of the non-attractor era, and $\mathcal{P}_h$ is the (nearly constant) value of the tensor spectrum at super-horizon scales in the initial slow-roll phase. See the technical Appendix B.1 and [123] for details on the computation of the tensor power spectrum during the non-attractor phase, leading to the aforementioned amplification.

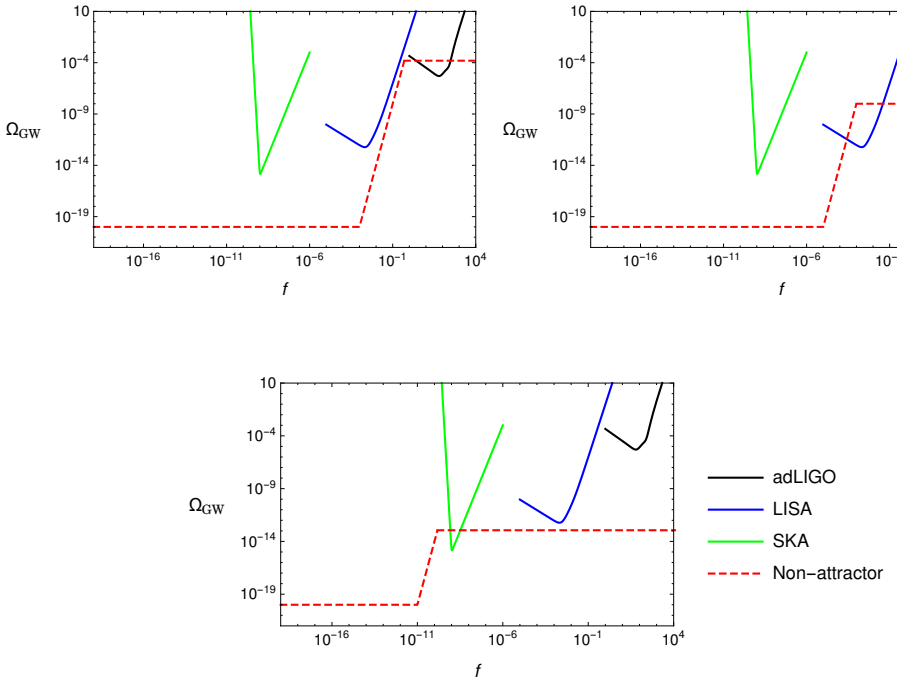

FIGURE 3.1: *This figure shows qualitatively how primordial tensor modes get amplified during a non-attractor phase. They can contribute to the GW energy density Ω_{GW}, and thus enter within the sensitivity curves for GW detectors in their appropriate frequency ranges (expressed in Hz). We model inflation as a pure de Sitter phase, during which a short period of non-attractor evolution occurs – whose starting time and duration depend on the model one considers – enhancing the tensor spectrum. We use formula (3.2.11), and assume for simplicity instantaneous transitions between attractor and non-attractor eras. Our conventions for the definition of the GW energy density Ω_{GW} are the same as in [211].*

Such amplification of tensor fluctuations during a (typically short) non-attractor phase can lead to a very steep increase of the tensor spectrum

as a function of frequency, once the amplitude of primordial tensor modes is transferred to the present cosmological epoch using standard formulae – see e.g. [211]. In Figure 3.1, we show how the spectrum of the superhorizon modes can be amplified to enter within the sensitivity curves for GW detectors, using formula (3.2.11), and assuming for simplicity instantaneous transitions between attractor and non-attractor eras. The figure is only indicative, because it does not take into account the transition phases during different epochs and, above all, does not take into consideration additional model-dependent constraints from amplification of scalar modes. In the next subsection we briefly review an example of a concrete realisation of a tensor dual to a slow-roll phase in single field inflation.

3.2.2 A concrete realisation in single field inflation

We now briefly review an explicit realisation of the mechanism of the previous subsection in a single field inflationary scenario, first presented in [123]. For convenience, we wish to find a single field inflationary model where the functions $\mathcal{F}_T$ and $\mathcal{G}_T$ introduced in the action (3.2.3) are directly proportional to the square of scalar field velocity $\dot{\phi}$ as

$$\mathcal{F}_T \;\propto\; \frac{\dot{\phi}^2}{H_0^2}\,, \qquad ; \qquad \mathcal{G}_T \propto \frac{\dot{\phi}^2}{H_0^2}\,, \tag{3.2.12}$$

during the entire phase of the inflationary evolution, which for simplicity we describe in terms of pure de Sitter evolution with constant Hubble parameter H_0. The scalar field follows a slow-roll evolution with constant velocity $\dot{\phi}$ = const for most of the inflationary phase, but there is a brief phase of non-attractor evolution (whose duration is tunable in terms of the available parameters) during which $\dot{\phi} \propto 1/a^3$:

$$\dot{\phi} \propto \begin{cases} \text{const} & \text{during slow-roll phase} \\ 1/a^3 & \text{during non-attractor phase} \end{cases}$$

See Fig 3.2 for a representation of the scalar field time dependent profile. Plugging these scalar profiles into the expressions for the functions $\mathcal{F}_T$, $\mathcal{G}_T$ of eq (3.2.12) and recalling the definition of the pump field z_T, eq (3.2.6), it is easy to show that during the non-attractor phase we can use the tensor duality of eq (3.2.9), and the tensor power spectrum is enhanced by a factor $a^6(t)$ in this era (3.2.11). Indeed, such a scenario is conceptually similar to the model of Starobinsky [166], designed to enhance scalar fluctuations during non-attractor inflation (see also [186] and references therein).

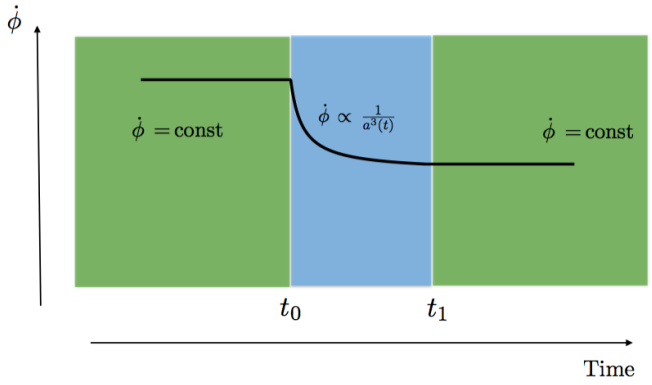

FIGURE 3.2: *Behaviour of the scalar field derivative in our system.*

The conditions described above can be realised if the scalar field has non-minimal couplings with gravity during inflation. We consider a scenario based on Horndeski theory of gravity, the most general scalar-tensor set-up with explicitly second order equations of motion, which is described by the Lagrangian

$$\mathcal{L}_{\rm tot} = \mathcal{L}_2 + \mathcal{L}_3 + \mathcal{L}_4 + \mathcal{L}_5 \,, \tag{3.2.13}$$

$$\mathcal{L}_2 = G_2 \,, \tag{3.2.14}$$

$$\mathcal{L}_3 = -G_3 \,\Box\,\phi \,, \tag{3.2.15}$$

$$\mathcal{L}_4 = G_4\, R + G_{4X}\left[(\Box\phi)^2 - (\nabla_\mu\nabla_\nu\phi)^2\right] , \tag{3.2.16}$$

$$\begin{aligned}\mathcal{L}_5 &= G_5\, G_{\mu\nu}\,\nabla^\mu\nabla^\nu\,\phi \\ &- \frac{G_{5X}}{6}\left[(\Box\phi)^3 - 3\,\Box\,\phi\,(\nabla_\mu\nabla_\nu\phi)^2 + 2\,(\nabla_\mu\nabla_\nu\phi)^3\right] .\end{aligned} \tag{3.2.17}$$

The quantities $G_a = G_a(\phi, X)$ $(a = 1, \dots 5)$ are in principle arbitrary functions of the scalar field ϕ and

$$X = -\frac{1}{2}\,\partial_\mu\phi\partial^\mu\phi\,, \tag{3.2.18}$$

R is the Ricci tensor, $G_{\mu\nu}$ is the Einstein tensor, and $G_{a\,X} = \partial G_a/\partial X$. For simplicity, in this work we focus on scenarios where a shift symmetry $\phi \to \phi + c$ is imposed, and the G_i only depend on the kinetic function X. Inflation in scenarios based on Horndeski and Galileon Lagrangians have a long history, starting from [212] and the more general G-inflation [202, 213] models. Scenarios of ultra slow-roll, non-attractor G-inflation have been discussed in [214]. The quadratic Lagrangian for tensor fluctuations is described by our initial action (3.2.3) with

$$\mathcal{F}_T = 2\left[G_4 - X\,\ddot{\phi}\,G_{5X}\right] \tag{3.2.19}$$

$$\mathcal{G}_T = 2\left[G_4 - 2\,X\,G_{4X} - X\,H_0\,\dot{\phi}\,G_{5X}\right]. \tag{3.2.20}$$

In [123] we showed that the conditions (3.2.12) can be realised by choosing the following structure for the functions $G_a(X)$

$$G_2 = \rho X + \frac{\sqrt{2}\,H_0^2\,\alpha}{3}\sqrt{X} - \nu\,, \qquad G_3 = \frac{\sqrt{2}\,\delta}{3\,H_0}\sqrt{X}\,,$$
$$G_4 = -\frac{\beta}{6H_0^2}\,X\,, \qquad G_5 = \frac{\sigma}{\sqrt{2}\,H_0^3}\sqrt{X}\,, \tag{3.2.21}$$

where the Greek letters are constant coefficients – which can be different during the three different phases of evolution summarised in Figure 3.2 – and H_0 is the constant Hubble parameter during inflation. We refer the reader to [123] for a detailed analysis of the system, with a quantitative discussion on the conditions necessary to avoid instability and to enhance the tensor power spectrum at superhorizon scales during the non-attractor phase. Notice that besides the tensor modes, scalar modes are also typically enhanced in these scenarios, although with a smaller amplitude [123].

3.3 Tensor non-Gaussianity in non-attractor inflation

The mechanism we analysed in the previous Section shows that it is possible to enhance the tensor power spectrum at small (interferometer) scales by exploiting the behaviour of the would-be decaying mode, which can grow in a regime of non-attractor inflation. An interesting feature of our mechanism is that there exists a *tensor duality* which allows us to obtain analytical expressions for the tensor power spectrum even in regimes that are far from a slow-roll period. In this Section, we study the tensor bispectrum, providing *analytical expressions* for this quantity during the non-attractor phase, and showing that the amplitude, shape and scale dependence of the tensor bispectrum can be different with respect to standard slow-roll inflation.

The tensor bispectrum is an interesting theoretical quantity which allows to discriminate between primordial and astrophysical sources of stochastic gravitational wave backgrounds (SGWB) [199]: if large tensor non-Gaussianity is detected, then it is likely that the SGWB has primordial origin, since an astrophysical GW background – formed by contributions from many unresolved sources – is likely to be Gaussian from the central limit theorem. The properties of the tensor bispectrum – shape, scale dependence, its value in the squeezed limit – are important for characterising the field content during inflation, and to further distinguish among different primordial sources that can amplify the tensor spectrum at interferometer scales [199].

Remarkably, the cubic action for tensor fluctuations around FRW in single field inflationary theories with second order equations of motion – the starting point for the computation of the bispectrum – has a simple structure, and contains only two contributions [215, 216]

$$
\begin{aligned}
S_T^{(3)} &= \int \mathrm{d}t\, \mathrm{d}^3x\, a^3 \left[\frac{\mathcal{F}_T}{4a^2} \left(h_{ik} h_{jl} - \frac{1}{2} h_{ij} h_{kl} \right) \partial_k \partial_l h_{ij} + \frac{\dot{\phi} X G_{5X}}{12} \dot{h}_{ij} \dot{h}_{jk} \dot{h}_{ki} \right], \\
&= S^{(3)}_{T(\mathrm{GR})} + S^{(3)}_{T(\mathrm{new})} \,. \qquad (3.3.1)
\end{aligned}
$$

This action is obtained expanding the Horndeski Lagrangian density (3.2.13) up to cubic order in fluctuations, and the functions $\mathcal{F}_T$ and G_5 are given respectively in (3.2.19) and (3.2.17). The result of standard single field inflation with canonical kinetic terms is obtained setting $\mathcal{F}_T = 1$ (recall that we choose units such that $M_{\mathrm{pl}}^2 = 1$). The structure of the first contribution, containing spatial derivatives only, is the same as the one obtained expanding the Ricci scalar at cubic order around a FRW background: this is the reason we denote it as $S^{(3)}_{T(\mathrm{GR})}$. The second contribution, $S^{(3)}_{T(\mathrm{new})}$, is instead specific to the Horndeski action: notice that it contains three time derivatives $\dot{h}_{ij}^3$, a feature to which we will return later. Tensor non-Gaussianity associated with the action (3.3.1) was studied in detail in a slow-roll regime in [215, 216], where it was found that the 'GR' term gives a bispectrum enhanced in the squeezed limit, while the 'new' contribution gives a bispectrum peaked in equilateral configurations. In this work, instead, we will work out the tensor non-Gaussianity during a transient non-attractor phase, finding quite different results.

3.3.1 Amplitude of tensor non-Gaussianity

We discuss the amplitude and some properties of tensor non-Gaussianity during an era of non-attractor inflation, which is dual to a slow-roll phase as explained in Section 3.2. For simplicity, we focus on the case where the background geometry is exactly described by a de Sitter universe, with constant Hubble parameter H_0 (in [123] we proved that the equations of motion admit this solution for the scale factor). We relegate all the technical details to Appendix B.1, and we discuss here the physical consequences of

our computation of the tensor three point function in Fourier space during a non-attractor era. In order to express our results more concisely, we define two polarisation modes as (here, $e_{ij}^{(s)}$ is the polarization tensor with the helicity states $s = \pm$, satisfying $e_{ii}^{(s)}(\mathbf{k}) = 0 = k_j e_{ij}^{(s)}(\mathbf{k})$. See Appendix B.1 for more information regarding our conventions on the polarisation tensors)

$$\xi^{(s)}(\mathbf{k}) \equiv h_{ij}(\mathbf{k}) e_{ij}^{*(s)}(\mathbf{k}), \tag{3.3.2}$$

which allow us to express the three point function in the non-attractor era as

$$\begin{aligned}\langle \xi^{(s_1)}(\mathbf{k}_1)\xi^{(s_2)}(\mathbf{k}_2)\xi^{(s_3)}(\mathbf{k}_3)\rangle &= (2\pi)^7 \delta(\mathbf{k}_1+\mathbf{k}_2+\mathbf{k}_3) \\ &\quad \times \frac{\mathcal{P}_h^{(\mathrm{end})^2}}{\Pi_i\ k_i^3}\left(\mathcal{A}^{s_1s_2s_3}_{(\mathrm{new})} + \mathcal{A}^{s_1s_2s_3}_{(\mathrm{GR})}\right), \\ &\equiv (2\pi)^7\, \delta(\mathbf{k}_1+\mathbf{k}_2+\mathbf{k}_3)\, B^{s_1s_2s_3}(\mathbf{k}_i)\,. \end{aligned} \tag{3.3.3}$$

Hence we define the tensor bispectrum $B^{s_1s_2s_3}(\mathbf{k}_i)$ as the coefficient of the δ-function in the previous expression, which depends on the momenta as well as on the polarisation indices.

Using (B.1.18), (B.1.27), the amplitudes

$$\mathcal{A}^{s_1s_2s_3}_{(\mathrm{new}),(\mathrm{GR})} \equiv e_{i_1j_1}^{*(s_1)}(\mathbf{k}_1) e_{i_2j_2}^{*(s_2)}(\mathbf{k}_2) e_{i_3j_3}^{*(s_3)}(\mathbf{k}_3) \mathcal{A}^{(\mathrm{new}),(\mathrm{GR})}_{i_1j_ii_2j_2i_3j_3}$$

can be calculated following the same methods of [216]. For our scenario, in the non-attractor regime, we find

$$\begin{aligned}\mathcal{A}^{s_1s_2s_3}_{(\mathrm{new})} &= \mathcal{A}^{(\mathrm{new})}(k_1,k_2,k_3) F(s_1k_1, s_2k_2, s_3k_3) \\ \mathcal{A}^{s_1s_2s_3}_{(\mathrm{GR})} &= \mathcal{A}^{(\mathrm{GR})}(k_1,k_2,k_3) \frac{(s_1k_1+s_2k_2+s_3k_3)^2}{2} F(s_1k_1, s_2k_2, s_3k_3), \end{aligned} \tag{3.3.4}$$

where

$$F(x,y,z) = \frac{1}{64}\frac{1}{x^2y^2z^2}(x+y+z)^3(x-y+z)(x+y-z)(x-y-z). \tag{3.3.5}$$

$\mathcal{A}^{(\mathrm{GR})}$ and $\mathcal{A}^{(\mathrm{new})}$ are obtained in equations (B.1.26) and (B.1.31) respectively, which we rewrite here:

$$\mathcal{A}^{(\mathrm{GR})} = -\frac{K}{64}\Bigg[\left(1-\frac{3}{K^3}\sum_{i\neq j}k_i^2k_j-\frac{6}{K^3}\Pi_i k_i\right)(-Ky_{\mathrm{end}})^2 \\ -\frac{\pi}{4}\left(1-\frac{4}{K^3}\sum_{i\neq j}k_i^2k_j-\frac{4}{K^3}\Pi_i k_i\right)(-Ky_{\mathrm{end}})^3+\dots\Bigg], \quad (3.3.6)$$

$$\mathcal{A}^{(\mathrm{new})} = -\frac{3H\mu^{(\mathrm{end})}}{16\mathcal{G}_T^{(\mathrm{end})}}\Bigg\{\left(K^3-3\sum_{i\neq j}k_i^2k_j-6\ \Pi_i k_i\right) \\ -\frac{1}{4}\left(K^3-5\sum_{i\neq j}k_i^2k_j+\frac{2}{K^2}\sum_{i\neq j}k_i^3k_j^2\right)(-Ky_{\mathrm{end}})^2\Bigg\}. \quad (3.3.7)$$

In these formulae, $K = k_1+k_2+k_3$,

$$\mu^{(\mathrm{end})} \equiv \dot{\phi}^{(\mathrm{end})}X^{(\mathrm{end})}G_{5X}^{(\mathrm{end})}$$

and the 'end' indicates the end of the non-attractor phase: our results then quantify the non-Gaussianity accumulated by the tensor modes during the non-attractor era. Before proceeding, some observations are in order:

- The squeezed limit of the bispectrum does not satisfy Maldacena's consistency relations [188]. Indeed, computing the bispectrum of eq (3.3.3) for $s_1 = s_2$ in the limit of squeezed isosceles triangles, we find

$$B^{s_1s_1s_3}(\mathbf{k}_1,-\mathbf{k}_1,\mathbf{k}_3\to 0) = \frac{\left(\mathcal{P}_h^{(\mathrm{end})}\right)^2}{32\,k_1^3\,k_3^3} \\ \times\left[\frac{3\,H\mu^{(\mathrm{end})}}{\mathcal{G}_T^{(\mathrm{end})}}\left(1+\frac{(-k_1y_{\mathrm{end}})^2}{2}\right)+\frac{(-k_1y_{\mathrm{end}})^2}{2}\right], \quad (3.3.8)$$

while we find zero for $s_1 \neq s_2$. Instead, Maldacena's consistency relation (with our conventions) would read in this case

$$B^{s_1 s_1 s_3}(\mathbf{k}_1, -\mathbf{k}_1, \mathbf{k}_3 \to 0) = \frac{3}{64\, k_1^3\, k_3^3} \left(\mathcal{P}_h^{(\mathrm{end})}\right)^2 .$$

This can be expected, since during the non-attractor era, besides the usual growing tensor mode, the would be tensor decaying mode is excited as well, and we are no longer working in a 'single tensor' adiabatic system where Maldacena's arguments apply [2]. By tuning the parameters of the model, this implies that the amplitude of the tensor bispectrum can be enhanced in the squeezed limit (see also [154, 155, 221–223] for different scenarios with enhanced squeezed tensor bispectrum), with potentially interesting phenomenological consequences that we shall discuss in Section 3.3.3.

- While the scenario studied so far is characterised by non-standard kinetic terms for the tensor sector, it is known that by performing a conformal followed by a disformal transformation the *second order action* for tensor modes – our eq. (3.2.3) – acquires the very same structure of the second order action of Einstein gravity around FRW homogeneous backgrounds [200]. On the other hand, the *third order action* we are considering here, eq (3.3.1), contains a piece with three time derivatives $\dot{h}_{ij}^3$ – an operator that cannot be recast into a pure 'GR' contribution via disformal/conformal transformations. This said, in Appendix B.2 we show in detail that all our results remain the same also in an 'Einstein frame' with standard second order tensor action: the only difference is that in this frame the non-attractor phase corresponds to a short period of universe contraction.

- Our expressions for the tensor bispectrum contain a characteristic scale dependence with overall factors containing powers of $(-K\, y_{\mathrm{end}})$,

[2] Similar considerations have been developed in various works for the scalar sector, see e.g. [170, 217–220], finding non-attractor models with an enhanced scalar bispectrum in the squeezed limit.

that are distinctive of our scenario – being absent in other frameworks with large tensor non-Gaussianity. The explicit dependence on the time y_{end} when the non-attractor phase ends is due to the fact that the bispectrum has been computed specifically at the end of the non-attractor phase. For simplicity, we assume that this era is immediately followed by a standard slow-roll inflation, where tensor modes and their statistics are frozen in a super-horizon regime. The overall scale dependence of the tensor bispectrum controlled by K is also distinctive of our set-up. Similar situations have been encountered in the scalar sector, starting from the work [209], for models with non-standard cosmological expansion history, leading to interesting observables associated with scale-dependent non-Gaussianity (explored in general terms in [224–226]). A consequence of this fact is that non-Gaussianity depends on the scale and might be different at different interferometer scales (for example, LIGO-VIRGO and LISA): it would be interesting to further explore phenomenological consequences of this property, which goes beyond the scope of our work.

We now continue by estimating the amplitude of non-Gaussian signal. As a measure for the amount of non-Gaussianity, we use the following definition of the non-linearity parameter $f_{\rm NL}$, as in the works [215, 216]

$$\hat{f}^{s_1s_2s_3}_{\rm NL(new),(GR)} \equiv 30\frac{\mathcal{A}^{s_1s_2s_3}_{\rm (new),(GR)}}{K^3}\bigg|_{k_1=k_2=k_3}, \tag{3.3.9}$$

which is analogous to the standard $f_{\rm NL}$ for the scalar curvature perturbation. Notice that the $f_{\rm NL}$ above is defined in terms of equilateral configurations for tensor bispectra, and its value depends on the polarisations. Using the definitions of the two amplitudes in (3.3.4), we find

$$\hat{f}^{s_1s_2s_3}_{\rm NL(new)} = -\frac{45}{32}\left[3+2(s_1s_2+s_1s_3+s_2s_3)\right]\frac{\mathcal{A}^{\rm (new)}(K/3,K/3,K/3)}{K^3}, \tag{3.3.10}$$

$$\hat{f}^{s_1s_2s_3}_{\rm NL(GR)} = -\frac{5}{64}\big[21 + 20(s_1s_2 + s_1s_3 + s_2s_3)\big]\frac{\mathcal{A}^{(\rm GR)}(K/3, K/3, K/3)}{K}. \tag{3.3.11}$$

The dependence of the non-linerity parameter on the polarization implies the following symmetry $\hat{f}^{++-}_{\rm NL(new),(GR)} = \hat{f}^{+--}_{\rm NL(new),(GR)}$ and $\hat{f}^{+++}_{\rm NL(new),(GR)} = \hat{f}^{---}_{\rm NL(new),(GR)}$ which follows from the fact that the interactions we consider do not violate parity. More concretely, we have

$$\hat{f}^{+++}_{\rm NL(new)} = \frac{135}{512}\frac{H\mu^{(\rm end)}}{\mathcal{G}_T^{(\rm end)}}\left(1 + \frac{5}{36}(-Ky_{\rm end})^2\right) \tag{3.3.12}$$

and

$$\hat{f}^{++-}_{\rm NL(new)} = \frac{15}{512}\frac{H\mu^{(\rm end)}}{\mathcal{G}_T^{(\rm end)}}\left(1 + \frac{5}{36}(-Ky_{\rm end})^2\right). \tag{3.3.13}$$

Similarly for $f^{s_1s_2s_3}_{\rm NL(GR)}$ we have

$$\hat{f}^{+++}_{\rm NL(GR)} = \frac{45}{4096}\,(-Ky_{\rm end})^2\left[1 + \frac{\pi}{12}(-Ky_{\rm end})\right] \tag{3.3.14}$$

and

$$\hat{f}^{++-}_{\rm NL(GR)} = \frac{5}{36864}\,(-Ky_{\rm end})^2\left[1 + \frac{\pi}{12}(-Ky_{\rm end})\right]. \tag{3.3.15}$$

These results show that the $f_{\rm NL}$ parameter is generically positive during the non-attractor phase, similar to the case of contracting universes considered in [209]. Importantly, due to the strong scale dependence of the $f_{\rm NL(GR)}$, $f_{\rm NL(new)}$ dominates the bispectrum for $-k_iy_{\rm end} \ll 1$ and $H\mu^{(\rm end)}/\mathcal{G}_T^{(\rm end)} \sim \mathcal{O}(1)$. Recall that $\mathcal{G}_T \supset \mu H$, in particular

$$\mathcal{G}_T = 2\left(G_4 - 2XG_{4X} - \mu H\right) \tag{3.3.16}$$

for the background model we discussed earlier. The expression above (3.3.16) indicates that we need accidental cancellations[3] between the first two terms in $\mathcal{G}_T > 0$ and μH in order to ensure $H\mu/\mathcal{G}_T \gg 1$. We discuss in

[3]Note that this situation is not special to the model under consideration in this work and arises for general slow-roll scenarios as well [215].

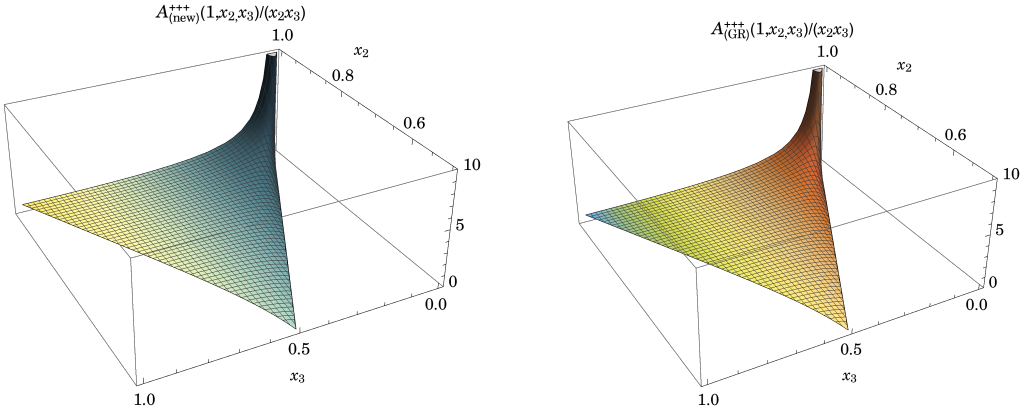

FIGURE 3.3: $\mathcal{A}^{+++}_{(\text{new})}(1,x_2,x_3)/(x_2x_3)$ *as a function of* x_2 *and* x_3 *where we set* $H\mu^{\text{end}}/\mathcal{G}^{\text{end}}_T \to 1$ *(Left).* $\mathcal{A}^{+++}_{(\text{GR})}(1,x_2,x_3)/(x_2x_3)$ *as a function of* x_2 *and* x_3 *(Right). In both plots we normalized the amplitudes* $\mathcal{A}^{+++}_{(\text{new})}$ *and* $\mathcal{A}^{+++}_{(\text{GR})}$ *to unity for equilateral configurations* $x_2 = x_3 = 1$ *and took* $-Ky_{\text{end}} = 10^{-2}$.

Appendix B.3 a concrete scenario leading to large tensor non-Gaussianity within the framework we reviewed in Section 3.2.2.

3.3.2 Shape of tensor non-Gaussianity

We now study the shape of non-Gaussianity in our model. Since both of the amplitudes have non-trivial scale dependence, we examine the shape of the amplitudes [4] at fixed $-Ky_{\text{end}}$. We focus on the dimensionless ratio $\mathcal{A}^{s_1s_2s_3}_{(\text{new}),(\text{GR})}/(k_1k_2k_3)$ of both amplitudes in (3.3.4) following the literature for scalar perturbations [227]. In particular, we will plot $\mathcal{A}^{s_1s_2s_3}_{(\text{new}),(\text{GR})}/(k_1k_2k_3)$ in the $x_2 - x_3$ plane where $x_j \equiv k_j/k_1$ with $j \neq 1$ by restricting ourselves to the range $1 - x_2 \leq x_3 \leq x_2$. Note that the first inequality follows from the triangle inequality whereas the latter allows us to avoid plotting the same configuration twice. The non-Gaussian amplitudes $\mathcal{A}^{+++}_{(\text{new})}/(k_1k_2k_3)$ and $\mathcal{A}^{+++}_{(\text{GR})}/(k_1k_2k_3)$ are shown in Figure 3.3. We see that both the interaction terms in (3.3.1) give rise to non-Gaussianity that peaks in the squeezed limit. This result is in contrast with the slow-roll case where the

[4] Recall that we are interested in modes that leave the sound-horizon during the non-attractor era, *i.e.* $-k_iy_0 > 1$ and $-k_iy_{\text{end}} < 1$. This implies that the modes of interest satisfy $1 > -Ky_{\text{end}} > e^{-\Delta N}$, where ΔN is the duration of the non-attractor era.

new contribution peaks in the equilateral configuration. This difference is due to the fact that during the non-attractor phase, the fluctuations in h_{ij} keeps growing outside the horizon due to the dynamics of the would be decaying mode, *i.e.* $\dot{h}_{ij} = 3Hh_{ij}$ and therefore the non-Gaussian amplitude peaks when one of the wave numbers is small, corresponding to the squeezed-triangle limit[5]. In the standard attractor slow-roll background however, tensor fluctuations freeze on large scales, $\dot{h}_{ij} \to 0$ and therefore only wave-numbers comparable to the size of the horizon can contribute to the non-Gaussianity for the interaction proportional to the time derivatives of h_{ij} in (3.3.1).

3.3.3 Interferometer response function for anisotropic tensor power spectrum

As we explained in Subsection 3.3.1, our system does not satisfy Maldacena consistency relations: the squeezed limit of the bispectrum can be enhanced by the contributions of the would be decaying tensor mode. This means that we can develop a scenario where at the same time we have a large tensor power spectrum at interferometer scales, accompanied by enhanced squeezed tensor non-Gaussianity. In this subsection, we start with a brief 'theory' part to connect the squeezed limit of the tensor bispectrum with a quadrupolar anisotropy of the tensor power spectrum; we then continue with a discussion on possible ways to detect an anisotropic gravitational wave power spectrum with ground based interferometers, building on the results of [228].

Theory: A large non-Gaussianity in the squeezed limit can induce couplings between modes at different scales: the tensor power spectrum is modulated by long tensor modes that induce large scale anisotropies. This fact has been explored in several contexts, mainly in the scalar, but also in

[5]See [209] for similar dynamics that lead an to enhanced squeezed bispectrum in curvature perturbations.

the tensor sector: see e.g. [229–232]. Other scenarios that can induce large tensor non-Gaussianity in the squeezed limit, by violating the adiabaticity condition in the tensor sector, are supersolid inflation [152–155, 159, 160], bigravity or higher spin theories [162–164, 221–223]; our considerations can apply to these cases as well.

When focussing on the 'GR' operator of action, one finds that squeezed non-Gaussianity induces a quadrupolar anisotropy in the tensor power spectrum, with[6] (see e.g. [163, 233])

$$\mathcal{P}_h(\mathbf{k}, \mathbf{x}) = \mathcal{P}_h^{(0)}(k) \left[1 + \mathcal{Q}_{ij}(\mathbf{k}, \mathbf{x})\, \hat{k}_i \hat{k}_j\right] \tag{3.3.17}$$

and

$$\mathcal{Q}_{ij}(\mathbf{k}, \mathbf{x}) = \sum_{s_1, s_2} \int_{L^{-1}} \frac{d^3q}{(2\pi)^3}\, e^{i\,\mathbf{q}\mathbf{x}} \left(\frac{B^{s_1 s_1 s_2}(\mathbf{q}, \mathbf{k}, -\mathbf{q}-\mathbf{k})}{P_h(q) P_h(k)}\right) h_{\mathbf{q}} e_{ij}^{(s_2)}(\mathbf{q})\,. \tag{3.3.18}$$

We expect that the modulation (3.3.17) of the tensor power spectrum arises in any scenario with enhanced squeezed tensor non-Gaussianity. The integral defining the anisotropy parameter is evaluated in a patch centered at the position $\mathbf{x}$ and spans over long tensor modes with momenta within the non-attractor phase, corresponding to scales well larger than the gravitational wave wavelengths under consideration (see e.g. Section 4.4 of [163]). Being dependent on a linear combination of the polarization tensors $e_{ij}^{(s)}$, the quantity Q_{ij} is traceless. It is convenient to define the squeezed limit of the bispectrum as

$$\lim_{\mathbf{q}\to 0} \frac{B^{s_1 s_1 s_2}(\mathbf{k}, -\mathbf{k}, \mathbf{q})}{P_h(q) P_h(k)} = \frac{3}{64} + \hat{f}_{\rm NL}^{\rm sqz}\,, \tag{3.3.19}$$

where the quantity $\hat{f}_{\rm NL}^{\rm sqz}$ parameterises the deviation from the Maldacena's consistency conditions. In our case, the quantity $\hat{f}_{\rm NL}^{\rm sqz}$ can be read from eq (3.3.8). The anisotropy parameter $\mathcal{Q}_{ij}$ is determined in a statistical sense, averaging over many large patches. Its average equal to zero, and its

[6] Here $P_h(\mathbf{k}) \equiv \frac{2\pi^2 \mathcal{P}_h(\mathbf{k})}{\mathbf{k}^3}$ and $h_{\mathbf{q}} = v_{\mathbf{q}} a$ (see Appendix B.1).

variance results (see e.g. [163, 233])

$$\langle \mathcal{Q}_{ij}(\mathbf{k})\, \mathcal{Q}_{mn}(\mathbf{k})\rangle = \frac{\pi}{20} \left(\delta_{im}\delta_{jn} + \delta_{in}\delta_{jm} - \frac{2}{3}\delta_{ij}\delta_{mn}\right) \int \frac{dk}{k} \left|\hat{f}_{\rm NL}^{\rm sqz}\right|^2 \mathcal{P}_h^2\,, \tag{3.3.20}$$

$$\simeq \left(\delta_{im}\delta_{jn} + \delta_{in}\delta_{jm} - \frac{2}{3}\delta_{ij}\delta_{mn}\right) \left|\hat{f}_{\rm NL}^{\rm sqz}\right|^2 \mathcal{P}_h^2\, \Delta N \tag{3.3.21}$$

where in the last line we specialised for simplicity to the case of scale invariant power-spectrum and squeezed $f_{\rm NL}^{\rm sqz}$, and ΔN indicates the number of e-folds of cosmological evolution associated with the non-attractor era. The value of $\mathcal{P}_h$ in the previous formula indicates the magnitude of the tensor power spectrum at the end of non-attractor, which can be much larger than its value during the initial phase of slow-roll. Assuming that the magnitude of tensor spectrum is of order $\sim 10^{-14}$ at large scales, and it receives a 10^{10} enhancement during three e-folds of non-attractor inflation (using eq (3.2.11)), we learn that $f_{\rm NL}^{\rm sqz} \sim 100$ is sufficient to give a value for $\sqrt{\langle \mathcal{Q}_{ij}^2\rangle}$ of the order of a few percent (but $\sqrt{\langle \mathcal{Q}_{ij}^2\rangle}$ can be larger depending on the magnitude of tensor non-Gaussianity).

These results imply that the size of the anisotropy parameter can be a probe of the squeezed tensor bispectrum. We now outline a possible way to test such quantity with ground based interferometers [7].

Connection with gravitational wave experiments: The possibility of detecting anisotropies in a SGWB has started with the work [228], that derived the formalism necessary to quantitatively address the subject. The motivation for such investigations is to detect signals from a stochastic background due to astrophysical sources that can generate multipolar anisotropies. On the other hand, the formalism of [228] is sufficiently general and can be used with little changes also to investigate tensor anisotropies from the early universe. We apply the formulae and

[7] Tensor non-Gaussianity can also be an important observable for characterizing the primordial stochastic gravitational wave background at CMB scales, and have been explored in other contexts, see e.g. [147, 150, 234].

arguments of [228] to analyse tensor power spectra with a quadrupolar anisotropic structure as in eq (3.3.17). We focus for simplicity on analysing the response function for a single Michelson ground-based interferometer (see [235, 236] for reviews).

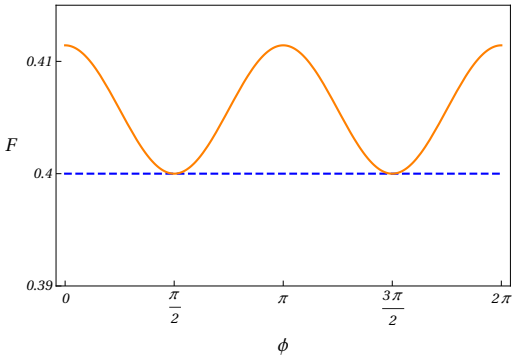

FIGURE 3.4: *Modulation of the response function F of eq (3.3.25) as the interferometer rotates an angle ϕ around an axis aligned with one of the interferometer arms. We assume that this arm points along the earth's rotation axis, and we choose a reference frame so that it corresponds to the direction $\hat{x}$. The dashed blue line shows the case with no anisotropy, $Q_{ij} = 0$, whereas the orange line shows the case with one component $Q_{33} = -Q_{11} = 0.1$ turned on.*

The total signal detected by an interferometer can decomposed as $S(t) = s(t) + n(t)$, with $n(t)$ the noise and $s(t)$ the contribution due to the gravitational wave. The relation between $s(t)$ and the mode h_{ij} can be written as [235]

$$s(t) = D^{ij} h_{ij}(t) , \tag{3.3.22}$$

with D_{ij} the detector tensor. For ground-based interferometers with arm directions $\hat{u}$ and $\hat{v}$ it reads

$$D^{ij} = \frac{1}{2} \left(\hat{u}^i \hat{u}^j - \hat{v}^i \hat{v}^j \right) . \tag{3.3.23}$$

We introduce the detector pattern function

$$F^{\lambda}(\mathbf{k}) = D^{ij} e_{ij}^{(\lambda)}(\mathbf{k}) . \tag{3.3.24}$$

The single detector response function, as defined for example in Section 3 of [235] is the proportionality constant F between the equal time 2pt function of the ground-based interferometer signal and the integral over frequencies of the amplitude of the primordial power spectrum $\mathcal{P}^{(0)}$. Using the techniques developed in [228], we find that the response function reads in our case

$$F = \frac{2}{5} - \frac{16}{35}\,\mathcal{Q}_{ij} D_{ik} D_{kj}\,. \tag{3.3.25}$$

The first contribution $2/5$ is the well known response function for an isotropic SGWB for a single, ground-based Michelson interferometer (see [235], Section 3). The additional contribution is instead new, and contains the anisotropic contributions of (3.3.17) to the interferometer response function: notice that it depends on the detector tensor D_{ij}.

As pointed out in [228], a response function as eq (3.3.25) can lead to a diurnal modulation of a ground-based interferometer signal, since the interferometer arms change orientation with respect to the anisotropy parameter $\mathcal{Q}_{ij}$ as the earth rotates around its axis. As a representative example, we plot in Fig 3.4 the modulation of the interferometer response function as the interferometer arms make a full rotation around the axis of rotation of the earth, when some of the components of the anisotropy parameter $\mathcal{Q}_{ij}$ is turned on. From the figure we learn that if we can probe percent variations of the interformeter response function – corresponding to diurnal modulations of the same order in the stochastic background – then we can probe anisotropies of the same magnitude: they correspond to values of $f_{\rm NL}^{\rm sqz}$ of the order of one hundred, which can be achieved in the model we are considering (see Appendix B.3).

It would be very interesting to study quantitatively whether current and future ground-based interferometers can set constraints on the size of Q_{ij} for realistic values of $\hat{f}_{\rm NL}^{\rm sqz}$, by studying correlations among signals from different instruments in the presence of the primordial quadrupolar asymmetry, and

by computing the corresponding signal-to-noise ratio. We plan to further develop these topics in a future publication.

3.4 Conclusions

We investigated the consequences of a non-attractor phase of cosmological evolution for the dynamics of primordial tensor modes, focussing on the properties of primordial tensor non-Gaussianity in scenarios with non-minimal couplings of gravity to the scalar sector. Thanks to a tensor duality, we have been able to analytically compute the properties of the tensor bispectrum during this phase. We have shown that the tensor bispectrum is enhanced in the squeezed limit with respect to standard slow-roll scenarios, and can parametrically violate Maldacena's consistency relations. Moreover, tensor non-Gaussianity exhibits a scale dependence characteristic of our set-up, that can help to distinguish our model from other scenarios with large tensor non-Gaussianity. Squeezed tensor non-Gaussianity induces a characteristic quadrupolar anisotropy on the power spectrum of the stochastic background of primordial tensor perturbations. To make contact with gravitational wave experiments, we discussed the response function of a ground based Michelson interferometer to a gravitational wave background with such a feature.

Much work is left for the future. It would be interesting to apply our approach to more general scenarios then the ones considered so far, including theories of Beyond Horndeski or DHOST [237–241]. This would also allow one to study in more general terms the transition phase between attractor and non-attractor, and related possible instabilities associated with violations of energy conditions (see the discussion in the Appendix of [123]). At the phenomenological level, it would be important to further investigate to what extent gravitational wave experiments can probe the quadrupolar anisotropy in the tensor power spectrum induced by squeezed

non-Gaussianity, by computing the corresponding signal-to-noise ratio for actual experiments, and relating it to the size of non-Gaussian observables. We plan to return on these topics soon.

Chapter 4

Probing a stationary non-Gaussian background of stochastic gravitational waves with pulsar timing arrays

This chapter consists of this paper [2] which was published in the jounral JCAP.

We introduce the concept of stationary graviton non-Gaussianity (nG), an observable that can be probed in terms of 3-point correlation functions of a stochastic gravitational wave (GW) background. When evaluated in momentum space, stationary nG corresponds to folded bispectra of graviton nG. We determine 3-point overlap functions for testing stationary nG with pulsar timing array GW experiments, and we obtain the corresponding optimal signal-to-noise ratio. For the first time, we consider 3-point overlap functions including scalar graviton polarizations (which can be motivated in theories of modified gravity); moreover, we also calculate 3-point overlap functions for correlating pulsar timing array with ground based GW detectors. The value of the optimal signal-to-noise ratio depends on the number

and position of monitored pulsars. We build geometrical quantities characterizing how such ratio depends on the pulsar system under consideration, and we evaluate these geometrical parameters using data from the IPTA collaboration. We quantitatively show how monitoring a large number of pulsars can increase the signal-to-noise ratio associated with measurements of stationary graviton nG.

4.1 Introduction

After the direct detection of GWs from merging black hole and neutron star binaries, one of the next challenges for GW experiments is the measurement of a stochastic gravitational wave background (SGWB). A theoretical characterization of the properties of the SGWB is essential for designing observables aimed to distinguish among different sources. Reviews of astrophysical and cosmological sources for a SGWB measurable with GW experiments can be found e.g. in [165, 242–245]. If a SGWB will be eventually detected, a natural question is whether it is possible to disentangle its different contributions from astrophysical and/or cosmological sources.

If a SGWB has cosmological origin, its spectrum can be characterized by specific properties: the frequency dependence of its energy density profile can be more complex than the typical power-law that characterise astrophysical backgrounds. (See e.g. the recent [246] for an accurate tool for distinguishing among different frequency profiles with LISA experiment.) Depending on the production mechanisms, it can be characterized by a large, intrinsic graviton (also called tensor) non-Gaussianity (nG) (see e.g. [199] for an analysis and review of tensor nG from cosmological inflation [1]). Although GWs produced by early universe mechanisms can be non-Gaussian,

[1] Also astrophysical backgrounds can be non-Gaussian, when sources of GWs are at the verge of being individually detected: the kind of nG is different from the one discussed here, and requires dedicated studies [247–251].

any signal detected at frequency scales of GW experiments is usually considered to be Gaussian, for various related reasons [197, 198, 242, 252]. One reason (as explained in [242, 252]) is that any higher order, connected correlation of signals detected with GW experiments typically involves angular integrations of contributions from many different, causally disconnected patches of the sky. By the central limit theorem, such linear superposition of signals from different directions tend to suppress any existing nG in GWs originating from each independent patch. Other more concrete reasons, as spelled out in full detail in the recent works [197, 198] are as follows: on their way through large cosmological distances from source to detection, GWs can collect random phases induced by long-wavelength matter fluctuations, which tend to suppress existing non-Gaussian phase correlations among GW signals. Moreover, due to the finite time of measurement, GW momenta can not be resolved perfectly, and such uncertainty again suppresses non-Gaussian effects when measuring higher order correlators [2].

A common feature of the cases studied so far, and partly at the root of the problems mentioned above, is that the corresponding GW signal 3-point function is not stationary: the value of the 3-point correlator of GW signal evaluated at equal time (say t) depends on the value of t. In this work, to overcome this problem, we introduce and characterize the concept of *stationary graviton non-Gaussianity*. It is characterized by higher-order correlators with two important porperties: they are invariant under time translation symmetry, and (as a consequence) they select GWs propagating along a common direction. Such features eliminate possible phase differences accumulating along the way GW travel from source to detection. They can then allow one to avoid the previous problems, making stationary graviton nG an observable that can be potentially probed by measuring

[2]Possible ways out to these negative conclusions have been proposed, involving measurements of quantities only indirectly sensitive to graviton nG: the quadrupolar anisotropy of the SGWB power spectrum, an observable which depends on the squeezed limit of tensor non-Gaussian correlation functions [1, 155, 253]; and higher-order correlations among spatial anisotropies in the distribution function of the GW energy density [254].

3-point functions of the SGWB with GW experiments. When evaluated in momentum space, stationary nG corresponds to a folded (also dubbed flattened) shape of tensor nG [3]. In Section 4.2, we first characterize general properties of this category of non-Gaussian, stationary signals, and explain why they have the opportunity to avoid the problems investigated in [197, 198]. We then discuss prospects to detect stationary non-Gaussianity with pulsar timing arrays (PTA).

Besides interferometers, another promising tool for detect SGWBs is based on observations of time residuals from large arrays of pulsars, which can detect the passage of GWs by tiny changes in their precisely measured periods. They can detect GWs at small frequencies of around $10^{-7} - 10^{-9}$ Hz. Several collaborations are studying pulsar data set in order to detect GW signals – EPTA [255], NANOGrav [256], PPTA [257] – and data are collected in an international collaboration called IPTA [258] which is currently monitoring 49 pulsars. In the relatively near future, SKA will considerably increase the number of monitored pulsars and the accuracy of measurements, see e.g. [259]. Theoretical studies of how the response of a PTA system to a SGWB have been started decades ago by the work of Hellings and Downs [260]. A more recent, detailed analysis of optimal signal-to-noise ratio and detectability prospects for a SGWB can be found in [261]. Reviews can be found in [243, 262, 263]. See also [264] for a study of overlap functions for 3-point non-Gaussian correlators with PTA (we will discuss in footnote 6 the differences between [264] and our work). Discussions on tests of deviations from General Relativity with PTAs can be found e.g. in [265–267].

In Section 4.3, we study overlap functions for PTA systems associated with stationary graviton nG. We do so in various different cases. We first consider 3-point overlap functions for PTA data aimed to detect correlations among spin-2 tensor modes of General Relativity. We then study

[3] The work [198] already pointed out that 3-point functions of GWs whose momenta are accurately aligned can avoid decorrelation effects.

3-point overlap functions including scalar excitations (the 'breathing mode' or transverse scalar graviton polarization), that are motivated by modified theories of gravity. We finally study correlations among different GW experiments (PTA and ground based interferometers), motivated by the fact 3-point functions associated with folded nG can correlate signals with very distinct frequencies.

Armed with these results, in Section 4.4 we determine the expression for the optimal signal-to-noise ratio to detect stationary nG in the SGWB. We investigate how the number of monitored pulsars and the geometry of the PTA system determine the optimal SGWB. We compute some of the key geometrical quantities characterizing the optimal SNR with data from IPTA collaboration. Our results give a quantitative indication that monitoring a large number of pulsars can increase the signal-to-noise ratio associated with measurements of stationary graviton nG.

4.2 Characterization of a stationary non-Gaussian SGWB

In this Section we discuss necessary conditions to make graviton non-Gaussianity an observable that can be directly probed in terms of 3-point correlation functions of a SGWB. We assume that the SGWB background is *stationary*, meaning that all correlators are time translationally invariant. If they were not, destructive interference effects are expected to set them to zero. Additionally, we shall also assume that parity is conserved, and that the background geometry preserves 3-dimensional spatial isotropy.

The GW spin-2 tensor mode in transverse-traceless gauge is expanded in Fourier modes as

$$h_{ab}(t,\vec{x}) = \sum_{\lambda} \int_{-\infty}^{\infty} df \int d^2\hat{n}\, e^{-2\pi i f \hat{n}\vec{x}}\, e^{2\pi i f t}\, \mathbf{e}_{ab}^{(\lambda)}(\hat{n})\, h_\lambda(f,\hat{n})\,, \tag{4.2.1}$$

with f the GW frequency, and $\hat{n}$ the unit vector corresponding to the GW direction. The product $2\pi f \hat{n}$ corresponds to the 3-momentum of the GW. The condition $h_\lambda(f,\hat{n}) = h_\lambda^*(-f,\hat{n})$ ensures that the function $h_{ab}(t,\vec{x})$ is real. The sum runs over chirality index $\lambda = L, R$, and $\mathbf{e}_{ab}^{(\lambda)}(\hat{n})$ denotes the polarization tensor: see Appendix C.1 for our conventions on these quantities. In (4.2.1) we integrate over positive as well as negative frequencies f, so to maintain a concise expression [268].

Being the SGWB by hypothesis stationary, all correlators depend on time differences only. In other words, correlators in real space as

$$\langle h_{a_1 b_1}(t_1,\vec{x}_1) \dots h_{a_n b_n}(t_n,\vec{x}_n)\rangle \tag{4.2.2}$$

depend only on $t_1 - t_n$ for each n and are invariant under time translation. This condition is easily achieved for the case of 2-point correlation functions. Assuming to correlate two modes with frequencies $f_{1,2}$ of opposite signs (say $f_1 > 0$), the 2-point correlator in Fourier space has the standard structure

$$\langle h_{\lambda_1}(f_1,\hat{n}_1) h_{\lambda_2}(f_2,\hat{n}_2)\rangle = \delta^{(3)}\left(f_1\hat{n}_1 + f_2\hat{n}_2\right)\delta^{\lambda_1\lambda_2} P(f_1)\,, \tag{4.2.3}$$

$$= \delta\left(f_1 + f_2\right)\delta^{(2)}\left(\hat{n}_2 - \hat{n}_3\right)\delta^{\lambda_1\lambda_2} P(f_1)\,, \tag{4.2.4}$$

with $P(f)$ the power spectrum depending on frequency. In the second line, we used the fact that the 3-dimensional δ-function implies the condition $f_1\hat{n}_1 = -f_2\hat{n}_2$. Taking the square of this expression one gets $f_1^2 = f_2^2 \Rightarrow f_1 = -f_2$ (recall that we are working with positive as well as negative frequencies) and hence $\hat{n}_1 = \hat{n}_2$.

The δ-functions make the correlator in eq (4.2.13) isotropic (the waves come from the same direction) and stationary. Stationarity is evident in the 2-point correlator in real space:

$$\begin{aligned}\langle h_{a_1b_1}(t_1,\vec{x}_1)h_{a_2b_2}(t_2,\vec{x}_2)\rangle &= \sum_{\lambda_1\lambda_2}\int_{-\infty}^{\infty} df_1 df_2 \int d^2\hat{n}_1\, d^2\hat{n}_2 \\ &\times\ e^{2\pi i f_1 t_1}\, e^{2\pi i f_2 t_2}\, \delta\left(f_1+f_2\right)\, \delta^{(2)}\left(\hat{n}_2-\hat{n}_3\right) \\ &\times\ \mathbf{e}^{(\lambda_1)}_{a_1b_1}(\hat{n}_1)\, \mathbf{e}^{(\lambda_2)}_{a_2b_2}(\hat{n}_2)\, \delta^{\lambda_1\lambda_2}\, P(f_1) \qquad (4.2.5)\\ &= \sum_{\lambda_1}\int_{-\infty}^{\infty} df_1 \int d^2\hat{n}_1\, e^{2\pi i f_1 (t_1-t_2)} \\ &\times\ \mathbf{e}^{(\lambda_1)}_{a_1b_1}(\hat{n}_1)\, \mathbf{e}^{(\lambda_1)}_{a_2b_2}(\hat{n}_1)\, P(f_1)\,.\end{aligned}$$

The previous expression is time-translationally invariant, since it depends only on the time difference $(t_2 - t_1)$ appearing in the exponential term of eq (4.2.6).

What about higher-order, connected n-point functions? The crucial feature of expression (4.2.13) which leads to time-translation invariance in real space is the presence of the δ-function in frequencies, $\delta(f_1 + f_2)$.

We then *postulate* that the same property holds for the 3-point function in Fourier space, and write the Ansatz

$$\begin{aligned}\langle h_{\lambda_1}(f_1,\hat{n}_1)h_{\lambda_2}(f_2,\hat{n}_2)h_{\lambda_3}(f_3,\hat{n}_3)\rangle &= \delta\left(f_1+f_2+f_3\right)\,\langle h_{\lambda_1}(f_1,\hat{n}_1) \\ &\times\ h_{\lambda_2}(f_2,\hat{n}_2)h_{\lambda_3}(f_3,\hat{n}_3)\rangle_{\rm st.} \qquad (4.2.6)\end{aligned}$$

where the label st means stationary. A non-vanishing 3-pt correlator with this property characterizes what we shall call *stationary graviton non-Gaussianity* (nG). Indeed, substituting the decomposition (4.2.6) in the three point correlator in coordinate space, and using eq (4.2.1) to express correlators, we obtain the expression (we integrate over f_3 and use the δ-function appearing in eq (4.2.6))

$$\langle h_{a_1b_1}(t_1,\vec{x}_1)h_{a_2b_2}(t_2,\vec{x}_2)h_{a_3b_3}(t_3,\vec{x}_3)\rangle = \sum_{\lambda_1\lambda_2\lambda_3}\int_{-\infty}^{\infty} df_1 df_2 \int d^2\hat{n}_1\, d^2\hat{n}_2\, d^2\hat{n}_3$$

$$
\begin{aligned}
&\times \quad e^{2\pi i f_1 (t_1 - t_3)}\, e^{2\pi i f_2 (t_2 - t_3)} \\
&\times \quad e^{-2\pi i f_1 (\hat{n}_1 \vec{x}_1 - \hat{n}_3 \vec{x}_3)}\, e^{-2\pi i f_2 (\hat{n}_2 \vec{x}_2 - \hat{n}_3 \vec{x}_3)} \\
&\times \quad \mathbf{e}^{(\lambda_1)}_{a_1 b_1}(\hat{n}_1)\, \mathbf{e}^{(\lambda_2)}_{a_2 b_2}(\hat{n}_2)\, \mathbf{e}^{(\lambda_3)}_{a_3 b_3}(\hat{n}_3) \\
&\times \quad \langle h_{\lambda_1}(f_1, \hat{n}_1) h_{\lambda_2}(f_2, \hat{n}_2) \\
&\times \quad h^*_{\lambda_3}(f_1 + f_2, \hat{n}_3) \rangle_{\rm st} \,. \qquad (4.2.7)
\end{aligned}
$$

Since it depends only on time differences, this correlator is time translationally invariant, as desired, hence the 3-point function is stationary.

At this level, our stationary Ansatz (4.2.6) is purely phenomenological, being it introduced to realize the stationary condition (4.2.7). But it is not difficult to characterise the 3-point function in Fourier space. Indeed, the statistical isotropy of the fluctuations also requires that the Fourier space correlator (4.2.6) is proportional to the three dimensional $\delta-$function acting on the three momenta, meaning that the vectors $f_i \hat{n}_i$ form a closed triangle (the label iso means isotropic):

$$
\begin{aligned}
&\langle h_{\lambda_1}(f_1, \hat{n}_1) h_{\lambda_2}(f_2, \hat{n}_2) h_{\lambda_3}(f_3, \hat{n}_3) \rangle \, = \\
&\delta^{(3)}(f_1 \hat{n}_1 + f_2 \hat{n}_2 + f_3 \hat{n}_3)\, \langle h_{\lambda_1}(f_1, \hat{n}_1) h_{\lambda_2}(f_2, \hat{n}_2) h_{\lambda_3}(f_3, \hat{n}_3) \rangle_{iso} \,. \qquad (4.2.8)
\end{aligned}
$$

We now show that, taken together with the condition (4.2.8), the stationarity condition of eq (4.2.6) selects only 'folded' (also called flattened) triangles in moment space, whose sides are exactly superimposed. Since the sum over frequencies vanish for the stationarity condition, one of the two frequencies has sign opposite to the other one: without lack of generality, we can take $f_{1,2} > 0$ and $f_3 < 0$. We write the two conditions (4.2.6) and (4.2.8) as

$$
\begin{aligned}
f_3 \hat{n}_3 &= -f_1 \hat{n}_1 - f_2 \hat{n}_2 \,, \qquad (4.2.9) \\
f_3 &= -f_1 - f_2 \,. \qquad (4.2.10)
\end{aligned}
$$

Taking the square of both sides of (4.2.9), we get the condition

$$f_3^2 \;=\; f_1^2 + f_2^2 + 2\, f_1 f_2\, \hat{n}_1 \cdot \hat{n}_2 \,. \tag{4.2.11}$$

Consider finite, non-vanishing values for f_i: the only way to make eq (4.2.11) compatible with the square of both sides of eq (4.2.10) is to require $\hat{n}_1 \cdot \hat{n}_2 = 1$. Contracting eq (4.2.9) with $\hat{n}_1$, and using this result, we obtain

$$f_3\, \hat{n}_3 \cdot \hat{n}_1 \;=\; -f_1 - f_2 \,, \tag{4.2.12}$$

which is compatible with eq (4.2.10) only if $\hat{n}_1 \cdot \hat{n}_3 = 1$. Hence the condition of stationarity is equivalent to consider folded triangles in momentum space, with superimposed sides. In other words, $\hat{n}_i \cdot \hat{n}_j = 1$ for each $\hat{n}_i$, and the directions characterizing the GW modes entering the three-point correlator lie on the same line. See Fig 4.1 for a graphical representation of examples of folded triangles in momentum space, corresponding to folded nG.

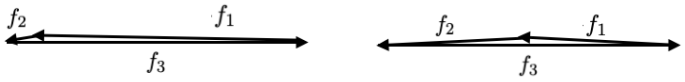

FIGURE 4.1: *Representation of folded (also called flattened) triangles. Here $f_{1,2} > 0$, $f_3 < 0$. The triangle sides are intended to be superimposed, with vanishing angles between the sides (f_1, f_3) and (f_2, f_3). The side lengths can be very different (e.g. $f_1 \sim |f_3| \gg f_2$, left plot) or comparable in size (e.g. $f_1 \sim f_2 \sim |f_3|/2$, right plot).*

To summarize, the condition of stationarity requires that the two and three point functions of tensor modes in Fourier space read, if none of the f_i is vanishing small [4]:

[4] In the squeezed case (one of the f_i vanishes) then the condition of stationarity it is not necessarily associated with the condition of superimposed triangle sides. The consequences of squeezed configurations for modulating the tensor power spectrum have been recently investigated in [253].

$$\begin{aligned}\langle h_{\lambda_1}(f_1,\hat{n}_1)h_{\lambda_2}(f_2,\hat{n}_2)\rangle &= \delta\left(f_1+f_2\right)\delta^{(2)}\left(\hat{n}_1-\hat{n}_2\right)\\ &\times\ \delta^{\lambda_1\lambda_2}P(f_1)\,, \qquad (4.2.13)\\ \langle h_{\lambda_1}(f_1,\hat{n}_1)h_{\lambda_2}(f_2,\hat{n}_2)h_{\lambda_3}(f_3,\hat{n}_3)\rangle &= \delta\left(f_1+f_2+f_3\right)\delta^{(2)}\left(\hat{n}_1-\hat{n}_3\right)\\ &\times\ \delta^{(2)}\left(\hat{n}_2-\hat{n}_3\right)\\ &\times\ B^{\lambda_1\lambda_2\lambda_3}(f_1,f_2,\hat{n}_\star)\,, \qquad (4.2.14)\end{aligned}$$

where in the last line we introduced the function $B^{\lambda_{1,2,3}}$, the tensor bispectrum associated to scenarios with stationary nG. Such bispectrum is characterized by flattened triangle shapes [5] (see Fig 4.1).

For the rest of this work, we shall focus on stationary correlators of the form in eqs (4.2.13), (4.2.14). Folded non-Gaussianity is known to arise in the scalar sector of specific models of inflation, see e.g. [269–272]. It would be interesting to investigate models where the same shape of nG arise in the tensor sector, for example in models with extra spin-2 degrees of freedom in an EFT approach to inflation (see e.g. [221, 222]). We do not pursue the problem of model building any further in this work, but we instead continue with characterizing the interesting properties of stationary graviton nG. It is also worth noticing that – even if the background is isotropic – the tensor bispectrum can distinguish among different chiralities, since its amplitude depends on the value of the chirality indexes λ_i.

Substituting the 3-point function in (4.2.14) into eq (4.2.7), we find the concise expression

[5] It is important to notice that $B^{\lambda_{1,2,3}}$ depends on a specific reference direction, that we denote with $\hat{n}_\star$: this is due to the fact that tensor modes transform under spatial rotations, and the definition of polarization tensors depends on such specific, selected direction. Our results for the overlap functions in the next Section then depend on the choice of $\hat{n}_\star$: see also [199] for a detailed discussion on this point.

$$\begin{aligned}\langle h_{a_1b_1}(t_1,\vec{x}_1)h_{a_2b_2}(t_2,\vec{x}_2)h_{a_3b_3}(t_3,\vec{x}_3)\rangle \;=\; & \sum_{\lambda_1\lambda_2\lambda_3}\int_{-\infty}^{\infty} df_1 df_2 \int d^2\hat{n} \\ \times\; & \mathbf{e}^{(\lambda_1)}_{a_1b_1}(\hat{n})\,\mathbf{e}^{(\lambda_2)}_{a_2b_2}(\hat{n})\,\mathbf{e}^{(\lambda_3)}_{a_3b_3}(\hat{n}) \\ \times\; & e^{2\pi i f_1 (t_1-t_3)}\, e^{2\pi i f_2 (t_2-t_3)} \\ \times\; & e^{-2\pi i f_1 \hat{n}\cdot(\vec{x}_1-\vec{x}_3)}\, e^{-2\pi i f_2 \hat{n}\cdot(\vec{x}_2-\vec{x}_3)} \\ \times\; & B^{\lambda_1\lambda_2\lambda_3}(f_1,\, f_2,\, \hat{n}_\star)\,, \qquad (4.2.15)\end{aligned}$$

that makes stationarity and isotropy particularly transparent.

4.2.1 On the local observability of stationary graviton non-Gaussianity in a SGWB

We conclude this Section discussing some interesting properties of (4.2.15). Tensor 3-point functions satisfying the stationarity condition (4.2.14) do not necessarily suffer from decorrelation effects as discussed in [197, 198, 242, 252]. Such effects are associated with phase decorrelations among different waves coming from several distinct causally disconnected regions, a process that tends to 'Gaussianize' the system for the central limit theorem. Interestingly, in our case, the delta-function conditions on the wave-vectors given in eq (4.2.14) (a consequence of stationarity) ensure us that GWs come from the same direction. This is particularly clear from eq (4.2.15), where the angular integral is carried over the single direction of propagation of the waves (see also Fig 4.2). The work [198] already pointed out that contributions to 3-point functions for which GW momenta are accurately aligned can avoid decorrelation effects. Our concept of stationary graviton nG singles out the category of tensor nG whose support is enhanced for such configurations, which are the only ones that can be probed by measurements of 3-point functions of GW signals.

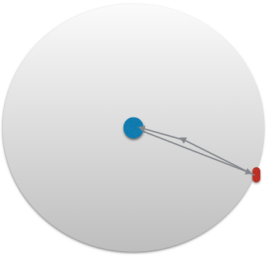

FIGURE 4.2: *The structure of the 3-point function in eq (4.2.14) requires that the three GWs entering in the correlator originate from a common direction $\hat{n}$ in the sky. In the graphical representation above, we show with the red spot the common region of emission of three GWs (which can be of cosmological origin); with the blue blob the region containing GW detectors (which can be of astrophysical size, as in the case of PTA experiments). The lines with arrows (that we intend as superimposed) indicate the GW common direction $\hat{n}$.*

Besides this effect, [197] shows that GWs, in their (possibly long) way from source to detection, can collect random phases induced by long-wavelength energy fluctuations. These phases, physically associated with a Shapiro time delay effect, influence the short-wavelength GW modes propagating over cosmological distances. Indeed, they tend to suppress phase correlations of initially non-Gaussian fields, and to reduce the amplitude of connected n-point tensor correlation functions with $n \geq 3$. In our case, correlators depend on time differences only. Hence they are not sensitive to the entire time-travel of the wave from emission to detection, but only to the relatively short time-scale of the experiment. Although this is a more model dependent issue – depending on how long wavelength matter fluctuations influence tensor geodesics – we can develop some semi-quantitative argument as follows. The effect of long wavelength modes can be expressed in terms of coordinate redefinitions [273], which depend on time and on position. Following [197], we focus on the effect of long wavelength curvature fluctuations, and describe their effect in terms of a shift of time coordinate. We express the graviton mode in real space as

$$h_{ab}(t,\vec{x}) = \sum_{\lambda} \int_{-\infty}^{\infty} df \int d^2\hat{n}\, e^{-2\pi i f \hat{n}\vec{x}}\, e^{2\pi i f (t+Z(t,\hat{n}))}\, \mathbf{e}^{(\lambda)}_{ab}(\hat{n})\, h_{\lambda}(f,\hat{n})\,, \tag{4.2.16}$$

where the function $Z(t, \hat{n})$ in the exponent (depending on time and GW direction) characterizes the effect of the long mode. In taking the equal time 3-point function in coordinate space using eq (4.2.16), and making use of stationary correlation properties as in eq (4.2.14), the δ-functions in the GW directions force all the arguments of the Z functions to be equal, and the δ-functions in frequencies force them to cancel. The result is not dependent on time, nor on Z. Hence, long modes – when described as above – do not influence the equal-time 3-point function. It would be interesting to formalize this argument more precisely, but such analysis deserves more extensive work that we leave to a future publication.

4.3 Pulsar Timing Array overlap functions

We now investigate techniques to probe stationary tensor nG with pulsar timing arrays (from now on, PTA). Precision measurements of time delays in pulsar periods can allow astronomers to extract interesting information on the physics of the GW sector. Pulsar time delays can be due to a GW which deform the space-time by passing between the pulsar and the earth; to intrinsic pulsar period variations; or to some unknown or less-known noise sources. By correlating measurements from distinct pulsars, noise can be reduced, and possible GW signal revealed. A correlation between different time-delay measurements lead to the concept of *overlap function*, which quantifies the response of a set of GW detectors to GWs with a given frequency. Starting from the overlap function, it is then possible to estimate the signal-to-noise ratio associated to dedicated GW observables aimed at characterising the non-Gaussian properties of a SGWB. In this Section, after reviewing in Section 4.3.1 well known results on 2-point overlap functions for PTA observations, we pass to discuss 3-point functions specializing to the case of stationary graviton non-Gaussianity. In particular:

1. In Section 4.3.2 we discuss overlap functions for pulsar timing arrays designed to probe tensor non-Gaussianity with folded shapes, corresponding to stationary graviton non-Gaussianity (see Section 4.2). When correlating GW measurements from PTA experiments we expect the signals to have comparable frequencies. Hence we probe flattened triangle shapes with comparable side lengths in momentum space, corresponding to the right panel of Fig 4.1. [6]

2. The tensor bispectrum can correlate also modes with different spins (e.g. tensors with scalars). This might lead to interesting observables when investigating theories of modified gravity with extra degrees of freedom (as in scalar-tensor theories). For the first time, in Section 4.3.3 we compute mixed 3-point overlap functions for GW experiments correlating tensor and scalar fluctuations, specialising to the case of PTA experiments.

3. A stationary tensor 3-point function can also correlate GWs with very distinct frequencies, as long as they satisfy the δ-function constraints of eq (4.2.14): an example is the flattened triangle in momentum space of Fig 4.1 (left panel) in which one of the frequencies is much smaller than the others. This implies that triangle configurations can be probed by correlating different experiments operating over different frequency ranges. For the first time, in Section 4.3.4 we build overlap functions correlating distinct experiments: PTA (detecting SGWBs at frequencies of order $f_{\rm PTA} \sim 10^{-9} - 10^{-7}$ Hz) and ground based detectors (operating at frequencies of $f_{\rm GB} \sim 10^{0} - 10^{3}$ Hz).

Following the review in [243], we define the total time-delay output s_α measured by a GW experiment based on a PTA system as sum of a GW signal σ_α, and the noise n_a. We assume that the noise is uncorrelated with

[6] An interesting study of PTA 3-point overlap functions, with the aim of to investigate tensor non-Gaussianity, has been carried on in [264]. But that work did not specifically analyzed flattened triangular shapes, that as we learned are the physically relevant ones in the context of stationary non-Gaussianity.

the GW signal, and both have average zero. For any GW propagating in the direction $\hat{n}$, we define the signal detected by the PTA in terms of the relative time delay induced by the GW on the pulsar period

$$\sigma_\alpha(t) \equiv \frac{\Delta T_\alpha}{T_\alpha} = \frac{x^i_\alpha\, x^j_\alpha}{2(1+\hat{n}\cdot\hat{x}_\alpha)}\left[h_{ij}(t,\vec{x}=0) - h_{ij}(t-\tau_\alpha,\vec{x}_\alpha)\right], \tag{4.3.1}$$

where the Earth is located at position $\vec{x} = 0$, while the pulsar α is located at position $\vec{x} = \vec{x}_\alpha$. τ_α is the light travel time from the pulsar to the Earth and $\hat{x}_a$ the unit vector between the Earth and the pulsar position. Expressing this quantity in Fourier space, we find

$$\sigma_\alpha(t) = \sum_\lambda \int_{-\infty}^{\infty} df \int d^2\hat{n}\; F^{(\lambda)}_\alpha(\hat{n})\, e^{2\pi i f t}\, h_\lambda(f,\hat{n}) \left(1 - e^{-2\pi i f \tau_\alpha}\, e^{-2\pi i f \hat{n}\vec{x}_\alpha}\right), \tag{4.3.2}$$

where we introduce the detector tensor

$$F^{(\lambda)}_\alpha(\hat{n}) = \frac{x^i_\alpha\, x^j_\alpha\, \mathrm{e}^{(\lambda)}_{ij}(\hat{n})}{2(1+\hat{n}\cdot\hat{x}_\alpha)}, \tag{4.3.3}$$

which depends only on the GW direction, but not on the GW frequency f.

4.3.1 Two-point overlap functions

The simplest possibility to consider is the 2-point correlation function. We review this well known case here, before discussing new results for the 3-point overlap function for stationary nG. The 2-point function for the GW modes is given in eq (4.2.13). The equal-time 2-point correlation function for the PTA time-delay signal reads

$$\begin{aligned}\langle \sigma_\alpha(t)\sigma_\beta(t)\rangle \;=\; & \sum_{\lambda_1\lambda_2}\int_{-\infty}^{\infty} df_1 df_2 \int d^2\hat{n}_1 d^2\hat{n}_2\; F^{(\lambda_1)}_\alpha(\hat{n}_1) F^{(\lambda_2)}_\beta(\hat{n}_2) \\ & \times\; e^{2\pi i (f_1+f_2)t}\, P(f_1)\; \delta^{(2)}(\hat{n}_1-\hat{n}_2)\, \delta(f_1+f_2)\, \delta_{\lambda_1\lambda_2} \\ & \times\; \left(1 - e^{-2\pi i f_1 \tau_\alpha (1+\hat{n}_1\,\hat{n}_\alpha)}\right)\left(1 - e^{-2\pi i f_2 \tau_\beta (1+\hat{n}_2\,\hat{n}_\beta)}\right).\end{aligned} \tag{4.3.4}$$

For pulsars at typical distances of 10^3 parsec, taking into account the frequency range probed by PTA, one finds that the quantity $f\tau_\alpha \sim \mathcal{O}(10^2)$. This implies that contributions containing exponentials in the pulsar terms, in the second line of the previous equation, are rapidly oscillating functions that are averaged out in the integral over directions $\hat{n}$. Hence we can neglect these terms and substitute the second line with a unit factor.

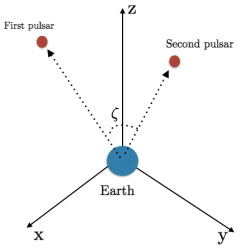

FIGURE 4.3: *Representation of a system of two pulsars, and the earth. We denote with ζ the angle between the unit vectors from the earth towards each of the pulsars.*

Under this approximation, making use of the δ functions, we can assemble the angular integral into a response function, and express the previous quantity as

$$\langle \sigma_\alpha(t)\sigma_b(t)\rangle \;=\; 2\pi \sum_\lambda \int df\, \mathcal{R}^{(\lambda)}_{\alpha\beta}\, P(f)\,, \tag{4.3.5}$$

where the PTA 2pt response function is given by an angular integration, leading to the so-called Hellings-Down overlap function [260] (see also [243, 261, 274]):

$$\mathcal{R}^{(\lambda)}_{\alpha\beta}(\zeta) \;=\; \int \frac{d^2\hat{n}}{2\pi}\, F^{(\lambda)}_\alpha(\hat{n}) F^{(\lambda)}_\beta(\hat{n})\,, \tag{4.3.6}$$

$$\;=\; \frac{1}{6} - \frac{(1-\cos\zeta)}{24}\left(1 - 6\,\ln\left(\frac{1-\cos\zeta}{2}\right)\right), \tag{4.3.7}$$

where

$$\cos\zeta \equiv \hat{x}_\alpha \cdot \hat{x}_\beta\,. \tag{4.3.8}$$

It is important to stress that the Hellings-Down function $\mathcal{R}^{(\lambda)}_{\alpha\beta}$ depends only on angle ζ between pulsar directions, and not on the GW frequency. In Fig 4.4 we represent the profile of the sum of overlap functions over polarization indexes, $\mathcal{R}_{\alpha\beta}(\zeta) = \sum_\lambda \mathcal{R}^{(\lambda)}_{\alpha\beta}$.

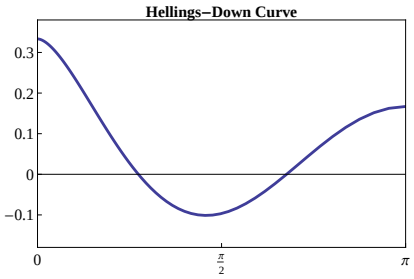

FIGURE 4.4: *The 2-point overlap function for the sum of the spin-2 polarizations $\mathcal{R}_{ab}(\zeta) = \sum_\lambda \mathcal{R}^{(\lambda)}_{ab}$ (the so-called Hellings-Down curve [260]). The x-axis contain the angle ζ defined in eq (4.3.8). The y-axis the corresponding value of the overlap function, see eq (4.3.6).*

4.3.2 Three-point overlap functions

We now analyze the 3-point overlap function for flattend tensor bispectra satisfying a stationarity condition, as described in Section 4.2. Such shapes of tensor bispectra were not specifically investigated in [264], hence our results are new. In correlating signals from different pulsars, we assume that the frequencies of the GWs are comparable, hence the flattened tensor bispectra in momentum space have a shape with sides of similar size, see the right panel of Fig 4.1.

The tensor 3-point function in Fourier space is given by eq (4.2.14). The PTA signal equal-time 3pt function then results, using the notation of the previous subsection, is

$$\begin{aligned}\langle \sigma_\alpha(t)\sigma_\beta(t)\sigma_\gamma(t)\rangle &= \sum_{\lambda_1\lambda_2\lambda_3}\int_{-\infty}^{\infty} df_1 df_2 \int d^2\hat{n}\, F^{(\lambda_1)}_\alpha(\hat{n}) F^{(\lambda_2)}_\beta(\hat{n}) \\ &\times F^{(\lambda_3)}_\gamma(\hat{n})\, B^{\lambda_1\lambda_2\lambda_3}(f_1, f_2, \hat{n}_\star)\,.\end{aligned} \tag{4.3.9}$$

We now conveniently collect the angular integration in the definition of the 3-point overlap function $\mathcal{R}^{\lambda_1\lambda_2\lambda_3}_{\alpha\beta\gamma}(\hat{n}_\star)$:

$$\begin{aligned}\langle\sigma_\alpha(t)\sigma_\beta(t)\sigma_\gamma(t)\rangle &= \sum_{\lambda_1\lambda_2\lambda_3} 2\pi \int_{-\infty}^{\infty} df_1 df_2\, \mathcal{R}^{\lambda_1\lambda_2\lambda_3}_{\alpha\beta\gamma}(\hat{n}_\star) \\ &\times B^{\lambda_1\lambda_2\lambda_3}(f_1, f_2, \hat{n}_\star)\,. \end{aligned} \tag{4.3.10}$$

To perform such angular integrations, we introduce a rotation matrix $M[\theta, \phi]$:

$$M[\theta, \phi] = \begin{pmatrix} \sin\theta\cos\phi & \cos\theta\cos\phi & -\sin\phi \\ \sin\theta\sin\phi & \cos\theta\sin\phi & \cos\phi \\ \cos\theta & -\sin\theta & 0 \end{pmatrix}. \tag{4.3.11}$$

We rotate over the reference direction $n_\star$: $\hat{n} = M[\theta, \phi]\,\hat{n}_\star$, so to write

$$\begin{aligned}\mathcal{R}^{\lambda_1\lambda_2\lambda_3}_{\alpha\beta\gamma}(\hat{n}_\star) &= \tfrac{1}{2\pi}\int_0^{2\pi} d\phi \int_0^{\pi} \sin\theta\, d\theta \\ &\times\Big[F^{(\lambda_1)}_\alpha(M\,\hat{n}_\star)F^{(\lambda_2)}_\beta(M\,\hat{n}_\star)F^{(\lambda_3)}_\gamma(M\,\hat{n}_\star) + (\lambda_i \to -\lambda_i)\Big]\,. \end{aligned} \tag{4.3.12}$$

Notice that the PTA 3-point overlap function depends on the chirality of the GW, the relative position of pulsars, and the reference direction $\hat{n}_\star$. From now on, in this work we select $\hat{n}_\star$ to point along the $\hat{x}$ axis:

$$\hat{n}_\star = (1, 0, 0)\,. \tag{4.3.13}$$

On the other hand, the overlap function does *not* depend on the frequency since (for the same arguments discussed in Section 4.3.1) we can safely neglect the earth terms. In what follows, we do not consider scenarios including parity violation, and we sum over opposite chiralities. In other words, indicating $R = +$ and $L = -$, we compute and plot the sum $\mathcal{R}^{\lambda_1\lambda_2\lambda_3}_{\alpha\beta\gamma} + \mathcal{R}^{-\lambda_1-\lambda_2-\lambda_3}_{\alpha\beta\gamma}$, as done in Section 4.3.1 for the 2-point overlap function.

Evaluating the precise angular structure of $\mathcal{R}^{\lambda_1\lambda_2\lambda_3}_{\alpha\beta\gamma}(\hat{n}_\star)$ is essential for estimating the optimal signal-to-noise ratio of an experiment to measure a stationary tensor bispectrum, as we shall learn in Section 4.4. In the next

two subsections, we evaluate the 3-point overlap functions in two different configurations.

4.3.2.1 3-point overlap function: two signals from the same pulsar

In this subsection we compute the overlap function for a case where we correlate two time-delay signals from the same pulsar α, with a third signal from a separate pulsar β. This case will be important for the discussion in Section 4.4. We consider the limit of equal time 3-point correlation

$$\langle \sigma_\alpha(t)\, \sigma_\alpha(t)\, \sigma_\beta(t) \rangle \,, \tag{4.3.14}$$

and we represent in Fig 4.5 for a graphical representation of the geometry of the system.

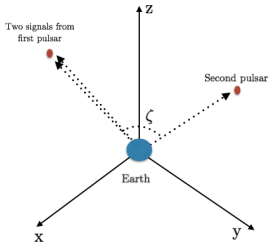

FIGURE 4.5: *Representation of a configuration where we correlate two signals measured at the same pulsar α with a signal for the distinct pulsar β.*

In this case we find that the 3-point overlap function depends only on the angle ζ between the vectors from the earth towards pulsars α and β. The general formula to compute such function is given by eq (4.3.12), with $\gamma = \beta$. The response function $\mathcal{R}^{\lambda_1\lambda_2\lambda_3}_{\alpha\beta\beta}$ depends on chirality, see Fig 4.6. Its magnitude is around few percent, depending on the value of ζ. We find $\mathcal{R}^{RRR}_{\alpha\beta\beta} = \mathcal{R}^{RLR}_{\alpha\beta\beta}$. Notice that these results are quite different from the

Hellings-Down profile reviewed in Section 4.3.1 for the 2-point function, in respect of size and angular profile.

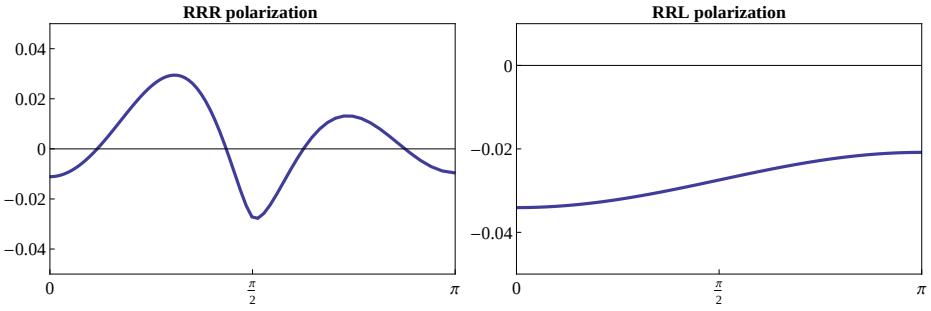

FIGURE 4.6: *3-point overlap functions associated with stationary, flattened bispectra, for correlating two signals from the same pulsar with a signal from another pulsar (see Fig 4.5). In the x-axis we vary the angle ζ between the unit vectors from the earth towards pulsars α and β. In the y-axis we represent the magnitude of the associated 3-point function, which depends on the polarization of the GWs.*

4.3.2.2 3-point overlap function: signals from from three distinct pulsars

When we correlate time-delay signals from three different pulsars, the result depends in a more complex way on the geometry of the system. For definiteness, here we focus our attention on a system where the three pulsars lie on orthogonal planes, (x, y), (x, z), (y, z): see Fig 4.7.

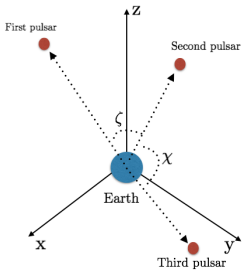

FIGURE 4.7: *A configuration with three pulsars lying on orthogonal planes. In this representative figure, ζ denotes the angle beween the unit vectors from the earth towards pulsar 1 and 2. χ denotes the angle beween the unit vectors from the earth towards pulsar 2 and 3.*

In this case, the 3-point overlap function depends on two angles ζ and χ between the vectors from earth towards the pulsars. We represent our results for the overlap functions in Fig 4.8, evaluated using the general formula (4.3.12). Also in this case the typical magnitude of the overlap function is of order of a few percent. On the other hand, the plots in Fig 4.8 also present peaks and valleys where the magnitude of the overlap function can increase by a factor of order one with respect to the 2-dimensional case studied in section 4.3.2.1.

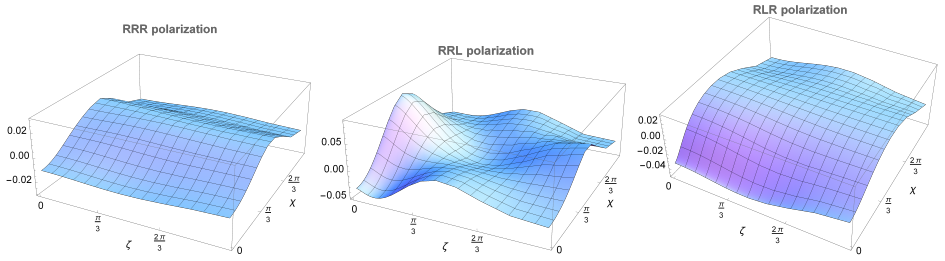

FIGURE 4.8: *Three-point overlap functions associated with stationary, flattened bispectra We locate the pulsars in three different orthogonal planes (say (xy), (yz), (xz)) and vary the angle ζ between the unit vectors from the earth towards pulsar 1 and 2, and χ the unit vectors from the earth towards pulsar 1 and 3. The z-axis represents the magnitude of the corresponding overlap function.*

4.3.3 Three-point overlap functions: correlating tensor and scalar polarizations

GW experiments can be sensitive also to vector and scalar polarizations of GWs, motivated by theories that modify General Relativity: see the interesting early works [275, 276] that first explored this possibility, and [265–267] for analysis that specifically cover PTA experiments. GW 2-point functions do not correlate fields of different spin (e.g. scalar and tensors) around an isotropic background; instead, correlations among different spins are possible at the level of 3-point functions. In this subsection, for the first time we investigate 3-point overlap functions describing the correlation of scalar GW polarizations with tensor (or scalar) polarizations. Our results

are model independent, and we do not refer to specific scenarios. But, for the same reasons discussed in the previous sections, we focus on stationary non-Gaussianity, associated with time-translation-invariant 3-point functions (that is, bispectra with folded shapes in momentum space). Our conventions for polarization tensors describing the transverse scalar 'breathing mode' GW polarization are standard and listed in Appendix C.1.

We first consider correlation of two signals from the same pulsar α with a signal from a distinct pulsar β, as in subsection 4.3.2.1. Figure 4.9 shows our result for the overlap function relative to a stationary bispectrum of folded shape, with correlate scalar and tensor modes. Interestingly, the magnitude of the overlap function in the presence of scalar excitations is larger than in the case of spin-2 modes only, and does not depend on the chirality (L/R) of tensors entering the correlators. As we shall see, this fact has some consequences in the computation of the signal-to-noise ratio.

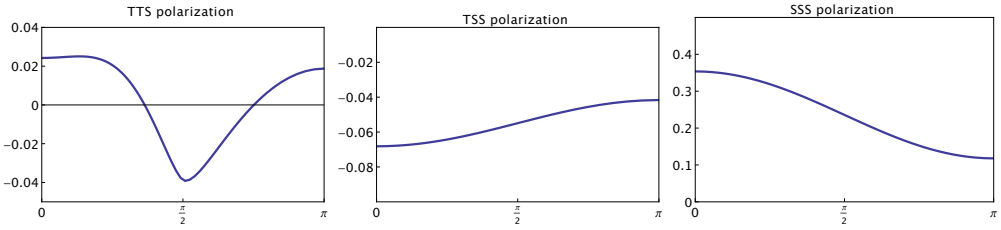

FIGURE 4.9: *Three-point overlap functions correlating two signals from the same pulsar α with a signal from second pulsar β. We vary the angle ζ between the unit vectors from the earth towards pulsar a and b. We correlate tensor* **T** *polarization with scalar* **S** *polarization.*

We then consider correlation of three signals from three distinct pulsars, with the condition that the three pulsars lie on orthogonal planes, as done in Section 4.3.2.2 in a purely tensor context. Figure 4.10 shows our results for the overlap functions for this case. Notice that for the pulsar configuration we consider the overlap function for scalar autocorrelations is flat.

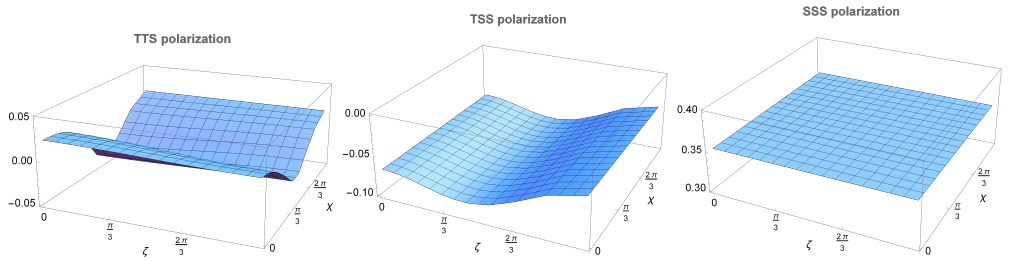

FIGURE 4.10: *Three-point overlap functions correlating scalar and tensor modes for signals from three different pulsars lying on orthogonal planes. We vary the angle ζ, χ between the unit vectors from the earth towards the pulsars. We correlate tensor (T) polarization with scalar (S) polarization.*

4.3.4 Three-point overlap functions: correlating PTA and ground-based experiments

Another interesting feature of stationary tensor nG is the possibility to correlate signals with very different frequencies, associated with triangles in momentum space for which one of the side lengths is much smaller than the other two (see Fig 4.1, left panel). In cases in which the frequencies involved differ by several orders of magnitude, it is interesting to correlate signals detected by PTA experiments with signals measured by ground-based experiments (e.g. LIGO) that work in the frequency range $10^0 - 10^3$ Hz. See Figure 4.11 for a graphical representation of the system.

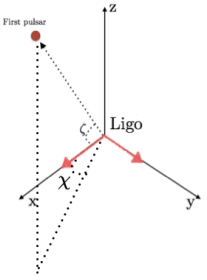

FIGURE 4.11: *Representation of a possible measurement where we correlate signals measured with PTA with signals detected with ground-based experiments (labelled as 'LIGO').*

The calculation of the corresponding overlap function is conceptually similar to what we have done so far: only the expression for the detector tensor (given in eq (4.3.3) for the PTA case) changes. In the small-antenna limit, the detector tensor for ground based experiments reads:

$$F_{\alpha}^{(\lambda)}(\hat{n}) = \frac{1}{2}\,\mathbf{e}_{ij}^{(\lambda)}\left(X_a^i\,X_a^j - Y_a^i\,Y_a^j\right), \tag{4.3.15}$$

with $\vec{X}_a$, $\vec{Y}_a$ indicating the arm directions of the interferometer α. It is sufficient to plug this expression for the detector tensor in the general formula (4.3.12) for the 3-point detector function to study the case of cross correlations among different experiments. We represent our results in Figs 4.12 and 4.13. In Fig 4.12, we correlate two signals from the same pulsar with a signal measured by a ground-based detector.

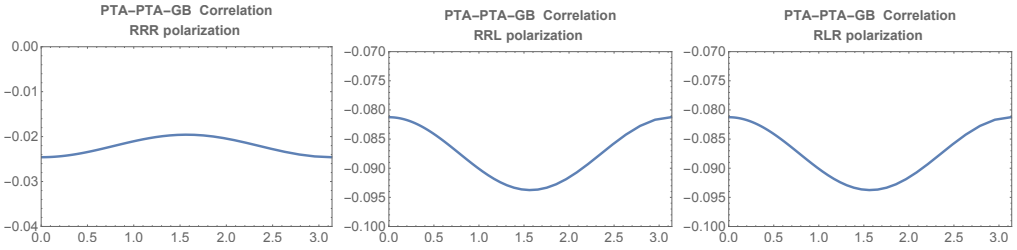

FIGURE 4.12: *3-point overlap functions for correlations between two signals from the same pulsar and a signal measured at a ground-based detector. We vary the angle ζ between the unit vectors from the earth and a direction of one of the ground based detector arms.*

In Fig 4.13, instead, we correlate one signal from a pulsar with two signals measured by the same ground based detector.

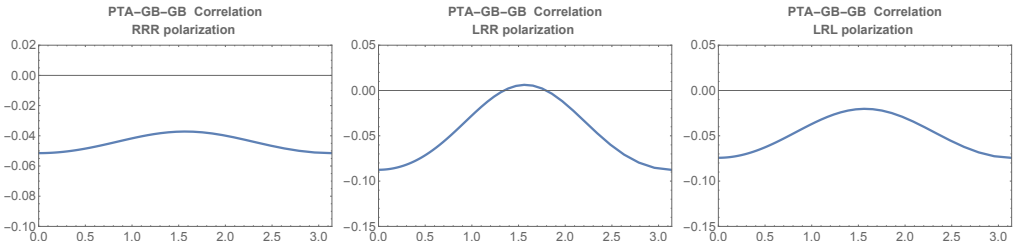

FIGURE 4.13: *3-point overlap functions for correlations between one signal from a pulsar and two signals measured at the same ground-based detector. We vary the angle ζ between the unit vectors from the earth and a direction of one of the ground based detector arms.*

4.4 The optimal signal-to-noise ratio for stationary tensor nG

Armed with the results of Section 4.3 on the PTA overlap functions, we now wish to determine the optimal way to correlate measurements from different pulsars, so to maximise the signal-to-noise ratio (SNR) when measuring stationary tensor bispectra in flattened configurations with Pulsar Timing Arrays. We call $s_\alpha(t)$ the output of the measurement at time t from pulsar α, which is the sum of GW signal $\sigma_\alpha(t)$ and noise $n(t)$. (And same for pulsars β, γ.) In order to carry on our computations, we make the following assumptions:

- We shall assume that the noise dominates over the GW signal. The total time T during which data are collected (5-10 years) is much larger than the typical frequency scale of the detected GWs (say $f \sim$ 10 nHz), so we work in a regime $fT \gg 1$.

- We will assume that the graviton bispectrum is very peaked in flattened configurations as described in Section 4.2, so that the condition of stationary bispectrum is very well realised, and any variance associated with the spread of the bispectrum shape is well smaller than the (dominant) instrumental noise as discussed in the previous bullet

point. It would be interesting to study concrete early universe models leading to graviton nG with this property, but we leave this for future work.

Under these hypothesis, we start deriving the expression for the optimal signal-to-noise ratio, which (as we shall see) depends on the frequency dependence of the tensor bispectrum, as we well as a constant geometrical quantity that we call $\mathtt{r}^{\lambda_1\lambda_2\lambda_3}$ (λ_i denoting the GW chirality). The quantity $\mathtt{r}^{\lambda_1\lambda_2\lambda_3}$ depends on the GW chirality and on the number and geometrical configuration of the pulsars in the PTA system under consideration. Towards the end of the section, we shall collect in a table the values for this quantity, when evaluated for the IPTA data set [258].

In order to estimate the optimal SNR, we generalise to the case of 3-point functions the methods described in the textbook [236] and the articles [261, 277]. The computation of the optimal SNR for tensor bispectrum has been already carried on in [199]: here we simplify the analysis by adapting the computation to the present context, where we focus on 'stationary' non-Gaussianity only, and on PTA measurements. We define the stationary three point correlator among a measurement performed with a triplet of pulsars, denoted with (α, β, γ):

$$\begin{aligned} \mathcal{Y}_{\alpha\beta\gamma} &= \int_{-T/2}^{T/2} dt_1 \int_{-T/2}^{T/2} dt_2 \int_{-T/2}^{T/2} dt_3 \\ &\times \; s_\alpha(t_1) s_\beta(t_2) s_\gamma(t_3) \;\; Q(t_3 - t_1)\, Q(t_3 - t_2)\,, \end{aligned} \tag{4.4.1}$$

where we integrate over the duration T of the experiment. In the previous expression, $Q(t_i - t_j)$ is a filter function, depending on time differences, which we assume decays very rapidly with increasing values of $|t_i - t_j|$. Notice that we include *two* copies of Q, in order to take into account the two independent time differences $(t_3 - t_1)$ and $(t_2 - t_1)$.

In the definition of SNR≡S/N, the quantity S (the signal) corresponds to the ensemble average value of $\mathcal{Y}_{\alpha\beta\gamma}$ when the signal is present; the quantity N

(the noise) is the root mean square value of $\mathcal{Y}_{\alpha\beta\gamma}$ when the signal is absent. In what comes next, we wish to determine the choice of filter function Q maximising the SNR.

We Fourier transform the expression (4.4.1):

$$\begin{aligned}\mathcal{Y}_{\alpha\beta\gamma} &= \int_{-\infty}^{\infty} df_A\, df_B\, df_1\, df_2\, df_3\ \delta_T(f_1 - f_A)\,\delta_T(f_2 - f_B)\,\delta_T(f_3 + f_A + f_B) \\ &\quad \times \tilde{s}_\alpha(f_1)\,\tilde{s}_\beta(f_2)\,\tilde{s}_\gamma(f_3)\,\tilde{Q}(f_A)\,\tilde{Q}(f_B)\,, \end{aligned} \tag{4.4.2}$$

and introduce the function $\delta_T(f) \equiv \left(\int_{-T/2}^{T/2} dt\, \exp 2\pi\, i\, ft\right)$. This function approaches the Dirac delta function for $T \to \infty$, and has the property that $\delta_T(0) = T$. We proceed integrating over the frequencies f_1, f_2. We get (in the physically relevant limit of large $f\,T$ where we can approximate δ_T with a δ function):

$$\begin{aligned}\mathcal{Y}_{\alpha\beta\gamma} &= \int_{-\infty}^{\infty} df_A\, df_B\, df_3\ \delta_T(f_3 + f_A + f_B) \\ &\quad \times \quad \tilde{s}_\alpha(f_A)\,\tilde{s}_\beta(f_B)\,\tilde{s}_\gamma(f_3)\,\tilde{Q}(f_A)\,\tilde{Q}(f_B)\,. \end{aligned} \tag{4.4.3}$$

We now compute the SNR≡S/N.

The signal S. Using the procedure outlined above, and equation (4.3.2) for the individual signals from each pulsar, we get the following expression for the total signal associated with the 3-pulsar measurement:

$$\begin{aligned} S &= \sum_{\lambda_1\lambda_2\lambda_3} \int_{-\infty}^{\infty} df_A\, df_B\, df_3\, d^2\hat{n}_1\, d^2\hat{n}_2\, d^2\hat{n}_3\, \delta_T(f_3 + f_A + f_B)\, F_\alpha^{\lambda_1}(\hat{n}_1)\, F_\beta^{\lambda_2}(\hat{n}_2) \\ &\times \quad F_\gamma^{\lambda_3}(\hat{n}_3)\, \langle h_{\lambda_1}(f_A, \hat{n}_1)\, h_{\lambda_2}(f_B, \hat{n}_2)\, h_{\lambda_3}(f_3, \hat{n}_3)\rangle\, \tilde{Q}(f_A)\,\tilde{Q}(f_B)\,, \end{aligned} \tag{4.4.4}$$

$$\begin{aligned} &= \sum_{\lambda_1\lambda_2\lambda_3} \int_{-\infty}^{\infty} df_A\, df_B\, df_3\, \delta(f_3 + f_A + f_B)\, \delta_T(f_3 + f_A + f_B)\,, \\ &\quad \tilde{Q}(f_A)\,\tilde{Q}(f_B)\, B^{\lambda_1\lambda_2\lambda_3}(f_A, f_B, \hat{n}_\star)\, \mathcal{R}^{\lambda_1\lambda_2\lambda_3}_{\alpha\beta\gamma}(\hat{n}_\star)\,, \end{aligned} \tag{4.4.5}$$

$$\begin{aligned} &= T \sum_{\lambda_1\lambda_2\lambda_3} \int_{-\infty}^{\infty} df_A\, df_B\,, \tilde{Q}(f_A)\,\tilde{Q}(f_B) \\ &\times \quad B^{\lambda_1\lambda_2\lambda_3}(f_A, f_B, \hat{n}_\star)\, \mathcal{R}^{\lambda_1\lambda_2\lambda_3}_{\alpha\beta\gamma}(\hat{n}_\star)\,, \end{aligned} \tag{4.4.6}$$

where we use the fact that $\delta_T(0) = T$, and make use of expression (4.2.14) for the GW three point function in momentum space.

The noise N. We assume that the noise is Gaussian and uncorrelated between pulsars; we define the noise spectrum as

$$\langle n_\alpha(f_A) n^*_\alpha(f_C)\rangle = S_n\, \delta(f_A - f_C)\,, \tag{4.4.7}$$

where we use the fact that PTA noise is frequency independent. We make use of the following formula from [277]:

$$S_n = 2\Delta t\, \sigma^2\,, \tag{4.4.8}$$

with $1/\Delta t$ the measurement cadence (of order 20 yr^{-1}), and σ^2 the *rms* of the noise timing (for IPTA pulsars, this quantity is of order 1 μs). The noise squared of the measurement, in absence of signal, is

$$\begin{aligned} N^2 &= \langle \mathcal{Y}\mathcal{Y}^*\rangle\,, && (4.4.9)\\ &= \int df_A\, df_B\, df_3\, df_C\, df_D\, df_4\; \delta_T(f_3 + f_A + f_B)\, \delta_T(f_4 + f_C + f_D) \\ &\quad \times \langle n_\alpha(f_A) n^*_\alpha(f_C)\rangle \langle n_\beta(f_B) n^*_\beta(f_D)\rangle \langle n_\gamma(f_3) n^*_\gamma(f_4)\rangle \\ &\quad \times Q(f_A) Q^*(f_C) Q(f_B) Q^*(f_D)\,, && (4.4.10)\\ &= T\, S_n^3 \int df_A\, df_B\, |Q(f_A)|^2\, |Q(f_B)|^2\,. && (4.4.11) \end{aligned}$$

Then the ratio corresponding to signal-to-noise is the ratio of the quantity S in eq (4.4.6) versus N of eq (4.4.11). We can sum over all the available distinct pulsar triplets (α, β, γ) in the network under consideration [7]. We

[7] Instead of correlating signals from three different pulsars, we can also correlate two signals from the same pulsar with a signal from a different pulsar, as described in Section 4.3. In this case, we need to sum over distinct pulsar pairs, instead of triplets (more on this later).

find

$$\begin{aligned}\text{SNR} \;&=\; \sqrt{T}\frac{1}{\left[\, S_n^3 \int df_A\, df_B\, |Q(f_A)|^2\, |Q(f_B)|^2 \,\right]^{1/2}} \\ &\times\Bigg[\sum_{\alpha\beta\gamma} \sum_{\lambda_i} \int_{-\infty}^{\infty} df_A\, df_B\; \tilde{Q}(f_A)\, \tilde{Q}(f_B) \\ &\Big(B^{\lambda_1\lambda_2\lambda_3}(f_A, f_B, \hat{n}_\star)\, \mathcal{R}^{\lambda_1\lambda_2\lambda_3}_{\alpha\beta\gamma}(\hat{n}_\star)\Big)\Bigg] \end{aligned} \tag{4.4.12}$$

In order to determine the function Q maximising the previous expression, we first define a positive definite scalar product $[\cdots,\cdots]$ between two quantities which depend on frequency (recall that S_n is a positive quantity):

$$[A_1(f_a, f_b),\, A_1(f_a, f_b)] \;=\; \int df_a\, df_b\; A_1(f_a, f_b)\, A_2^*(f_a, f_b)\, S_n^3\,. \tag{4.4.13}$$

By dropping indexes, the SNR of eq (4.4.12) can be then schematically re-expressed in terms of this scalar product as

$$\text{SNR} \;=\; \sqrt{T}\, \frac{[QQ,\, B\,\mathcal{R}/S_n^3]}{[QQ,\, QQ]^{1/2}}\,. \tag{4.4.14}$$

The previous quantity is maximized by choosing the function Q as

$$Q(f_a)Q(f_b) \;=\; \frac{B(f_a, f_b, n^*)\, \mathcal{R}(n^*)}{S_n^3}\,. \tag{4.4.15}$$

To summarize, the optimal SNR is given by the expression

$$\text{SNR}_{\text{opt}} \;=\; \sqrt{4\,T}\left[\sum_{\lambda_1\lambda_2\lambda_3} \frac{\int_0^\infty df_A\, df_B\, (\mathtt{r}^{\lambda_1\lambda_2\lambda_3}\, B^{\lambda_1\lambda_2\lambda_3}(f_A, f_B, \hat{n}_\star)\,)^2}{S_n^3} \right]^{\frac{1}{2}}, \tag{4.4.16}$$

where we find convenient to define a single quantity $\mathtt{r}^{\lambda_1\lambda_2\lambda_3}$ containing the sum of the PTA response functions over all independent pulsar triplets:

$$\mathtt{r}^{\lambda_1\lambda_2\lambda_3} \;=\; \left[\sum_{\alpha\beta\gamma} \left(\mathcal{R}^{\lambda_1\lambda_2\lambda_3}_{\alpha\beta\gamma}(\hat{n}_\star)\right)^2 \right]^{\frac{1}{2}}. \tag{4.4.17}$$

	Case 1	Case 2
$\mathtt{r}^{RRR}$	20.17	0.58
$\mathtt{r}^{RRL}$	19.58	0.99
$\mathtt{r}^{RLR}$	19.58	0.99
$\mathtt{r}^{STT}$	38.11	0.28
$\mathtt{r}^{SST}$	119.49	1.96
$\mathtt{r}^{SSS}$	168.99	9.12

TABLE 4.1: *Value of the quantity $\mathtt{r}^{\lambda_1\lambda_2\lambda_3}$ for different GW tensor polarizations, computed for two different cases using IPTA data. Case 1: we do the sum of eq (4.4.17) summing over distinct pulsar triplets. Case 2: the sum is made assuming that we correlate two signals from one pulsar with one signal from another pulsar (as in Section 4.3.2.1) hence we sum over distinct couples of pulsars. We consider purely tensor correlators (depending on chirality, upper part of the table) and scalar-tensor correlators (lower part of the table).*

Hence we learn that the optimal SNR, besides than on the frequency dependence of the bispectrum, is characterized by the constant quantity $\mathtt{r}^{\lambda_1\lambda_2\lambda_3}$ of eq. (4.4.17). This depends on the GW polarization, and on the number and position of the pulsars one considers. We compute this quantity for the case of IPTA pulsars – an international collaboration monitoring the period of 49 pulsars from different PTA data set, see Appendix C.2 – in Table 4.1. Summing over distinct triplets of pulsars (Case 1) give much larger values for the parameter $r^{\lambda_1\lambda_2\lambda_3}$, than summing over couples (Case 2): we believe that this is due to the large number of independent triples one can form with the large pulsar data set we use. Also, both for Case 1 and 2, the size of this parameter is much larger in the case of correlations involving scalar modes only, since the corresponding overlap function is one order of magnitude larger than in the case of tensor correlators, see Section 4.3.

Our conclusion is that the optimal SNR for measuring stationary graviton non-Gaussianity can be greatly enhanced by monitoring larger numbers of pulsars, since it depends on number and configurations of pulsar triplets. It will be interesting to build explicit models leading to stationary tensor nG, and investigate at what extent we can probe amplitude and slope

(i.e. frequency dependence) of a stationary tensor bispectrum with current (IPTA) and future (SKA) PTA experiments. We leave these investigations to future work. SKA is expected to observe all the pulsars in the galaxy (up to 30,000) [278] and a few thousand will be millisecond pulsars [279] thereby in increasing the number available to improve the signal to noise ratio.

4.5 Conclusions

In this work we introduced the concept of stationary graviton non-Gaussianity (nG). We discussed how its properties make it the only type of graviton nG that can be directly measurable in terms of three-point functions of a stochastic gravitational wave background (SGWB). When evaluated in Fourier space, 3-point functions associated with stationary nG correspond to configurations peaked in folded configurations. We determined 3-point overlap functions for probing stationary nG with PTA experiments, and we obtained the corresponding optimal signal-to-noise ratio (SNR). For the first time, we considered 3-point overlap functions for PTA including scalar graviton polarizations (which can be motivated in theories of modified gravity); moreover, we also calculated 3-point overlap functions for correlating PTA with ground based GW interferometers. We have shown that the value of the optimal SNR depends on the number and position of monitored pulsars. We built geometrical quantities characterizing how the SNR depends on the PTA system under consideration, and we evaluated such geometrical parameters using data from the IPTA collaboration. We shown that monitoring a large number of pulsars can increase the SNR associated with measurements of stationary graviton nG.

If in the future a SGWB will be detected with PTA GW experiments, it will be interesting to try to measure the corresponding signal 3-point function with the tools we developed here. If data will provide evidence for

stationary nG, a challenge for theorists will be to design and characterize early universe scenarios (possibly using approaches based on the effective field theory of inflation) able to realize folded configurations for graviton nG in momentum space.

Chapter 5

Conclusions

In Chapter 1 we discussed one of the biggest mysteries of the Universe, Dark Matter. The possible candidates were mentioned focusing specifically on the axion and how it is more suitable than other particles such as WIMPS. The detection methods for this pseudoscalar, both direct and indirect, were discussed and how axions have the potential to produce gravitational waves (indirect detection of axions). Following on from this, we then explored inflation and how a particular model is able to amplify and enhance primordial gravitational waves from the early universe which can then be detected by various detectors such LIGO, LISA, SKA etc.

In Chapter 2 we aimed to create a multi field system of ultra-light scalar fields which could increase the mass range of the cosmological axion into the observation range of current pulsar timing arrays. Beginning with the uncoupled system, the highest characteristic strain that could be achieved was identical to the single field case form the paper we based this work was based on [95]. We then attempted a system where we coupled our dark matter to dark energy, however, we were unable to produce an expression for the pressure perturbations (from the energy momentum tensor) which was much smaller than the energy density of the system. So, the system was not pressureless and therefore no longer a dark matter candidate. In future

work, another coupled system could be devised which could, potentially, improve the mass range of the axion.

In Chapter 3 we investigated the consequences of a non-attractor phase of cosmological evolution for the dynamics of primordial tensor modes, focusing on the properties of primordial tensor non-Gaussianity in scenarios with non-minimal couplings of gravity to the scalar sector. Squeezed tensor non-Gaussianity induces a characteristic quadrupolar anisotropy on the power spectrum of the stochastic background of primordial tensor perturbations. To align with gravitational wave experiments, we discussed the response function of a ground based Michelson interferometer to a gravitational wave background with such a feature. In future it would be interesting to apply our approach to more general scenarios. This would also allow one to study in more general terms the transition phase between attractor and non-attractor, and related possible instabilities associated with violations of energy conditions.

In Chapter 4 we determined 3-point overlap functions for probing stationary non-Gaussianities with PTA experiments and we obtained the corresponding optimal signal-to-noise ratio (SNR). For the first time, we considered 3-point overlap functions for PTA including scalar graviton polarizations; moreover, we also calculated 3-point overlap functions for correlating PTA with ground based GW interferometers. We have shown that the value of the optimal SNR depends on the number and position of monitored pulsars. We configured geometrical quantities characterizing how the SNR depends on the PTA system under consideration, and we evaluated such geometrical parameters using data from the IPTA collaboration. We have shown that monitoring a large number of pulsars can increase the SNR associated with measurements of stationary graviton nG. If, in the future, a stochastic gravitational wave background is detected with PTA GW experiments, it will be interesting to try to measure the corresponding signal 3-point function with the tools developed in this chapter.

Appendix A

Axions and Gravitational Waves

It has been suggested that axions, or in a more general sense, pseudoscalars could be detected through the use of pulsar timing arrays [95].The motivation for this detection method arose from observations of pulsars by telescopes (Pulsar Timing Arrays (PTAs)). They rotate with very precise periods of the order of milliseconds, however what the PTAs observe is a frequency shift when photons from the pulsars reach the detector. The question is what is the cause of this? The main suspect are gravitational waves. The entirety of spacetime is filled with background gravitational waves which are the product of two massive merging black holes. However, the suggestion made by Rubakov and Khmelnitsky [95] is that the gravitational oscillations that cause the frequency shift of the pulsar observations is in fact due to axions. They state that the axions (ultra-light non-interacting dark matter) behave as a perfect fluid with oscillating pressure, which averages to zero on the time scales which exceed the oscillation period, and is usually treated as a pressureless dust. However, what is not taken in to account is that as a consequence of these oscillations in pressure this causes oscillations in the gravitational potentials. These gravitational

potential oscillations could be observed which could result in the indirect detection of axions.

In their paper they show the pulsar timing signal for scalar field dark matter for a range of scalar masses.

Our aim is to prove that the gravitational oscillations are produced by pseudoscalars. These methods are collected in a review by Romano and Cornish [280].

First we must mention the polarisation mode for a gravitational wave (GW). The most that are allowed for a GW in a general metric gravity theory in four dimensions is 6 polarisation (two tensor, two vector and two scalar) [281]. [1]

$$
\begin{aligned}
e^{+}_{ab} &= \hat{l}_a\hat{l}_b - \hat{m}_a\hat{m}_b, & e^{\times}_{ab} &= \hat{l}_a\hat{m}_b + \hat{m}_a\hat{l}_b,\\
e^{X}_{ab} &= \hat{l}_a\hat{l}_b + \hat{m}_a\hat{m}_b, & e^{Y}_{ab} &= \hat{m}_a\hat{n}_b + \hat{n}_a\hat{m}_b,\\
e^{B}_{ab} &= \hat{l}_a\hat{l}_b + \hat{m}_a\hat{m}_b, & e^{L}_{ab} &= \sqrt{2}\hat{n}_a\hat{n}_b.
\end{aligned}
\tag{A.0.1}
$$

where e^{+}_{ab} is the tensor-plus mode, $e^{\times}_{ab}$ is the tensor-cross mode, e^{X}_{ab} is the vector-x mode, e^{Y}_{ab} is the vector-y mode, e^{B}_{ab} is the scalar breathing mode (or transverse massless mode) and e^{L}_{ab} is the scalar longitudinal mode.

$\hat{\mathbf{l}}$, $\hat{\mathbf{m}}$ and $\hat{\mathbf{n}}$ are unit vectors defined as:

$$
\begin{aligned}
\hat{\mathbf{n}} &= \sin\theta\cos\phi\,\hat{x} + \sin\theta\sin\phi\,\hat{y} + \cos\theta\,\hat{z},\\
\hat{\mathbf{l}} &= \cos\theta\cos\phi\,\hat{x} + \cos\theta\sin\phi\,\hat{y} - \sin\theta\,\hat{z},\\
\hat{\mathbf{m}} &= -\sin\phi\,\hat{x} + \cos\phi\,\hat{y}.
\end{aligned}
\tag{A.0.2}
$$

We then check through any possible combination of these unit vectors in order to find a combination which could be consider as a pseudoscalar. Unlike ordinary scalars who have a parity of +1 pseudoscalars have a parity of −1

[1] This is true for theories of modified gravity, in general relativity only predicts the two tensor modes.

when they undergo improper rotation. So how do we check if our proposed polarisation basis is a pseudoscalar? First, we must check if the above unit vectors change sign under improper rotation. The parity transformations for θ and ϕ are defined as:

$$\theta \to \pi - \theta, \qquad \phi \to \phi + \pi, \tag{A.0.3}$$

This changes the definitions of the unit vectors,

$$\begin{aligned} \hat{\mathbf{n}} &= -\sin\theta\cos\phi\,\hat{x} - \sin\theta\sin\phi\,\hat{y} - \cos\theta\,\hat{z}, \\ \hat{\mathbf{l}} &= \cos\theta\cos\phi\,\hat{x} + \cos\theta\sin\phi\,\hat{y} - \sin\theta\,\hat{z}, \\ \hat{\mathbf{m}} &= \sin\phi\,\hat{x} - \cos\phi\,\hat{y}. \end{aligned} \tag{A.0.4}$$

$\hat{\mathbf{m}}$ and $\hat{\mathbf{n}}$ change sign which narrows down the possibilities of either of these two combined with $\hat{\mathbf{l}}$. How do we know if a polarisation basis is a scalar? By performing a rotating the unit vectors around a new angle ψ.[2]

$$\begin{aligned} \hat{p} &\equiv \cos\psi\,\hat{\mathbf{l}} + \sin\psi\,\hat{\mathbf{m}}, \\ \hat{q} &\equiv -\sin\psi\,\hat{\mathbf{l}} + \cos\psi\,\hat{\mathbf{m}}. \end{aligned} \tag{A.0.5}$$

As an example we take the polarisation basis e^B_{ab} and perform a rotation on it and this produces the following transformation

$$e^B_{ab}(\hat{\mathbf{n}}, \psi) = e^B_{ab}(\hat{\mathbf{n}}). \tag{A.0.6}$$

After the rotation is performed the scalar polarisation basis remains the same, therefore our new basis must do the same.

Our new polarisation basis is defined as

$$e^{Ps}_{ab} = \hat{l_a}\,\hat{m}_b - \hat{m}_a\,\hat{l_b}. \tag{A.0.7}$$

[2] $\hat{\mathbf{n}}$ remains the same as $\hat{\mathbf{l}}$ and $\hat{\mathbf{m}}$ are perpendicular to it.

Since it is a combination of $\hat{\mathbf{l}}$ and $\hat{\mathbf{m}}$ its sign changes. Under a proper rotation to transforms as:

$$e_{ab}^{Ps}(\hat{\mathbf{n}}, \psi) = e_{ab}^{Ps}(\hat{\mathbf{n}}). \tag{A.0.8}$$

Not only is a scalar but it changes sign under parity transformation therefore it is a pseudoscalar.

Each of the polarisation basis are used to produce a response function from the chosen detector.

The pulsar timing array response function equation is defined as [280][3]:

$$R^A(f, \hat{\mathbf{n}}) = \frac{1}{2} \frac{\hat{\mathbf{u}}^a \hat{\mathbf{u}}^b}{1 - \hat{\mathbf{n}} \cdot \hat{\mathbf{u}}} e_{ab}^A(\hat{\mathbf{n}}) \left[1 - e^{-\frac{i2\pi f L}{c}(1 - \hat{\mathbf{n}} \cdot \hat{\mathbf{u}})}\right], \tag{A.0.9}$$

where $A = \{\times, +, X, Y, B, L, Ps\}$.

A detector response function can be produced for each of the polarisation basis, including the one for our new pseudoscalar, Ps.

$$\begin{aligned}
R^+(f, \hat{\mathbf{n}}) &= \frac{1}{2}(1 + \cos\theta)\left[1 - e^{-\frac{i2\pi f L}{c}(1 - \cos\theta)}\right], \\
R^\times(f, \hat{\mathbf{n}}) &= 0, \\
R^X(f, \hat{\mathbf{n}}) &= -\frac{\sin\theta\cos\theta}{1 - \cos\theta}\left[1 - e^{-\frac{i2\pi f L}{c}(1 - \cos\theta)}\right], \\
R^Y(f, \hat{\mathbf{n}}) &= 0, \\
R^B(f, \hat{\mathbf{n}}) &= \frac{1}{2}(1 + \cos\theta)\left[1 - e^{-\frac{i2\pi f L}{c}(1 - \cos\theta)}\right], \\
R^L(f, \hat{\mathbf{n}}) &= \frac{1}{\sqrt{2}}\frac{\cos^2\theta}{1 - \cos\theta}\left[1 - e^{-\frac{i2\pi f L}{c}(1 - \cos\theta)}\right], \\
R^{Ps}(f, \hat{\mathbf{n}}) &= 0.
\end{aligned} \tag{A.0.10}$$

Unfortunately the response function for the pseudoscalar is zero which leads us to the conclusion that pseudoscalars cannot be detected with pulsar timing arrays despite the proposals put forward by Rubakov in [95].

[3] the detector response function is how the detector responds in the presence of a polarisation mode.

The next step is to check whether the pseudoscalar can be detected for ground-based interferometers. Their detector response function is defined as:

$$R^A(f,\hat{\mathbf{n}}) \simeq \frac{1}{2}(u^a u^b - v^a v^b)\, e^A_{ab}(\hat{\mathbf{n}}), \tag{A.0.11}$$

where $\hat{\mathbf{u}}$ and $\hat{\mathbf{v}}$ are unit vectors that are pointing in the direction of the arms of the interferometer [280].

From this we are able to find the solutions for the interferometer response functions.

$$R^+(\hat{\mathbf{n}}) = \frac{1}{2}(1+\cos\theta), \qquad R^\times(\hat{\mathbf{n}}) = -\cos\theta\sin 2\phi,$$
$$R^X(\hat{\mathbf{n}}) = \sin\theta\cos\theta\cos 2\phi, \qquad R^Y(\hat{\mathbf{n}}) = -\sin\theta\sin 2\phi,$$
$$R^B(\hat{\mathbf{n}}) = -\frac{1}{2}\sin^2\theta\cos 2\phi, \qquad R^L(\hat{\mathbf{n}}) = \frac{1}{\sqrt{2}}\sin^2\theta\cos 2\phi,$$
$$R^{Ps}(\hat{\mathbf{n}}) = 0.$$

It seems that pseudoscalars cannot to be detected using ground-based interferometers either; as its response function is zero for this case as well.

Is there a geometry for a detector which allows us to produce a non-zero response function for the pseudoscalar mode? The space-based interferometer LISA (due to be launched in the 2030s) could the configuration for the detection of axions or creating another ground-based interferometer which are modified to detect axions, axion interferometers. Both of which are discused in the first chapter.

A.1 Pseudovector

While searching for a pseudoscalar polarisation basis we discovered a pseudovector basis as well. A pseudovector (similar to the pseudoscalar) has parity of -1 when it undergoes an improper rotation. To prove it is also a vector it must transform as below when performing a proper rotation

(using the rotated unit vectors from (A.0.5))

$$e^X(\hat{\mathbf{n}},\psi) = \cos\psi\, e^X_{ab}(\hat{\mathbf{n}}) + \sin\psi\, e^Y_{ab}(\hat{\mathbf{n}}),$$
$$e^Y(\hat{\mathbf{n}},\psi) = -\sin\psi\, e^X_{ab}(\hat{\mathbf{n}}) + \cos\psi\, e^Y_{ab}(\hat{\mathbf{n}}). \tag{A.1.1}$$

The polarisation basis for a vector but with parity of −1 after an improper rotation is performed upon is the following:

$$e^{Pv}_{ab} = \hat{l}_a\,\hat{n}_b - \hat{n}_a\,\hat{l}_b. \tag{A.1.2}$$

It is a vector since it transforms as below after proper rotation:

$$e^{Pv}(\hat{\mathbf{n}},\psi) = \cos\psi\, e^Z_{ab}(\hat{\mathbf{n}}) + \sin\psi\, e^{Pv}_{ab}(\hat{\mathbf{n}}), \tag{A.1.3}$$

where $e^Z_{ab}(\hat{\mathbf{n}})$ is the polarisation basis of another vector combination found during the process of searching for the pseudoscalar. It has this form [4]

$$e^Z_{ab} = \hat{m}_a\,\hat{n}_b - \hat{n}_a\,\hat{m}_b. \tag{A.1.4}$$

$e^{Pv}_{ab}(\hat{\mathbf{n}})$ is a pseudovector as it changes sign under parity transformation.

Like the pseudoscalar the detector response functions for the pseudovector basis cannot be calculated. This is because the polarisation mode gives us a zero-response function. Therefore the pseudovector also has a zero response function for interferometers. [5] The response functions for the extra vector mode was also calculated but it yielded a zero response function for both types of detectors, so only the other two vector modes can be detected.

[4] $e^Z_{ab}(\hat{\mathbf{n}})$ does not change sign under parity transformation therefore it is an ordinary vector.

[5] That when two different unit vector are multiplied by each other and then subtracted from each other you will not be able to produce a non-zero response function.

A.2 Modes with one index and no indices

In the introductory part we had been using the conventions from [280]. From now on we will be using the conventions from [282]

Now that we have produced expressions for pseudoscalar and pseudovector modes with two indices (gravitational waves are spin-2 therefore they require two indices) we wish to repeat the same process for modes with one index and following that we move on to where there are no indices and produce Hellings and Downs curves for pseudovectors and pseudoscalars in these cases as we were unable to produce non-zero response functions in the cases involving two indices.

We list the modes with one index as follows:

$$\begin{aligned} e_a^V &= \hat{l}_a, \\ e_a^{Pv} &= \hat{m}_a, \\ e_a^{PSc} &= \hat{n}_a. \end{aligned} \tag{A.2.1}$$

where,

$$\begin{aligned} \hat{\mathbf{n}} &= -\sin\theta\cos\phi\,\hat{x} - \sin\theta\sin\phi\,\hat{y} - \cos\theta\,\hat{z}, \\ \hat{\mathbf{l}} &= \cos\theta\cos\phi\,\hat{x} + \cos\theta\sin\phi\,\hat{y} - \sin\theta\,\hat{z}, \\ \hat{\mathbf{m}} &= -\sin\phi\,\hat{x} + \cos\phi\,\hat{y}. \end{aligned} \tag{A.2.2}$$

We have found a vector, pseudovector and a scalar mode. From this we can produce the response functions for these modes in the direction of a pulsar, $\hat{\mathbf{u}}_1$. Using the following formula:

$$F_1^{\alpha}(\hat{\mathbf{k}}) \equiv \frac{1}{2}\left(\frac{\hat{\mathbf{u}}_1}{1+\hat{\mathbf{k}}\cdot\hat{\mathbf{u}}_1}\right) : e_{\alpha}(\hat{\mathbf{k}})\left[1 - e^{-\frac{i2\pi fL}{c}(1+\cos\theta)}\right], \tag{A.2.3}$$

where, $\hat{\mathbf{k}}$ is a unit vector which is pointing in $-\hat{\mathbf{n}}$ direction.

$$\begin{aligned} F_a^V(\hat{\mathbf{k}}) &= \frac{1}{2}\frac{-\sin\theta}{1+\cos\theta}\left[1-e^{-\frac{i2\pi fL}{c}(1+\cos\theta)}\right], \\ F_a^{Pv}(\hat{\mathbf{k}}) &= 0, \\ F_a^{PSc}(\hat{\mathbf{k}}) &= \frac{1}{2}\frac{-\cos\theta}{1+\cos\theta}\left[1-e^{-\frac{i2\pi fL}{c}(1+\cos\theta)}\right]. \end{aligned} \tag{A.2.4}$$

The case where there are no indices (scalar mode), which we call ϕ, the response function is given as

$$F_1^{\alpha}(\hat{\mathbf{k}}) \equiv \frac{1}{2}\left(\frac{\hat{\mathbf{u}}_1}{1+\hat{\mathbf{k}}\cdot\hat{\mathbf{u}}_1}\right) : e_{\alpha}(\hat{\mathbf{k}})\left[1-e^{-\frac{i2\pi fL}{c}(1+\cos\theta)}\right].$$

where,

$$F^{\phi}(\hat{\mathbf{k}}) = \frac{1}{2(1+\cos\theta)}\left[1-e^{-\frac{i2\pi fL}{c}(1+\cos\theta)}\right]. \tag{A.2.5}$$

Response functions were also found for ground-based interferometers for the one and zero indices modes.

$$F^A(\hat{\mathbf{k}}) \simeq \frac{1}{2}(u^a - v^a)\, e_a^A(\hat{\mathbf{k}}) \tag{A.2.6}$$

One index:

$$F_a^V(\hat{\mathbf{k}}) = -\cos\phi - \frac{1}{2}\sin\phi, \tag{A.2.7}$$

$$F_a^{Pv}(\hat{\mathbf{k}}) = \frac{1}{2}\cos\theta\cos\phi - \cos\theta\sin\phi, \tag{A.2.8}$$

$$F_a^{PSc}(\hat{\mathbf{k}}) = \frac{1}{2}\cos\phi\sin\theta - \sin\theta\sin\phi. \tag{A.2.9}$$

Zero indices:

$$F^A(\hat{\mathbf{k}}) \simeq \frac{1}{2}\, e_a^A(\hat{\mathbf{k}}), F^{\phi}(\hat{\mathbf{k}}) = \frac{1}{2}. \tag{A.2.10}$$

The vector mode F_a^{Pv} gives a zero result because the unit vector m does not have a z-component. As we have been able to produce two non-zero response functions (one index and zero indices) we can now produces Hellings and Downs curves for them.

Since a none-zero response function was produced for the one index vector mode its overlap function can be calculated and from that its Hellings and Downs [260] curve can be plotted. Stochastic gravitational-wave backgrounds manifests itself as a non-vanishing correlation between the data taken by two or more detectors. This correlation differs, in general, from that due to instrumental noise, allowing us to distinguish between a stochastic gravitational-wave signal and other noise sources [280].

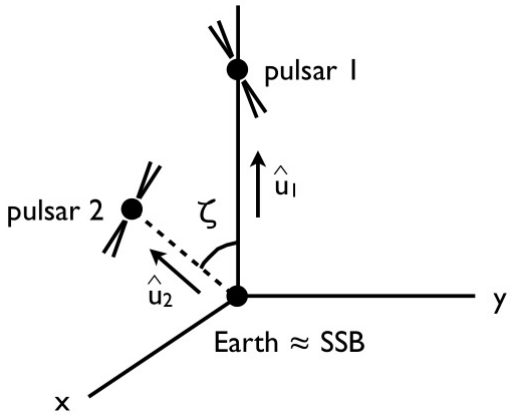

FIGURE A.1: Geometry for the calculation of the Hellings and Downs function for the correlated response of a pair of Earth-pulsar baselines to an isotropic, unpolarized stochastic gravitational-wave background [282]. The Earth is taken to be at the Solar System barycentre (SSB).

From the above figure we get the coordinates for each pulsar 1 and 2 respectively, $\hat{\mathbf{u}}_1 = \hat{\mathbf{z}}$ and $\hat{\mathbf{u}}_2 = \sin(\zeta)\hat{\mathbf{x}} + \cos(\zeta)\hat{\mathbf{z}}$.

The overlap function of the polarisation modes is defined as:

$$\Gamma_{ij}(f) = \frac{1}{(2\pi f)^2}\frac{1}{3}\chi(\zeta_{ij}), \tag{A.2.11}$$

where $\chi(\zeta_{ij})$ is the Hellings and Downs function and ζ is the angle of separation between pulsars [280].

$$\chi(\zeta) = \frac{1}{8\pi}\int_{S^2} d^2\Omega_{\hat{\mathbf{k}}} \sum_{\alpha} \frac{1}{2}\left(\frac{\hat{\mathbf{u}}_1}{1+\hat{\mathbf{k}}\cdot\hat{\mathbf{u}}_1}\right) : e_\alpha(\hat{\mathbf{k}})\ \frac{1}{2}\left(\frac{\hat{\mathbf{u}}_2}{1+\hat{\mathbf{k}}\cdot\hat{\mathbf{u}}_2}\right) : e_\alpha(\hat{\mathbf{k}}) \tag{A.2.12}$$

where α represents the polarisation mode which is being used. We should mention that $\hat{\mathbf{k}}$ is in the direction $-\hat{\mathbf{n}}$. **:** symbol denotes a contraction between tensors [281] .

We aim to calculate the Hellings and Downs functions for the one index modes starting with e_a^V. First we must provide a few definitions. From (A.2.12):

$$\begin{aligned}
\hat{\mathbf{k}} \cdot \hat{\mathbf{u}}_1 &= \cos\theta, \\
\hat{\mathbf{k}} \cdot \hat{\mathbf{u}}_2 &= \sin\zeta \sin\theta \cos\phi + \cos\zeta \cos\theta, \\
\hat{\mathbf{u}}_1 : e^V &= -\sin\theta, \\
\hat{\mathbf{u}}_2 : e^V &= \sin\zeta \cos\theta \cos\phi - \cos\zeta \sin\theta.
\end{aligned} \tag{A.2.13}$$

Now we are able to put these definitions back in to (A.2.12) which we then simplify.

$$\begin{aligned}
F_1^\alpha(\hat{\mathbf{k}}) &\equiv \frac{1}{2}\left(\frac{\hat{\mathbf{u}}_1}{1+\hat{\mathbf{k}}\cdot\hat{\mathbf{u}}_1}\right) : e_\alpha(\hat{\mathbf{k}}), \\
F_2^\alpha(\hat{\mathbf{k}}) &\equiv \frac{1}{2}\left(\frac{\hat{\mathbf{u}}_2}{1+\hat{\mathbf{k}}\cdot\hat{\mathbf{u}}_2}\right) : e_\alpha(\hat{\mathbf{k}}).
\end{aligned} \tag{A.2.14}$$

This allows us to go about solving the Hellings and Downs function.

$$\begin{aligned}
F_1^V(\hat{\mathbf{k}}) &= -\frac{1}{2}\frac{\sin\theta}{1+\cos\theta}, \\
F_2^V(\hat{\mathbf{k}}) &= \frac{1}{2}\frac{\sin\zeta\cos\theta\cos\phi - \cos\zeta\sin\theta}{1+\sin\zeta\sin\theta\cos\phi+\cos\zeta\cos\theta},
\end{aligned} \tag{A.2.15}$$

where $F_1^V(\hat{\mathbf{k}})$ is the response function for the pseudovector mode in the direction of the pulsar in $\hat{\mathbf{u}}_1$ from (A.2.7). $F_2^V(\hat{\mathbf{k}})$ is the response function in the direction $\hat{\mathbf{u}}_2$.

With our expressions for the response functions complete we can re-write the integral (A.2.12) as:

$$\chi(\zeta) = \frac{1}{8\pi}\int_{S^2} d^2\Omega_{\hat{\mathbf{k}}}\, F_1^V(\hat{\mathbf{k}})\, F_2^V(\hat{\mathbf{k}}) = \frac{1}{16\pi}\int_{-1}^{1} dx\, \frac{-\sqrt{1-x^2}}{1-x}\, I^V(x,\zeta). \tag{A.2.16}$$

where $I^V(x,\zeta)$ is the integral of $F_2^V(\hat{\mathbf{k}})$ in terms of ϕ.

$$\begin{aligned} I^V(x,\zeta) &\equiv \int_0^{2\pi} d\phi\, F_2^V(\hat{\mathbf{k}}), \\ &= \frac{1}{2}\int_0^{2\pi} d\phi \left[\frac{\cos\theta\,\sin\zeta\,\cos\phi - \cos\zeta\,\sin\theta}{1+\sin\zeta\,\sin\theta\,\cos\phi + \cos\theta\,\cos\zeta}\right], \end{aligned} \tag{A.2.17}$$

We provide the following definition $x \equiv \cos\theta$ and substitute it into the expression (A.2.17).

$$\begin{aligned} I^V(x,\zeta) &\equiv \int_0^{2\pi} d\phi\, F_2^V(\hat{\mathbf{k}}), \\ &= \frac{1}{2}\int_0^{2\pi} d\phi \left[\frac{x\,\sin\zeta\,\cos\phi - \cos\zeta\,\sqrt{1-x^2}}{1+\sin\zeta\,\sqrt{1-x^2}\cos\phi + x\,\cos\zeta}\right]. \end{aligned} \tag{A.2.18}$$

Due to the presence of a ϕ term in the denominator we are unable to use standard integration methods. In this case we must use contour integration in order to compute $I(x,\zeta)$. Contour integration involves integrating around a contour in the complex plane and find the poles within that contour and calculating their residues.

Firstly, $I^V(x,\zeta)$ can be split in to two simpler integrals labelled as follows:

$$I_1^V(x,\zeta) = \int_0^{2\pi} d\phi \left[\frac{x\,\sin\zeta\,\cos\phi}{1+\sin\zeta\,\sqrt{1-x^2}\,\cos\phi + x\,\cos\zeta}\right], \tag{A.2.19}$$

$$I_2^V(x,\zeta) = \int_0^{2\pi} d\phi \left[\frac{-\cos\zeta\,\sqrt{1-x^2}}{1+\sin\zeta\,\sqrt{1-x^2}\,\cos\phi + x\,\cos\zeta}\right].$$

A substitution of variables is needed in order to perform the contour integration. We put the following definitions in to (A.2.19) $z = e^{i\phi}$ and

$cos\,\phi = \frac{1}{2}(z + z^{-1})$

$$I_1^V(x,\zeta) = x\,\sin\zeta \int_0^{2\pi} d\phi \left[\frac{\frac{e^{i\,\phi}+e^{-i\,\phi}}{2}}{1 + x\,\cos\zeta + \sqrt{1-x^2}\,\frac{e^{i\,\phi}+e^{-i\,\phi}}{2}\sin\zeta} \right], \quad \text{(A.2.20)}$$

$$I_2^V(x,\zeta) = -\cos\zeta\,\sqrt{1-x^2} \int_0^{2\pi} d\phi \left[\frac{1}{1 + x\,\cos\zeta + \sqrt{1-x^2}\,\frac{e^{i\,\phi}+e^{-i\,\phi}}{2}\sin\zeta} \right].$$

$e^{i\,\phi} = z$ and $e^{-i\,\phi} = \frac{1}{z}$ are then substituted in the equation (A.2.20).

$$I_1^V(x,\zeta) = x\,\sin\zeta \oint_C dz\,\frac{1}{i\,z} \left[\frac{(z+\frac{1}{z})}{2(1 + x\,\cos\zeta + \frac{1}{2}\sqrt{1-x^2}(z+\frac{1}{z})\sin\zeta)} \right], \quad \text{(A.2.21)}$$

$$I_2^V(x,\zeta) = -\cos\zeta\,\sqrt{1-x^2} \oint_C dz\,\frac{1}{i\,z} \left[\frac{1}{1 + x\,\cos\zeta + \frac{1}{2}\sqrt{1-x^2}(z+\frac{1}{z})\sin\zeta} \right].$$

$$I_1^V(x,\zeta) = x\,\sin\zeta \oint_C dz\,\frac{1}{i\,z} \left[\frac{(z^2+1)z}{2\,z(z(1 + x\,\cos\zeta) + \frac{1}{2}\sqrt{1-x^2}(z^2+1)\sin\zeta)} \right], \quad \text{(A.2.22)}$$

$$I_2^V(x,\zeta) = -\cos\zeta\,\sqrt{1-x^2} \oint_C dz\,\frac{1}{i\,z} \left[\frac{z}{z(1 + x\,\cos\zeta + \frac{1}{2}\sqrt{1-x^2}(z^2+1)\sin\zeta)} \right].$$

We then multiply (A.2.21) and (A.2.22) by $\frac{1}{i\,z}$

$$I_1^V(x,\zeta) = x\,\sin\zeta \oint_C dz \left[\frac{(z^2+1)}{2\,i\,z\,(z(1 + x\,\cos\zeta) + \frac{1}{2}\sqrt{1-x^2}(z^2+1)\sin\zeta)} \right], \quad \text{(A.2.23)}$$

$$I_2^V(x,\zeta) = -\cos\zeta\,\sqrt{1-x^2} \oint_C dz \left[\frac{1}{i(1 + x\,\cos\zeta + \frac{1}{2}\sqrt{1-x^2}(z^2+1)\sin\zeta)} \right].$$

Finally we multiply and divide by $-i$

$$I_1^V(x,\zeta) = x\,\sin\zeta \oint_C dz \left[\frac{-i(z^2+1)}{z\,(2\,z(1+x\,\cos\zeta)+\sqrt{1-x^2}(z^2+1)\sin\zeta)}\right], \tag{A.2.24}$$

$$I_2^V(x,\zeta) = -\cos\zeta\sqrt{1-x^2}\oint_C dz \left[\frac{-i}{z(1+x\,\cos\zeta)+\frac{1}{2}\sqrt{1-x^2}(z^2+1)\sin\zeta}\right].$$

Which leaves us with the following expression

$$\begin{aligned} I_1^V(x,\zeta) &= x\,\sin\zeta \oint_C dz\, f_1(z), \\ I_2^V(x,\zeta) &= -\cos\zeta\sqrt{1-x^2}\oint_C dz\, f_2(z). \end{aligned} \tag{A.2.25}$$

where,

$$\begin{aligned} f_1(z) &= \frac{-i\,(z^2+1)}{z\left[2z(1+x\,\cos\zeta)+\sqrt{1-x^2}\,\sin\zeta(z^2+1)\right]}, \\ f_2(z) &= \frac{-i}{\left[z(1+x\,\cos\zeta)+\frac{1}{2}\sqrt{1-x^2}\,\sin\zeta(z^2+1)\right]}. \end{aligned} \tag{A.2.26}$$

and C is the unit circle in the complex z-plane. The denominator of $f_1(z)$ and $f_2(z)$ can be factored using the quadratic formula for the expression in the square brackets [282].

For $f_1(z)$

$$\begin{aligned} &2z(1+x\,\cos\zeta)+\sqrt{1-x^2}\,\sin\zeta\,(z^2+1) \\ &\qquad = \sqrt{1-x^2}\,\sin\zeta\,(z-z_+)(z-z_-), \end{aligned} \tag{A.2.27}$$

and $f_2(z)$

$$\begin{aligned} &z(1+x\,\cos\zeta)+\frac{1}{2}\sqrt{1-x^2}\,\sin\zeta\,(z^2+1) \\ &\qquad = \frac{1}{2}\sqrt{1-x^2}\,\sin\zeta\,(z-z_+)(z-z_-). \end{aligned} \tag{A.2.28}$$

where,

$$z_+ = -\sqrt{\left(\frac{1 \pm \cos\zeta}{1 \mp \cos\zeta}\right)\left(\frac{1 \mp x}{1 \pm x}\right)}, \qquad z_- = \frac{1}{z_+}. \tag{A.2.29}$$

We are able to compute the integrals (A.2) by using the residue theorem which we define as

$$\oint_C f(z)dz = 2\,\pi\,i \sum_i \mathrm{Res}\,(f, z_i). \tag{A.2.30}$$

First we calculate the residues of $f_1(z)$

$$\mathrm{Res}(f_1, z_+) = \lim_{z\to z_+} (z - z_+) f(z) = \frac{-i\,(z^2+1)}{\sqrt{1-x^2}\,\sin\zeta\,(z^2+1)}\,(z - z_+), \tag{A.2.31}$$

$$\mathrm{Res}(f_1, 0) = \lim_{z\to 0} (z\,f(z)) = \frac{-i(z^2+1)}{\sqrt{1-x^2}\sin\zeta(z^2+1)}z. \tag{A.2.32}$$

Within the contour we have found two poles for f_1 in the complex plane, one at $z- > 0$ and the other at $z- > z_+$

We are able to expand out the term (z^2+1)

$$\mathrm{Res}(f_1, z_+) = \lim_{z\to z_+} (z - z_+) f(z) = \frac{-i\,(z^2+1)}{\sqrt{1-x^2}\,\sin\zeta\,(z - z_+)(z - z_-)}\,(z - z_+), \tag{A.2.33}$$

$$\mathrm{Res}(f_1, 0) = \lim_{z\to 0} (zf(z)) = \frac{-i(z_+^2+1)}{\sqrt{1-x^2}\sin\zeta(z - z_+)(z - z_-)}z. \tag{A.2.34}$$

Now we take in to account the limits that we set for each pole within the contour.

$$\mathrm{Res}(f_1, z_+) = \lim_{z\to z_+} (z - z_+) f(z) = \frac{-i\,(z_+^2+1)}{\sqrt{1-x^2}\,\sin\zeta\,(z_+ - z_+)(z_+ - z_-)}\,(z_+ - z_+), \tag{A.2.35}$$

$$\mathrm{Res}(f_1, 0) = \lim_{z\to 0} (zf(z)) = \frac{-i}{\sqrt{1-x^2}\sin\zeta(0 - z_+)(0 - z_-)}. \tag{A.2.36}$$

Which leaves us with final expressions for residues of $f_1(z)$

$$\mathrm{Res}(f_1, z_+) = \lim_{z\to z_+} (z - z_+) f(z) = \frac{-i(z_+^2 + 1)}{\sqrt{1-x^2}\,\sin\zeta\,(z_+ - z_-)}, \tag{A.2.37}$$

$$\mathrm{Res}(f_1, 0) = \lim_{z\to 0} (z f(z)) = \frac{-i}{\sqrt{1-x^2}\sin\zeta}. \tag{A.2.38}$$

Now we repeat the method in order to find residues of $f_2(z)$

$$\mathrm{Res}(f_2, z_+) = \lim_{z\to z_+} (z - z_+) f(z) = \frac{-i}{\frac{1}{2}\sqrt{1-x^2}\,\sin\zeta(z - z_+)(z - z_-)}\,(z - z_+). \tag{A.2.39}$$

Remember to take the limit in to account

$$\mathrm{Res}(f_2, z_+) = \lim_{z\to z_+} (z - z_+) f(z) = \frac{-i}{\frac{1}{2}\sqrt{1-x^2}\,\sin\zeta(z_+ - z_-)(z_+ - z_+)}\,(z_+ - z_+). \tag{A.2.40}$$

Which leaves us with the following residue for f_2

$$\mathrm{Res}(f_2, z_+) = \lim_{z\to z_+} (z - z_+) f(z) = \frac{-2\,i}{\sqrt{1-x^2}\,\sin\zeta(z_+ - z_-)} \tag{A.2.41}$$

$f_2(z)$ only has one residual because it only has one pole inside the contour (z_+) and there is no pole at $z = 0$.

Now we take the sum of the residues, remembering the residue formula (A.2.30)

$$\oint_C f(z)\,dz = 2\,\pi\,i \sum_i \mathrm{Res}\,(f, z_i).$$

First we take the sum of the residues of $f_1(z)$

$$\oint_C f_1(z)\,dz = 2\,\pi\,i \left(\frac{-i\,(z_+^2 + 1)}{\sqrt{1-x^2}\,\sin\zeta(z_+ - z_-)} + \frac{-i}{\sqrt{1-x^2}\sin\zeta} \right), \tag{A.2.42}$$

which simplifies to

$$\oint_C f_1(z)\,dz = \frac{2\,\pi}{\sqrt{1-x^2}\,\sin\zeta} \left(\frac{z_+^2 + 1}{z_+ - z_-} \right), \tag{A.2.43}$$

We can then reintroduce this in to the expression for I_1^V

$$I_1^V(x,\zeta) = x\,\sin\zeta \oint_C dz\, f_1(z), I_1^V(x,\zeta) = \frac{2\,\pi\,x}{\sqrt{1-x^2}}\left(\frac{z_+^2+1}{z_+ - z_-}\right). \tag{A.2.44}$$

Then repeat the process for the two residues of $f_2(z)$

$$\begin{aligned}\oint_C f_2(z)\,dz =& 2\,\pi\,i\left(\frac{-2\,i}{\sqrt{1-x^2}\,\sin\zeta(z_+ - z_-)}\right),\\ \oint_C f_2(z)\,dz =& \frac{4\,\pi}{\sqrt{1-x^2}\,\sin\zeta}\left(\frac{1}{(z_+ - z_-)}\right),\end{aligned} \tag{A.2.45}$$

Reintroduce in to expression for I_2^V

$$\begin{aligned}I_2^V =& -\cos\zeta\sqrt{1-x^2}\frac{4\,\pi}{\sqrt{1-x^2}\,\sin\zeta}\left(\frac{1}{(z_+ - z_-)}\right),\\ I_2^V =& -\frac{4\,\pi}{\tan\zeta}\left(\frac{1}{(z_+ - z_-)}\right).\end{aligned} \tag{A.2.46}$$

We can now take the sum of $I_1^V(x,\zeta)$ and $I_2^V(x,\zeta)$ which will give us the final expression for the integral I^V

$$\begin{aligned}I^V(x,\zeta) =& \frac{1}{2}(I_1^V(x,\zeta) + I_2^V(x\,\zeta)),\\ I^V(x,\zeta) =& \frac{1}{2}\left(\frac{2\,\pi\,x}{\sqrt{1-x^2}}\left(\frac{z_+^2+1}{z_+ - z_-}\right) + \frac{-4\,\pi}{\tan\zeta}\left(\frac{1}{(z_+ - z_-)}\right)\right).\end{aligned} \tag{A.2.47}$$

Expand and simplify the expression which leaves us with

$$I^V(x,\zeta) = \frac{\pi}{(z_+ - z_-)}\left(\frac{x\,(z_+^2+1)}{\sqrt{1-x^2}} + \frac{-2}{\tan\zeta}\right). \tag{A.2.48}$$

Having solved the integral through contour integration we are now able to calculate the Hellings and Downs (A.2.16) function for our vector mode.

$$\begin{aligned}\chi(\zeta) =& \frac{1}{8\pi}\int_{S^2} d^2\Omega_{\hat{\mathbf{k}}}\, F_1^V(\hat{\mathbf{k}})\, F_2^V(\hat{\mathbf{k}}) = \frac{1}{16\pi}\int_{-1}^{1} dx\,\frac{-\sqrt{1-x^2}}{1+x}\, I^V(x,\zeta),\\ \chi(\zeta) =& \frac{1}{8\pi}\int_{S^2} d^2\Omega_{\hat{\mathbf{k}}}\, F_1^V(\hat{\mathbf{k}})\, F_2^V(\hat{\mathbf{k}})\\ =& \frac{1}{16\pi}\int_{-1}^{1} dx\,\frac{-\sqrt{1-x^2}}{1+x}\,\frac{2\,\pi}{(z_+ - z_-)}\left(\frac{x\,(z_+^2+1)}{\sqrt{1-x^2}} + \frac{-2}{\tan\zeta}\right),\end{aligned} \tag{A.2.49}$$

$$\chi(\zeta) = \frac{1}{8}\Big(-2 + \ln(4) - 2\ln(1-\cos\zeta)\Big). \tag{A.2.50}$$

A.2.50 is now plotted as shown below

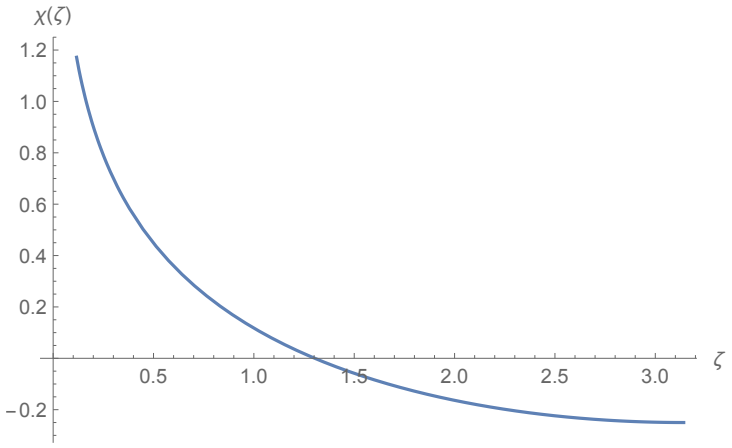

FIGURE A.2: Hellings and Downs Curve for one index vector mode.

As was stated previously, we are unable to produce the Hellings and Downs (HD) function for the pseudovector as it produces a zero response function for the pulsar in the direction $\hat{\mathbf{u}}_1$ because the unit vector $\hat{\mathbf{m}}$ does not have a **z**-component and $\hat{\mathbf{u}}_1$ is in the **z**-direction.

Now we move on to calculating the HD function for a pseudoscalar.

Starting from (A.2.12)

$$\chi(\zeta) = \frac{1}{8\pi}\int_{S^2} d^2\Omega_{\hat{\mathbf{k}}} \sum_{\alpha} \frac{1}{2}\left(\frac{\hat{\mathbf{u}}_1}{1+\hat{\mathbf{k}}\cdot\hat{\mathbf{u}}_1}\right) : e_\alpha(\hat{\mathbf{k}})\ \frac{1}{2}\left(\frac{\hat{\mathbf{u}}_2}{1+\hat{\mathbf{k}}\cdot\hat{\mathbf{u}}_2}\right) : e_\alpha(\hat{\mathbf{k}})$$

where we provide the coordinates of the system,

$$\begin{aligned}
&\hat{\mathbf{k}}\cdot\hat{\mathbf{u}}_1 = \cos\theta,\\
&\hat{\mathbf{k}}\cdot\hat{\mathbf{u}}_2 = \sin\zeta\sin\theta\cos\phi + \cos\zeta\cos\theta,\\
&\hat{\mathbf{u}}_1 : e^{PSc} = -\cos\theta,\\
&\hat{\mathbf{u}}_2 : e^{PSc} = -\sin\zeta\sin\theta\cos\phi - \cos\zeta\cos\theta.
\end{aligned} \tag{A.2.51}$$

We also simplify (A.2.12) by using the definitions from (A.2.14), where

$$F_1^{PSc} \equiv \frac{-\cos\theta}{2(1+\cos\theta)}\left[1 - e^{-\frac{i2\pi fL}{c}(1+\cos\theta)}\right], \tag{A.2.52}$$
$$F_2^{PSc} \equiv \frac{1}{2}\frac{-\sin\zeta\sin\theta\cos\phi - \cos\zeta\cos\theta}{1+\sin\zeta\sin\theta\cos\phi+\cos\zeta\cos\theta}\left[1 - e^{-\frac{i2\pi fL}{c}\left(1+\sin\zeta\,\sin\theta\,\cos\phi+\cos\zeta\cos\theta\right)}\right],$$

where $F_1^{PSc}(\hat{\mathbf{k}})$ is the response function for the pseudoscalar mode in the direction of the pulsar in $\hat{\mathbf{u}}_1$ from (A.2.7). $F_2^{PSc}(\hat{\mathbf{k}})$ is the response function in the direction $\hat{\mathbf{u}}_2$. Fron this we can re-write the integral (A.2.12) as:

$$\chi(\zeta) = \frac{1}{8\pi}\int_{S^2} d^2\Omega_{\hat{\mathbf{k}}}\, F_1^{PSc}(\hat{\mathbf{k}})\, F_2^{PSc}(\hat{\mathbf{k}}) = \frac{1}{16\pi}\int_{-1}^{1} dx\, \frac{-x}{1+x}\, I^{PSc}(x,\zeta). \tag{A.2.53}$$

where $x \equiv \cos\theta$. Unfortunately, unlike the vector mode the integral for the pseudoscalar does not converge. This is because the vector is transverse polarisation mode and the pseudoscalar is longitudinal. For this reason we included the pulsar terms (exponential terms. The term is known as the Earth term) for the response functions of the two pulsars in order to properly integrate the Hellings and Downs function. However, we now have to deal with both the real and imaginary parts of the function and if you look at the scalar longitudinal mode from the Romano and Cornish review [280] you will see that the function is barely above zero for both real and imaginary parts. So, it would require a lot of work in order for the pseudoscalar mode to converge. As a result we will try another configuration for the pseudoscalar mode which will converge when it is integrated.

A pseudoscalar is defined as the cross product of two vectors multiplied by a third. In orderd to get a new configuration we take our pseudoscalar from the previous case, $\hat{\mathbf{n}}$ and define the response functions as follows:

$$R_1^{Psc*} = \frac{1}{2}\frac{\hat{\mathbf{n}}\,(\hat{\mathbf{u}}_1 \times \hat{\mathbf{u}}_2)}{1+\hat{\mathbf{k}}\,\hat{\mathbf{u}}_1},$$
$$R_2^{Psc*} = \frac{1}{2}\frac{\hat{\mathbf{n}}\,(\hat{\mathbf{u}}_1 \times \hat{\mathbf{u}}_2)}{1+\hat{\mathbf{k}}\,\hat{\mathbf{u}}_2}. \tag{A.2.54}$$

Then we imposed our coordinate definitions on the response functions'

$$R_1^{Psc\star} = \frac{1}{2}\frac{-\sin\zeta\,\sin\theta\,\sin\phi}{1+\cos\theta},$$
$$R_2^{Psc\star} = \frac{1}{2}\frac{-\sin\zeta\,\sin\theta\,\sin\phi}{1+\sin\zeta\,\sin\theta\,\cos\phi+\cos\zeta\,\cos\theta}. \tag{A.2.55}$$

As we have previously defined $x \equiv \cos\theta$ we can therefore redefine any terms which include θ

$$R_1^{Psc\star} = \frac{1}{2}\frac{-\sin\zeta\,\sqrt{1-x^2}\,\sin\phi}{1+x},$$
$$R_2^{Psc\star} = \frac{1}{2}\frac{-\sin\zeta\,\sqrt{1-x^2}\,\sin\phi}{1+\sin\zeta\,\sqrt{1-x^2}\,\cos\phi+\cos\zeta\,x}. \tag{A.2.56}$$

The product of $R_1^{Psc\star}$ and $R_2^{Psc\star}$ is taken

$$R_1R_2 = \frac{1}{2}\frac{\sin^2\zeta\,(1-x^2)\,\sin^2\phi}{(1+x)\,(1+\sin\zeta\,\sqrt{1-x^2}\,\cos\phi+\cos\zeta\,x)},$$
$$R_1R_2 = \frac{1}{2}\frac{\sin^2\zeta\,(1-x)\,\sin^2\phi}{1+\sin\zeta\,\sqrt{1-x^2}\,\cos\phi+\cos\zeta\,x}. \tag{A.2.57}$$

This is now a suitable expression to begin the process of contour integrating R_1R_2. We begin by applying a change of variables.

$$I^{Psc\star} = \sin^2\zeta\,\int_0^{2\pi} d\phi\,\frac{(1-x)\,\sin^2\phi}{2(1+\sin\zeta\sqrt{1-x^2}\cos\phi+\cos\zeta x)} \tag{A.2.58}$$

where $I^{Psc\star}$ is the contour integral of R_1R_2 [6]

$$I^{Psc\star} = \sin^2\int_0^{2\pi} d\phi\frac{(1-x)\left(\frac{e^{-i\,\phi}-e^{i\,\phi}}{2\,i}\right)^2}{2\left(1+\sin\zeta\sqrt{1-x^2}\,\left(\frac{e^{i\,\phi}+e^{-i\,\phi}}{2}\right)+\cos\zeta\,x\right)} \tag{A.2.59}$$

$e^{i\,\phi} = z$ and $e^{-i\,\phi} = \frac{1}{z}$ are substituted in

$$I^{Psc\star} = \sin^2\zeta\,\oint_C dz\,\frac{1}{i\,z}\frac{(1-x)\,\left(\frac{\frac{1}{z}-z}{2i}\right)^2}{2\left(1+\sin\zeta\sqrt{1-x^2}\left(\frac{z+\frac{1}{z}}{2}\right)+\cos\zeta x\right)},$$

[6] $\sin^2\theta = \left(\frac{e^{-i\,\phi}-e^{i\,\phi}}{2\,i}\right)^2$ and $\cos\theta = \frac{e^{i\,\phi}+e^{-i\,\phi}}{2}$

$$I^{Psc*} = \sin^2\zeta \oint_C dz\, \frac{1}{i\,z}\, \frac{-(1-z^2)^2\,(1-x)}{2z\left(z\,(1+\cos\zeta\,x)+\frac{1}{2}\,\sin\zeta\sqrt{1-x^2}\,(z^2+1)\right)}, \tag{A.2.60}$$

Then the expression are multiplied by $\frac{1}{i\,z}$

$$I^{Psc*} = \sin^2\zeta \oint_C dz\, \frac{-(1-z^2)^2(1-x)}{2\,i\,z^2\left(z\,(1+\cos\zeta\,x)+\frac{1}{2}\sin\zeta\sqrt{1-x^2}\,(z^2+1)\right)}, \tag{A.2.61}$$

We can simplify by multiplying and dividing by $-i$

$$I^{Psc*} = \sin^2\zeta \oint_C dz\, \frac{i(1-z^2)^2\,(1-x)}{2\,z^2\left(z(1+\cos\zeta\,x)+\frac{1}{2}\,\sin\zeta\sqrt{1-x^2}\,(z^2+1)\right)}. \tag{A.2.62}$$

This leaves us with the following expression

$$I^{Psc*} = \sin^2\zeta \oint_C dz\, f^{PSc*}(z). \tag{A.2.63}$$

where,

$$f^{PSc*}(z) = \frac{i(1-z^2)^2}{z^2\left(2\,z(1+\cos\zeta)+\sin\zeta\sqrt{1-x^2}\,(z^2+1)\right)}. \tag{A.2.64}$$

C is the unit circle in the complex z-plane. The denominator of $f^{PSc*}(z)$ can be factorised using the quadratic formula for the expression in the square brackets [282]

$$\begin{aligned} & 2z(1+x\cos\zeta)+\sqrt{1-x^2}\sin\zeta\,(z^2+1) \\ = \;& \sqrt{1-x^2}\sin\zeta\,(z-z_+)\,(z-z_-). \end{aligned} \tag{A.2.65}$$

where,

$$z_+ = -\sqrt{\left(\frac{1\pm\cos\zeta}{1\mp\cos\zeta}\right)\left(\frac{1\mp x}{1\pm x}\right)}, \quad z_- = \frac{1}{z_+} \tag{A.2.66}$$

We are able to compute the integral (A.2.63) by using the residue theorem (A.2.30)

$$\oint_C f(z)dz = 2\,\pi\,i\sum_i \mathrm{Res}\,(f,z_i)$$

The next step is to calculate the residues of f^{PSc*}. Just as in the case of

the one index vector mode there are two poles within the contour (at z_+ and 0):

$$\text{Res}(f^{PSc*}, z_+) = \frac{i(1-x)\,(1-z_+^2)\csc\zeta}{\sqrt{1-x^2}\,z_+}, \tag{A.2.67}$$

$$\text{Res}(f^{PSc*}, 0) = \frac{i(1-x)\,(1+z_+^2)\csc\zeta}{\sqrt{1-x^2}\,z_+}. \tag{A.2.68}$$

The total residues is given as the product of (A.2.67) and (A.2.68)

$$\begin{aligned}\oint_C f(z)dz &= 2\,\pi\,i\,\sin\zeta\,\left(\text{Res}(f^{PSc*}, z_+) + \text{Res}(f^{PSc*}, 0)\right),\\ \oint_C f(z)dz &= 2\,\pi\,i\,\sin\zeta\left(\frac{i(1-x)\,(1-z_+^2)\csc\zeta}{\sqrt{1-x^2}\,z_+} + \frac{i(1-x)\,(1+z_+^2)\csc\zeta}{\sqrt{1-x^2}\,z_+}\right),\end{aligned} \tag{A.2.69}$$

Which simplifies down to give us

$$\oint_C f(z)dz = \frac{4\,\pi(1-x)\,z_+\,\sin\zeta}{\sqrt{1-x^2}}. \tag{A.2.70}$$

Finally, we are able to calculate the Hellings and Downs function (A.2.12)

$$\chi(\zeta) = (\ln(4) - 2\,\ln(1-\cos\zeta))\sin^2\left(\frac{\zeta}{2}\right). \tag{A.2.71}$$

This result can be plotted against the angle of separation between the two pulsars ("arms of the detector").

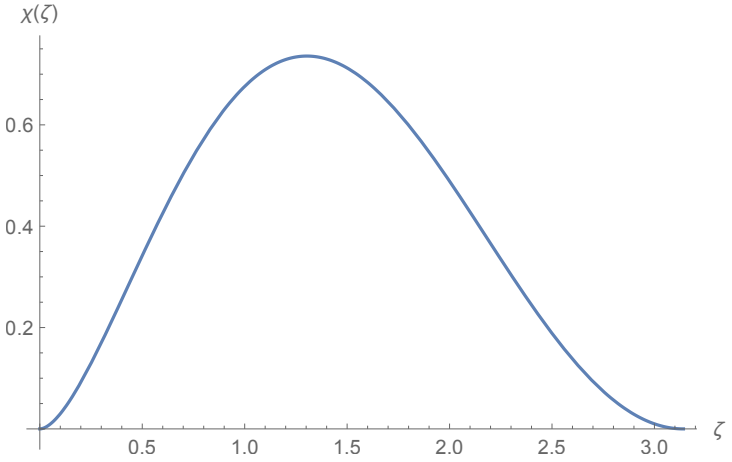

FIGURE A.3: Hellings and Downs Curve for pseudoscalar with one index.

How can we explain the pseudoscalar we've chosen physically? Must understand how the response functions for PTAs are constructed. Perhaps the axions have a long enough wavelength in order to affect both pulsar simultaneously. Perhaps axions have such a low frequency that the are unable to deform the arms of the interferometer/squeeze the Earth enough in order for the axions to be detected so the axions exist in a frequency range that cannot as yet be detected by any gravitational wave detector. Ways to combat this include (referring back to chapter 2) are to find a system which involves the axion which would be able to increase their mass (and therefore their frequency) to be within the range of the PTAs. Or the PTAs in the future will improve their observation range which may be able to detect the axions in their current mass limit.

An experiment was discussed in the first chapter involving axion interferometry [42, 99]. The effect of axion dark matter is to change the velocity of circularly polarised light. Therefore, the natural experiment to build is an interferometer where one arm has only left circularly polarised light and the other has right. The presence of axion dark matter would produce a difference in phase velocity between the two arms, thus generating an interference pattern. Extra wave plates can be added to Michelson interferometers to preserve polarisation. The same paper also proposed an interferometer where the same mirrors are used to form both cavities. Two quarter wave plates and a half wave plate are used to maintain circular polarisation of light [42].

Appendix B

A Non-Attractor Model of Inflation

B.1 Technical appendix: computation of two-point and three-point functions for tensor modes

In this Appendix, we go through the technical details of the results we discuss in the main text. We start showing that tensor duality allows us to obtain an analytical expression for tensor mode functions during the non-attractor era dual to a slow-roll phase: this is the basic ingredient we need for then analytically evaluating two point and three point functions in the non-attractor regime. For definiteness, the set-up we have in mind to realise this scenario is the same of Subsection 3.2.2, first discussed in [123]. In this case,

$$\begin{aligned} \mathcal{F}_T \;&\propto\; 1/a^6 \qquad c_T^2 = \mathcal{F}_T/\mathcal{G}_T \propto \text{constant} \\ &\text{during non-attractor phase}\,, \\ \mathcal{F}_T \;&\propto\; \text{constant} \quad c_T^2 = \mathcal{F}_T/\mathcal{G}_T \propto \text{constant} \end{aligned} \tag{B.1.1}$$

during slow-roll phase. (B.1.2)

We start by discussing the computation of the quadratic case, leading to the tensor power spectrum. To investigate the behavior of the tensor fluctuations, we define the canonically normalized tensor fluctuation $v_{ij} = z_T h_{ij}$ to re-write the leading order action (3.2.3) as

$$S_T^{(2)} = \frac{1}{2}\int \mathrm{d}y\,\mathrm{d}^3x\left[\left(v_{ij}'\right)^2 - \left(\vec{\nabla}v_{ij}\right)^2 + \frac{z_T''}{z_T}\,v_{ij}^2\right]. \tag{B.1.3}$$

Using the expression (3.2.10), this leads to the following equation of motion in Fourier space

$$v_{\mathbf{k}}'' + \left(k^2 - \frac{2}{y^2}\right)v_{\mathbf{k}} = 0, \tag{B.1.4}$$

where we have used the following expansion for the canonical tensor perturbation

$$v_{ij}(y,\mathbf{k}) = \sum_s e_{ij}^{(s)}(\mathbf{k})\Big[v_{\mathbf{k}}(y)a_s(\mathbf{k}) + v_{-\mathbf{k}}^*(y)a_s^\dagger(-\mathbf{k})\Big]. \tag{B.1.5}$$

Here, $e_{ij}^{(s)}$ is the polarization tensor with the helicity states $s = \pm$, satisfying $e_{ii}^{(s)}(\mathbf{k}) = 0 = k_j e_{ij}^{(s)}(\mathbf{k})$. Our normalisation is

$$e_{ij}^{(s)}(\mathbf{k})e_{ij}^{*(s')}(\mathbf{k}) = \delta_{ss'}, \tag{B.1.6}$$

and we choose the phase so that the following relations hold:

$$e_{ij}^{*(s)}(\mathbf{k}) = e_{ij}^{(-s)}(\mathbf{k}) = e_{ij}^{(s)}(-\mathbf{k}). \tag{B.1.7}$$

The commutation relation for the creation and annihilation operators is

$$[a_s(\mathbf{k}), a_{s'}^\dagger(\mathbf{k}')] = (2\pi)^3\delta_{ss'}\delta(\mathbf{k}-\mathbf{k}'). \tag{B.1.8}$$

The mode equation in (B.1.4) implies that the power spectrum of the fluctuations $v_{\mathbf{k}}$ is scale invariant on large scales. In order to see this, we note the

solution to the differential equation in (B.1.4) that reduces to the adiabatic vacuum on small scales which reads

$$v_{\mathbf{k}}(y) = \frac{1}{\sqrt{2k}}\left(1 - \frac{i}{ky}\right)e^{-iky}, \tag{B.1.9}$$

so that $\mathcal{P}_h \sim k^3|v_k|^2 \propto k^0$ in the limit $-ky \to 0$, as anticipated. Using (B.1.9) and the formulae for z_T, we write the solution to the original tensor mode function by using $h_{\mathbf{k}} \equiv v_{\mathbf{k}}/z_T$,

$$h_{\mathbf{k}}(y) = \frac{i\sqrt{2}H}{\sqrt{c_T\mathcal{F}_T k^3}}\,(1+iky)\,e^{-iky}, \tag{B.1.10}$$

which essentially has the same form as the one in the slow-roll approximation (see eq (11) of [216]), although in this case $\mathcal{F}_T$ is strongly time dependent, as discussed in Section 3.2.2 of the main text. Indeed, $\mathcal{F}_T$ is evolving rapidly as $\propto a^{-6}$ during the non-attractor regime contrary to the case in slow-roll where $\mathcal{F}_T \simeq$ constant, see eqs (3.2.12).

The two point function and the tensor power spectrum

Starting from the two point function of tensor modes in Fourier space, the power spectrum of tensor fluctuations can be defined by $\mathcal{P}_h = (k^3/2\pi^2)\mathcal{P}_{ij,ij}$ using the following expressions[1]

$$\langle h_{ij}(\mathbf{k})h_{kl}(\mathbf{k}')\rangle = (2\pi)^3\delta(\mathbf{k}+\mathbf{k}')\mathcal{P}_{ij,kl}(\mathbf{k}), \tag{B.1.11}$$

$$\mathcal{P}_{ij,kl}(\mathbf{k}) = |h_{\mathbf{k}}|^2\Pi_{ij,kl}(\mathbf{k}), \tag{B.1.12}$$

where

$$\Pi_{ij,kl}(\mathbf{k}) = \sum_s e_{ij}^{(s)}(\mathbf{k})e_{kl}^{*(s)}(\mathbf{k}). \tag{B.1.13}$$

[1]Sometimes, it is also convenient to use the quantity $P_h(\mathbf{k}) \equiv \frac{\mathbf{2\pi^2\,\mathcal{P}_h(k)}}{\mathbf{k^3}}$.

We learn that on super horizon scales $-ky \to 0$, one still gets a scale invariant power spectrum of primordial tensor fluctuations during the non-attractor phase.

$$\mathcal{P}_h = \lim_{-ky\to 0} \frac{k^3}{2\pi^2} 2|h_{\mathbf{k}}|^2 = \frac{2}{\pi^2}\frac{H^2}{\mathcal{F}_T c_T}. \tag{B.1.14}$$

However, since the tensor kinetic term evolves as $\mathcal{F}_T \propto a^{-6}$, the amplitude of the power spectrum grows on super-horizon scales and therefore it has to be evaluated at the end of the non-attractor era. These result shows an agreement with what one would expect from the duality arguments discussed in [185], namely the power spectrum grows on superhorizon scales while it preserves a scale invariant form.

The three point function and the tensor bispectrum

The tensor bispectrum can be computed by employing the in-in formalism (see e.g. [283]), starting from the three point function in Fourier space

$$\begin{aligned}\langle h_{i_1 j_1}(\mathbf{k}_1) h_{i_2 j_2}(\mathbf{k}_2) h_{i_3 j_3}(\mathbf{k}_3)\rangle = -i \int_{t_i}^{t} \mathrm{d}t' \\ \Big\langle \ [h_{i_1 j_1}(t,\mathbf{k}_1) h_{i_2 j_2}(t,\mathbf{k}_2) h_{i_3 j_3}(t,\mathbf{k}_3), H_{\rm int}(t')] \ \Big\rangle,\end{aligned} \tag{B.1.15}$$

where t_i is some early time when the perturbation is well inside the sound horizon and the interaction Hamiltonian is given by $H_{\rm int}(t) = -\int \mathrm{d}^3x \ \mathcal{L}_T^{(3)}$. We find it convenient to work with the time coordinate y in evaluating the three point function. We express all the time dependent quantities with respect to the time when the non-attractor era ends, $y_{\rm end}$. Using (B.1.10), the mode functions therefore take the following form

$$h_{\mathbf{k}}(y) = \frac{i\sqrt{2}H}{\sqrt{c_T \mathcal{F}_T^{(\rm end)} k^3}} \ (1+iky) \ e^{-iky} \left(\frac{y_{\rm end}}{y}\right)^3, \tag{B.1.16}$$

where $^{(0)}$ denotes the value of the quantity at the beginning of the non-attractor era. Using the expansions in (B.1.5) (and noting $h_{ij} = v_{ij}/z_T$),

we take the commutators in (B.1.17) by taking into account the relations between the polarization tensors (B.1.6),(B.1.7) and (B.1.8).

This procedure yields to the following expression for three point function,

$$\begin{aligned}&\langle h_{i_1j_1}(\mathbf{k}_1)h_{i_2j_2}(\mathbf{k}_2)h_{i_3j_3}(\mathbf{k}_3)\rangle\\&= (2\pi)^3\delta(\mathbf{k}_1+\mathbf{k}_2+\mathbf{k}_3)\ \mathcal{T}^{(\alpha)}_{i_1j_ii_2j_2i_3j_3}\Big(2\ \mathrm{Im}[\ \mathcal{I}^{(\alpha)}(y)\ ]\Big),\end{aligned}\tag{B.1.17}$$

where the form of tensorial part $\mathcal{T}^{(\alpha)}$ and the function $\mathcal{I}^{(\alpha)}(y)$ depends on the interaction term under consideration in the third order action (3.3.1), denoted by the superscript $\alpha = (\mathrm{GR}, \mathrm{new})$.

• **The 'GR' contribution**

We begin our calculations by the first term in the interaction Hamiltonian $H_{\rm int}(t) = -\int \mathrm{d}^3x\ \mathcal{L}^{(3)}_T$, using the interaction Lagrangian (3.3.1) which we denote by $\alpha \to \mathrm{GR}$. In this case the tensorial part is given by

$$\begin{aligned}\mathcal{T}^{(\mathrm{GR})}_{i_1j_1i_2j_2i_3j_3} = &\quad\Big\{\Pi_{i_1j_1,ik}(\mathbf{k}_1)\Pi_{i_2j_2,jl}(\mathbf{k}_2)\Big[k_{3k}k_{3l}\Pi_{i_3j_3,ij}(\mathbf{k}_3)\\&-\quad\frac{1}{2}k_{3i}k_{3k}\Pi_{i_3j_3,jl}(\mathbf{k}_3)\Big] + 5\text{ perms of }1,2,3\Big\}.\end{aligned}\tag{B.1.18}$$

where recall the definition of the four-index tensor Π in eq (B.1.13). Since the tensor modes evolve outside the horizon during the non-attractor regime, we need to evaluate the function $\mathcal{I}$ (and hence the bispectrum) at the end of the non-attractor era beyond which we assume the mode functions (as well as time dependent quantities such as $\mathcal{F}_T$) freeze-out, since we return into a standard slow-roll phase. We are therefore interested in the following expression

$$\begin{aligned}\mathcal{I}^{(\mathrm{GR})} &= h_{\mathbf{k_1}}(y_{\rm end})h_{\mathbf{k_2}}(y_{\rm end})h_{\mathbf{k_3}}(y_{\rm end})\int_{-\infty}^{y_{\rm end}}\mathrm{d}y'\\&\times\quad\frac{a^2(y')\mathcal{F}_T(y')}{4\ c_T}\ h^*_{\mathbf{k_1}}(y')h^*_{\mathbf{k_2}}(y')h^*_{\mathbf{k_3}}(y'),\end{aligned}\tag{B.1.19}$$

where we take $y_i \to -\infty$ to ensure all modes of interest are inside the horizon initially and $y_{\rm end}$ denotes the end of non-attractor era. Noting the behavior of the mode functions in (B.1.10) and of the tensor kinetic function $\mathcal{F}_T \propto y^6$ during the non-attractor era, the function $\mathcal{I}^{(\rm GR)}$ contains integrals of the following form

$$\mathcal{C}_p^{(\alpha)} = \int_{\infty}^{x_{\rm end}} {\rm d}x' \; (x')^{-p} \; e^{-ix'}, \tag{B.1.20}$$

where we defined $x' \equiv -Ky'$ with $K = \sum_i k_i$ and $|\mathbf{k_i}| = k_i$. For the GR contribution we are focussing on, p is a positive integer with the following possible values, $p = \{5, 4, 3, 2\}$. The result of the integration can be expressed in terms of the incomplete Gamma functions,

$$\mathcal{C}_p^{(\alpha)} = -(-i)^{1-p} \; \Gamma(1-p, ix_{\rm end}) \tag{B.1.21}$$

which has the following series expansion for negative integer values of its first argument

$$\Gamma(-m, z) = \frac{1}{m!}\left(\frac{e^{-z}}{z^m}\sum_{k=0}^{m-1}(-1)^k(m-k-1)! \; z^k + (-1)^m \; \Gamma(0, z)\right). \tag{B.1.22}$$

The results above are valid as far as we are away from the origin $x_{\rm end} = 0$ but diverges as $x_{\rm end} \to 0$. In the following, we will express our results for small but non-zero value of $x_{\rm end} \equiv -Ky_{\rm end} < 1$. Moreover, notice that the incomplete Gamma $\Gamma(0, z)$ (also known as the exponential integral $E_1(z)$) admits the following useful power series expansion in terms of elementary functions,

$$\Gamma(0, z) = -\gamma_E - \ln(z) - \sum_{k=1}^{\infty}\frac{(-z)^k}{k \; k!}, \tag{B.1.23}$$

where γ_E is the Euler-Mascheroni constant. Following the discussion above, we use (B.1.21) with (B.1.22) and (B.1.23) to present our results at next to leading order in $-Ky_{\rm end} < 1$. Keeping in mind the full expression in (B.1.19), we thus have

$$2 \; {\rm Im}[\mathcal{I}^{(\rm GR)}] = \frac{(2\pi)^4 \mathcal{P}_h^{(\rm end)^2}}{\Pi_i \; k_i^3}$$

$$\times -\frac{K}{64}\Bigg[\left(1-\frac{3}{K^3}\sum_{i\neq j}k_i^2k_j-\frac{6}{K^3}\Pi_i k_i\right)(-Ky_{\rm end})^2$$
$$\frac{\pi}{4}\left(1-\frac{4}{K^3}\sum_{i\neq j}k_i^2k_j-\frac{4}{K^3}\Pi_i k_i\right)(-Ky_{\rm end})^3\Bigg], \qquad \text{(B.1.24)}$$

where we made use of the expression for the power spectrum in (B.1.14) evaluated at the end of the non-attractor era. With these ingredients, we can express the tensor three point function associated with the 'GR' contribution as

$$\begin{aligned}\langle h_{i_1j_1}(\mathbf{k}_1)h_{i_2j_2}(\mathbf{k}_2)h_{i_3j_3}(\mathbf{k}_3)\rangle &= (2\pi)^7\delta(\mathbf{k}_1+\mathbf{k}_2+\mathbf{k}_3)\\ &\times \frac{\mathcal{P}_h^{(\rm end)^2}}{\Pi_i\ k_i^3}\ \mathcal{A}^{(\rm GR)}_{i_1j_ii_2j_2i_3j_3}, \end{aligned}\qquad \text{(B.1.25)}$$

where we defined $\mathcal{A}^{(\rm GR)}_{i_1j_ii_2j_2i_3j_3}\equiv\mathcal{A}^{(\rm GR)}(k_1,k_2,k_3)\ \mathcal{T}^{(\rm GR)}_{i_1j_ii_2j_2i_3j_3}$ with $\mathcal{T}^{(\rm GR)}$ given in eq (B.1.18),

$$\mathcal{A}^{(\rm GR)}=-\frac{K}{64}\Bigg[\left(1-\frac{3}{K^3}\sum_{i\neq j}k_i^2k_j-\frac{6}{K^3}\Pi_i k_i\right)(-Ky_{\rm end})^2$$
$$-\frac{\pi}{4}\left(1-\frac{4}{K^3}\sum_{i\neq j}k_i^2k_j-\frac{4}{K^3}\Pi_i k_i\right)(-Ky_{\rm end})^3+\ldots\Bigg], \qquad \text{(B.1.26)}$$

and dots indicates sub-leading terms higher order in $-Ky_{\rm end}$. The amplitude $\mathcal{A}^{(\rm GR)}$ shows the scale dependence of the non-Gaussianity parameterized by the powers of $-Ky_{\rm end}<1$ during the non-attractor era.

• **The 'new' contribution**

In a similar fashion, we now move on to calculate the contribution to the tensor three point function from the second term in the interaction Hamiltonian (see *e.g.* (3.3.1)). Following the same steps as we did for the previous term, we write the three point function in the same form as in (B.1.17) with

$$\mathcal{T}^{(\rm new)}_{i_1j_1i_2j_2i_3j_3}=\Pi_{i_1j_1,ij}(\mathbf{k}_1)\Pi_{i_2j_2,jk}(\mathbf{k}_2)\Pi_{i_3j_3,kl}(\mathbf{k}_3) \qquad \text{(B.1.27)}$$

and

$$\begin{aligned}\mathcal{I}^{(\rm new)} &= -h_{\mathbf{k_1}}(y_{\rm end})h_{\mathbf{k_2}}(y_{\rm end})h_{\mathbf{k_3}}(y_{\rm end})\int_{-\infty}^{y_{\rm end}}{\rm d}y' \\ &\times \frac{c_T^2 a\dot\phi X G_{5X}}{2}\, h^{*'}_{\mathbf{k_1}}(y')h^{*'}_{\mathbf{k_2}}(y')h^{*'}_{\mathbf{k_3}}(y'). \end{aligned} \tag{B.1.28}$$

Here a prime on the mode functions denotes a time derivative with respect to their argument y'. We note that since the integral contains these time derivatives, the calculation of the 3-pt function associated with this contribution is more involved compared to the previous case. In order to deal with the integral in (B.1.28), we note the time derivative of the complex conjugated mode function as

$$h^{*'}_{\mathbf{k}}(y) = -\frac{i\sqrt{2}H}{\sqrt{c_T\mathcal{F}_T^{(\rm end)}k^3}}\left(\frac{y_{\rm end}}{y}\right)^3\left\{-\frac{3}{y}(1-iky)+k^2y\right\}\, e^{iky}, \tag{B.1.29}$$

which reflects the rapid change of the mode functions after horizon crossing ($-ky\to 0$). Noting the time dependence of the functions inside the integral, *i.e.* $\dot\phi\propto a^{-3}$, $X\propto a^{-6}$ and $G_{5X}\propto a^3$, we see that we need to deal with integrals that has the same form as in (B.1.20) with $p=\{7,6,5,4,3,2,1\}$. Therefore, repeating the same steps as we did for the "GR" term, we obtain the following results for $2{\rm Im}[\mathcal{I}^{(\rm new)}]$ at next to leading order in $-Ky_{\rm end}$,

$$\begin{aligned}2\ {\rm Im}[\mathcal{I}^{(\rm new)}] = &-\frac{(2\pi)^4\mathcal{P}_h^{(\rm end)^2}}{\Pi_i\ k_i^3}\ \frac{3H\mu^{(\rm end)}}{16\mathcal{G}_T^{(\rm end)}}\Bigg\{\left(K^3-3\sum_{i\neq j}k_i^2k_j-6\ \Pi_i k_i\right) \\ &-\frac{1}{4}\left(K^3-5\sum_{i\neq j}k_i^2k_j+\frac{2}{K^2}\sum_{i\neq j}k_i^3k_j^2\right)(-Ky_{\rm end})^2\Bigg\},\end{aligned} \tag{B.1.30}$$

where we defined $\mu^{(\rm end)}\equiv\dot\phi^{(\rm end)}X^{(\rm end)}G_{5X}^{(\rm end)}$. The contribution of this term to the 3pt function can be written similarly to the expression in (B.1.25) where we define the amplitude $\mathcal{A}^{(\rm new)}_{i_1j_ii_2j_2i_3j_3}\equiv\mathcal{A}^{(\rm new)}(k_1,k_2,k_3)\ \mathcal{T}^{(\rm new)}_{i_1j_ii_2j_2i_3j_3}$ and

$$\mathcal{A}^{(\rm new)} = -\frac{3H\mu^{(\rm end)}}{16\mathcal{G}_T^{(\rm end)}}\Bigg\{\left(K^3-3\sum_{i\neq j}k_i^2k_j-6\ \Pi_i k_i\right)$$

$$-\frac{1}{4}\left(K^3-5\sum_{i\neq j}k_i^2k_j+\frac{2}{K^2}\sum_{i\neq j}k_i^3k_j^2\right)(-Ky_{\rm end})^2\Bigg\}. \tag{B.1.31}$$

This result shows that the contribution of the new term to the amplitude of the bispectrum has a scale independent piece plus a scale dependent subleading term, which becomes small as $-Ky_{\rm end}\to 0$. The difference between the scale dependence of the $\mathcal{A}^{(\rm new)}$ and $\mathcal{A}^{(\rm GR)}$ can be understood by analyzing the time dependence of each term in the interaction Lagrangian (3.3.1). For example, during the non-attractor phase the new term can be written schematically as $a^{-6}hhh$ whereas the GR term scales with scale factor as $a^{-8}hhh$ where we have suppressed the indices on the metric. This explains why the contribution from each term differs by a factor $y_{\rm end}^{-2}$ at leading order in the amplitude of the bispectrum.

B.2 Disformal transformation and tensor non-Gaussianity

The general quadratic action for tensors in (3.2.3) can be transformed into a form identical to the action for tensor fluctuations in general relativity (GR) by applying a disformal and conformal transformation to the metric successively [200, 201]. In this appendix, we discuss the implications[2] of such transformations for the background dynamics and for the tensor bispectrum we discussed earlier in Section 3.3 and Appendix B.1. For our system, the corresponding combination of disformal and conformal transformation is given by

$$g_{\mu\nu}\to\frac{\mathcal{F}_T}{c_T}\left[g_{\mu\nu}+(1-c_T^2)n_\mu n_\nu\right], \tag{B.2.1}$$

[2]See also [284] for a general analysis of the consequences of disformal transformations on cosmological fluctuations.

which corresponds to the following re-labeling of the time coordinate and re-definition of the scale factor,

$$\mathrm{d}\hat{t} = (c_T \mathcal{F}_T)^{1/2} \mathrm{d}t, \qquad \hat{a}(\hat{t}) = \left(\frac{\mathcal{F}_T}{c_T}\right)^{1/2} a(t). \tag{B.2.2}$$

Using the transformations in (B.2.2), the quadratic action in (3.2.3) take the standard form that appear in GR,

$$\begin{aligned} S_T^{(2)} &= \frac{1}{8}\int \mathrm{d}\hat{t}\ \mathrm{d}^3x\ \hat{a}(\hat{t})^3 \left[(\partial_{\hat{t}} h_{ij})^2 - \frac{1}{\hat{a}(\hat{t})^2}(\vec{\nabla} h_{ij})^2\right], \\ &= \frac{1}{2}\int \mathrm{d}y\ \mathrm{d}^3x\ \frac{\hat{a}^2}{4}\left[(\partial_y h_{ij})^2 - (\vec{\nabla} h_{ij})^2\right], \end{aligned} \tag{B.2.3}$$

where in the second line we have used the fact that the conformal time in the GR frame is defined by the coordinate y , namely $\mathrm{d}\hat{t}/\hat{a}(\hat{t}) \equiv \mathrm{d}y$, which can be seen by combining the expressions given in (B.2.2).

In order to describe the time evolution of the background in the Einstein Frame, we make use of the relation between two scale factors in (B.2.2) together with the fact that $\mathcal{F}_T \propto a^{-6}$ and $a \propto -1/y$. This procedure leads to the conclusion that, universe appear to be collapsing as in a dust dominated universe, that is

$$\hat{a} \propto y^2, \tag{B.2.4}$$

as $y \to 0$. Similarly, we can relate the Hubble rate in the Einstein frame, $\hat{H} = \mathrm{d}\ln\hat{a}/\mathrm{d}\hat{t}$, to the Hubble rate in the Jordan frame using (B.2.2), which leads to

$$\hat{H} = -\frac{2H}{(c_T \mathcal{F}_T)^{1/2}} \propto \hat{a}^{-3/2}, \tag{B.2.5}$$

as expected from a dust dominated universe. Using the transformation (B.2.5) for the Hubble rate, the power spectrum of tensor fluctuations in the Jordan frame can be expressed in terms of the quantities in the Einstein frame as

$$\mathcal{P}_h = \frac{\hat{H}^2}{2\pi^2} \propto \hat{a}^{-3}. \tag{B.2.6}$$

This expression reflects the equivalence of the interpretation of the results

in both frames. In the Einstein frame, the power spectrum of tensor fluctuations also appear to be increasing during the transient collapsing[3] phase as $\hat{a} \to 0$.

The equivalence of the results in both frames also extends to the observables such as the tensor non-Gaussianity. In the following, we prove that the calcuation of the bispectrum is equivalent in both frames. For this purpose, we first realize from (B.2.3) and (B.2.4) that the canonical variable $v_{ij} = z_T h_{ij}$ with $z_T = \hat{a}/2$ satisfies the same equation in Fourier space similar to the case during the non-attractor phase (See, *e.g.* eq. (B.1.4)). Therefore, in the Einstein frame, the mode functions that reduces to the Bunch-Davies vacuum is given by,

$$h_{\mathbf{k}} = \frac{-i\hat{H}}{\sqrt{2k^3}}\,(1+iky)\,e^{-iky}. \tag{B.2.7}$$

Notice that using the relation (B.2.5), the mode functions appear to have the same form as the one in the non-attractor phase (B.1.16):

$$h_{\mathbf{k}} = \frac{i\sqrt{2}H}{\sqrt{c_T\mathcal{F}_T k^3}}\,(1+iky)\,e^{-iky}, \tag{B.2.8}$$

where $\mathcal{F}_T = \mathcal{F}_T^{(\rm end)}(y/y_{\rm end})^6$. In order to establish the equivalence of the in-in calculation in both frames, we therefore only need to focus on the time dependence of the interaction Hamiltonian in the Einstein frame, which is given by

$$\begin{aligned} H_{\rm int}(y) &= -\int \mathrm{d}^3x \left[\frac{Q_{\rm new}(y)}{12}\; h'_{ij}h'_{jk}h'_{ki}\right. \\ &+ \left.\frac{\hat{a}^2(y)}{4}\left(h_{ik}h_{jl}-\frac{1}{2}h_{ij}h_{kl}\right)\partial_k\partial_l h_{ij}\right], \end{aligned} \tag{B.2.9}$$

where prime denotes a time derivative w.r.t y and we have defined the time dependent pre-factor of the new interaction as

$$Q_{\rm new} = \frac{\hat{a}\mathcal{F}_T^{3/4}}{\mathcal{G}_T^{5/4}} X\dot{\phi}G_{5X}. \tag{B.2.10}$$

[3]Note that similar to the time span $y_0 < y < y_{\rm end}$ of the non-attractor era in the Jordan frame, the collapsing phase in the Einstein frame will last for a finite time.

We proceed the in-in calculation in the Einstein frame by defining analogues of the functions $\mathcal{I}^{(\rm new)}$ and $\mathcal{I}^{(\rm GR)}$ that we defined earlier in the Jordan frame. Following the same steps as we before, these functions in the Einstein frame is given by

$$\hat{\mathcal{I}}^{(\rm GR)} = h_{\mathbf{k_1}}(y_{\rm end})h_{\mathbf{k_2}}(y_{\rm end})h_{\mathbf{k_3}}(y_{\rm end}) \int_{-\infty}^{y_{\rm end}} {\rm d}y' \times \frac{\hat{a}^2(y')}{4}\, h^*_{\mathbf{k_1}}(y')h^*_{\mathbf{k_2}}(y')h^*_{\mathbf{k_3}}(y'), \tag{B.2.11}$$

$$\hat{\mathcal{I}}^{(\rm new)} = -h_{\mathbf{k_1}}(y_{\rm end})h_{\mathbf{k_2}}(y_{\rm end})h_{\mathbf{k_3}}(y_{\rm end}) \int_{-\infty}^{y_{\rm end}} {\rm d}y' \times \frac{Q_{\rm new}(y')}{2}\, h^{*'}_{\mathbf{k_1}}(y')h^{*'}_{\mathbf{k_2}}(y')h^{*'}_{\mathbf{k_3}}(y'), \tag{B.2.12}$$

where $y_{\rm end}$ denotes the end of the collapsing phase. Noting $\hat{a} \propto y^2$ and $Q_{\rm new} \propto \hat{a}^{5/2} \propto y^5$ and the mode functions in (B.2.8), we see that we need to deal with identical integrals in the calculation of bispectrum amplitude in the Einstein frame. In particular, defining the dimensionless variable $x' = -Ky'$, integrals have the same form as before (See for example, eq. (B.1.20)):

$$\mathcal{C}_p^{(\alpha)} = \int_{\infty}^{x_{\rm end}} {\rm d}x'\ (x')^{-p}\ e^{-ix'}, \tag{B.2.13}$$

where α labels the new or the GR term with $p = \{7,6,5,4,3,2,1\}$ and $p = \{5,4,3,2\}$. Therefore, as expected, one can reach at the same results we derived earlier for the amplitude of the bispectrum in the Einstein frame.

B.3 An explicit scenario with large tensor non-Gaussianity

In this appendix we apply the results presented in the main text, for the amplitude of tensor non-Gaussianity during a phase of non-attractor inflation, to a concrete model. We use the model introduced in Section 3.2.2, which is based on the Horndeski theory of gravity, choosing the Horndeski functions as in (3.2.21). The model is discussed in detail in [123], and we

present in this appendix only a brief summary of the relevant dynamics and parameter space. In particular, our purpose here is to identify a consistent parameter space for the model, which gives rise to a large tensor bispectrum during a non-attractor phase.

We allow the free parameters, $\rho, \alpha, \nu, \delta, \beta$ and σ in (3.2.21) to take different values during three different phases of inflationary evolution. Provided that the parameters satisfy certain relations, the equations of motion admit a solution with a constant Hubble parameter and continuous metric and $\dot{\phi}$, consisting of two slow roll inflationary phases, during which $\dot{\phi} = const$, connected by a transient non-attractor self-accelerating de Sitter phase that is tensor dual to the initial slow roll phase, with $\dot{\phi} \propto 1/a^3$. As we show in [123], such a solution is possible provided that the parameters satisfy $\rho = 2\delta + 3\beta + 4\sigma$ and $\nu = 0$, during the non-attractor phase.

Whilst the non-minimal derivative couplings between metric and scalar in Horndeski Lagrangians have been chosen to allow a non-attractor inflationary phase, tensor dual to slow roll, care must be taken so that they do not also introduce ghost or gradient instabilities in the tensor and scalar fluctuations. As discussed in detail in [123], the stability constraints restrict the parameter space to $\rho < 0$, $\beta > 0$, $\sigma < 0$, $\delta < 0$, $\beta + 9\sigma < 0$, $\beta + 3\sigma > 0$ and $f_s > 0$, during the non-attractor era, where

$$f_s = \frac{-2\beta^2 + \delta(\beta + 9\sigma) + 3\sigma(\beta + 3\sigma)}{6(3\beta + \delta + 6\sigma)}. \tag{B.3.1}$$

Referring to [123] for the explicit solution for $\dot{\phi}$ in the non-attractor phase, we now write the non-linearity parameter given in (3.3.9) in terms of the model parameters:

$$\hat{f}^{+++}_{\mathrm{NL(new)}} = \frac{135}{512}\frac{H\mu^{\mathrm{end}}}{\mathcal{G}_T^{\mathrm{end}}} = -\frac{135}{512}\frac{3\sigma}{2(\beta + 3\sigma)}. \tag{B.3.2}$$

It is clear from the expression above that bispectrum amplitude can be large, in the limit $\beta \to -3\sigma$. In order to parametrize the proximity to this

limit and hence the enhancement of the bispectrum, we thus set $\beta = -3\sigma + \epsilon$ where $0 < \epsilon \ll -3\sigma$. Notice that this parametrization guarantees that the stability conditions $\beta + 3\sigma > 0$ and $\beta + 9\sigma < 0$ are satisfied, when $\sigma < 0$. The condition $f_s > 0$ can then be satisfied by fixing the parameter δ within the range:

$$3\sigma - 3\epsilon + \frac{5\epsilon^2}{6\sigma} < \delta < 3\sigma - 3\epsilon. \tag{B.3.3}$$

We can then set the final parameter ρ using $\rho = 2\delta + 3\beta + 4\sigma$ as required by the equations of motion in the non-attractor self-accelerating de Sitter background.

The expressions (B.3.2) and (B.3.3) imply that in order to enhance the bisepctrum by an amount ϵ^{-1}, we require a cancellation between β and $3|\sigma|$ at the order of ϵ, together with a fine-tuning of δ (and thus ρ) at the order of ϵ^2. As shown in [123], an enhancement for the tensor power spectrum is also achieved, by choosing the parameter α to be suppressed in the non-attractor regime, with respect to the slow-roll regime preceding it. The scalar power spectrum is also enhanced, by a smaller factor. For example, for the parameters considered in [123] – $\sigma = -0.2$, $\beta = 1.5$, $\delta = -4$, $\alpha_{\rm sr}/\alpha_{\rm na} = 10^{-3}$ – the scalar power spectrum is enhanced by a factor 5.3×10^6, the tensor power spectrum by a factor of 5.0×10^7 and the non-linearity parameter, (B.3.2), is $\hat{f}^{+++}_{\rm NL(new)} = 0.088$. Fine-tuning instead $\sigma = -1$, $\beta = 3.001$, $\delta = -3.003007$ and $\alpha_{\rm sr}/\alpha_{\rm na} = 10^{-6}$, the scalar power spectrum is enhanced by a factor 5.5×10^7, the tensor power spectrum by a factor of 1.3×10^8 and the non-linearity parameter, (B.3.2), is $\hat{f}^{+++}_{\rm NL(new)} = 395.5$. We see that – with sufficient fine-tuning – large, potentially observable tensor non-Gaussianities can occur.

Appendix C

Conventions for the polarization tensors and the IPTA data set

C.1 Conventions for the polarization tensors

We adopt standard conventions for the polarization tensors adapted to the GW direction $\hat{n}$, the same used in [199]. We assume a Cartesian coordinate system with orthogonal axis $(\hat{x}, \hat{y}, \hat{z})$. Starting from the GW direction $\hat{n}$ we define two orthogonal unit vectors $\hat{u}$ and $\hat{v}$:

$$\hat{u} = \frac{\hat{n} \times \hat{z}}{|\hat{n} \times \hat{z}|} \quad , \quad \hat{v} = \hat{n} \times \hat{u} \, . \tag{C.1.1}$$

Using these unit vectors, we can define two tensor polarizations $(+, \times)$:

$$e^{(+)}_{ab} = \frac{\hat{u}_a \hat{u}_b - \hat{v}_a \hat{v}_b}{\sqrt{2}} \, , \tag{C.1.2}$$

$$e^{(\times)}_{ab} = \frac{\hat{u}_a \hat{v}_b + \hat{v}_a \hat{u}_b}{\sqrt{2}} \tag{C.1.3}$$

which satisy $e^{(+)}_{ab}e^{(+)}_{ab} = 1 = e^{(\times)}_{ab}e^{(\times)}_{ab}$, $e^{(+)}_{ab}e^{(\times)}_{ab} = 0$. From these objects, we obtain the chiral polarization operators (R, L) which we use in the main text:

$$e^{(R,L)}_{ab} = \frac{e^{(+)}_{ab} \pm i\, e^{(\times)}_{ab}}{\sqrt{2}}\,. \tag{C.1.4}$$

For what respect the breathing scalar mode we adopt the following polarization tensor [281]:

$$e^{(S)}_{ab} = \frac{\hat{u}_a\hat{u}_b + \hat{v}_a\hat{v}_b}{\sqrt{2}}\,. \tag{C.1.5}$$

C.2 The IPTA data set

Table C.2 contains data from 49 pulsars which are observed by the International Pulsar Timing Array (IPTA). The IPTA consists of various pulsar timing arrays throughout the world. This includes the Parkes Pulsar Timing Array (PPTA) in Australia, NanoGrav (consisting of Arecibo (Puerto Rico) and Green Bank Telescope (USA)) and the European Pulsar Timing Array (EPTA) (consisting of Effelsberg Radio Telescope (Germay), Nançay (France), Lovell Telescope (UK), Sardina Radio Telescope (Italy) and Synthesis Radio Telescope (Netherlands)). The combination of these various arrays allows for a larger data set of pulsars to be observed.

Pulsar Name	**RMS** $[\mu s]$	**TOAs**
J0030+0451	1.9	1,030
J0034-0538	4.4	267
J0218+4232	6.7	1,005
J0437–4715	0.3	5,052
J0610–2100	5.2	347
J0613–0200	1.2	2,940
J0621+1002	11.5	637
J0711–6830	2.0	549
J0751–6830	3.5	1,129
J0900–3144	3.4	575
J1012+5307	1.7	2,910
J1022+1001	2.2	1375
J1024–0719	5.9	918
J1045–4509	3.3	635
J1455–3330	4.0	1,495
J1600–3053	0.8	1,697
J1603–7202	2.3	483
J1640+2224	2.0	1,139
J1643–1224	2.7	2,395
J1713+0747	0.3	19,972
J1721–2457	25.5	152
J1730–2304	2.1	5.63
J1732–5049	2.5	242
J1738+0333	2.6	206
J1744–1134	1.1	2,589
J1751–2857	2.4	78
J1801–1417	4.6	86
J1802–2124	4.3	433
J1804–2717	4.5	76

J1824–2452A	2.4	298
J1843–1113	1.7	186
J1853+1303	1.1	566
J1857+0943	1.3	1,641
J1909–3744	0.2	2,623
J1910+1256	3.0	597
J1911+1347	0.6	45
J1911–1114	5.3	81
J1918–0642	1.5	1,522
J1939+2134	70.0	3,905
J1955+2908	5.0	319
J2010–1323	1.9	296
J2019+2425	8.8	80
J2033+1734	13.3	130
J2124–3358	3.0	1115
J2129–5721	1.2	447
J2145–0750	1.2	2,347
J2229+2643	3.8	234
J2317+1439	1.6	867
J2322+2057	6.9	199

TABLE C.1: *Pulsars analyzed by IPTA [258].*

J1824-2452A is followed by a letter in order to differentiate between pulsars that are in close proximity (otherwise it is difficult to give them unique names).

The pulsar names are determined by the coordinates in the sky. Pulsars with a J in front of the coordinates mean that they have more precise coordinates than older pulsars (before 1993 and these are denoted with a

B). The first number is the right ascension which is the a point along the celestial equator between the sun and the March equinox to the point above the earth which is in question. This is measured in hours and minutes. The other section of the coordinates is determined by its declination which is how far above (+) or below (–) the pulsar is with respect to the celestial equator. Note that older pulsars (that begin with a B) only have their declination to the nearest degree whilst the J pulsars have more accurate coordinates. Right ascension can be converted to degrees as follows:

$$RA_{deg} = \text{hour} + \frac{\text{min}}{60} + \frac{\text{sec}}{3600}. \tag{C.2.1}$$

Bibliography

[1] Ogan Ozsoy, Maria Mylova, Susha Parameswaran, Cari Powell, Gianmassimo Tasinato, and Ivonne Zavala. Squeezed tensor non-Gaussianity in non-attractor inflation. 2019.

[2] Cari Powell and Gianmassimo Tasinato. Probing a stationary non-Gaussian background of stochastic gravitational waves with pulsar timing arrays. *JCAP*, 2001(01):017, 2020. [doi].

[3] F. Zwicky. On the Masses of Nebulae and of Clusters of Nebulae. *Astrophys. J.*, 86:217–246, 1937. [doi].

[4] Alan H. Guth. The Inflationary Universe: A Possible Solution to the Horizon and Flatness Problems. *Phys. Rev.*, D23:347–356, 1981. [doi]. [Adv. Ser. Astrophys. Cosmol.3,139(1987)].

[5] Igor G. Irastorza and Javier Redondo. New experimental approaches in the search for axion-like particles. *Prog. Part. Nucl. Phys.*, 102: 89–159, 2018. [doi].

[6] Joerg Jaeckel and Andreas Ringwald. The Low-Energy Frontier of Particle Physics. *Ann. Rev. Nucl. Part. Sci.*, 60:405–437, 2010. [doi].

[7] R. D. Peccei and Helen R. Quinn. CP Conservation in the Presence of Instantons. *Phys. Rev. Lett.*, 38:1440–1443, 1977. [doi]. [,328(1977)].

[8] R. D. Peccei and Helen R. Quinn. Constraints Imposed by CP Conservation in the Presence of Instantons. *Phys. Rev.*, D16:1791–1797, 1977. [doi].

[9] Steven Weinberg. A New Light Boson? *Phys. Rev. Lett.*, 40:223–226, 1978. [doi].

[10] Frank Wilczek. Problem of Strong P and T Invariance in the Presence of Instantons. *Phys. Rev. Lett.*, 40:279–282, 1978. [doi].

[11] A. Ringwald. Axions and Axion-Like Particles. In *Proceedings, 49th Rencontres de Moriond on Electroweak Interactions and Unified Theories: La Thuile, Italy, March 15-22, 2014*, pages 223–230, 2014.

[12] Hans Peter Nilles and Stuart Raby. Supersymmetry and the strong CP problem. *Nucl. Phys.*, B198:102–112, 1982. [doi].

[13] Mark B. Wise, Howard Georgi, and Sheldon L. Glashow. SU(5) and the Invisible Axion. *Phys. Rev. Lett.*, 47:402, 1981. [doi].

[14] Edward Witten. Some Properties of O(32) Superstrings. *Phys. Lett.*, 149B:351–356, 1984. [doi].

[15] Joseph P. Conlon. The QCD axion and moduli stabilisation. *JHEP*, 05:078, 2006. [doi].

[16] A. A. Anselm and N. G. Uraltsev. A SECOND MASSLESS AXION? *Phys. Lett.*, 114B:39–41, 1982. [doi].

[17] G. G. Raffelt. *Stars as laboratories for fundamental physics*. 1996. ISBN 9780226702728. URL `http://wwwth.mpp.mpg.de/members/raffelt/mypapers/199613.pdf`.

[18] Georg G. Raffelt. Astrophysical axion bounds. *Lect. Notes Phys.*, 741:51–71, 2008. [doi]. [,51(2006)].

[19] Maria Archidiacono, Tobias Basse, Jan Hamann, Steen Hannestad, Georg Raffelt, and Yvonne Y. Y. Wong. Future cosmological sensitivity for hot dark matter axions. *JCAP*, 1505(05):050, 2015. [doi].

[20] J. E. Moody and Frank Wilczek. NEW MACROSCOPIC FORCES? *Phys. Rev.*, D30:130, 1984. [doi].

[21] Javier Redondo and Andreas Ringwald. Light shining through walls. *Contemp. Phys.*, 52:211–236, 2011. [doi].

[22] P. Sikivie. Experimental Tests of the Invisible Axion. *Phys. Rev. Lett.*, 51:1415–1417, 1983. [doi]. [,321(1983)].

[23] John Preskill, Mark B. Wise, and Frank Wilczek. Cosmology of the Invisible Axion. *Phys. Lett.*, 120B:127–132, 1983. [doi].

[24] Michael Dine and Willy Fischler. The Not So Harmless Axion. *Phys. Lett.*, 120B:137–141, 1983. [doi].

[25] L. F. Abbott and P. Sikivie. A Cosmological Bound on the Invisible Axion. *Phys. Lett.*, 120B:133–136, 1983. [doi].

[26] Richard Lynn Davis. Cosmic Axions from Cosmic Strings. *Phys. Lett.*, B180:225–230, 1986. [doi].

[27] David H. Lyth. Estimates of the cosmological axion density. *Phys. Lett.*, B275:279–283, 1992. [doi].

[28] David J. E. Marsh. Axions and ALPs: a very short introduction. In *Proceedings, 13th Patras Workshop on Axions, WIMPs and WISPs, (PATRAS 2017): Thessaloniki, Greece, 15 May 2017 - 19, 2017*, pages 59–74, 2018. [doi].

[29] R. J. Crewther, P. Di Vecchia, G. Veneziano, and Edward Witten. Chiral Estimate of the Electric Dipole Moment of the Neutron in Quantum Chromodynamics. *Phys. Lett.*, 88B:123, 1979. [doi]. [Erratum: Phys. Lett.91B,487(1980)].

[30] J. M. Pendlebury et al. Revised experimental upper limit on the electric dipole moment of the neutron. *Phys. Rev.*, D92(9):092003, 2015. [doi].

[31] Brian D. Fields, Paolo Molaro, and Subir Sarkar. Big-Bang Nucleosynthesis. *Chin. Phys.*, C38:339–344, 2014.

[32] David J. E. Marsh. Axion Cosmology. *Phys. Rept.*, 643:1–79, 2016. [doi].

[33] Gerard 't Hooft. Symmetry Breaking Through Bell-Jackiw Anomalies. *Phys. Rev. Lett.*, 37:8–11, 1976. [doi]. [,226(1976)].

[34] Gerard 't Hooft. Computation of the Quantum Effects Due to a Four-Dimensional Pseudoparticle. *Phys. Rev.*, D14:3432–3450, 1976. [doi]. [,70(1976)].

[35] Michael Dine, Willy Fischler, and Mark Srednicki. A Simple Solution to the Strong CP Problem with a Harmless Axion. *Phys. Lett.*, 104B: 199–202, 1981. [doi].

[36] Paul J. Steinhardt and Michael S. Turner. Saving the Invisible Axion. *Phys. Lett.*, 129B:51, 1983. [doi].

[37] Michael S. Turner, Frank Wilczek, and A. Zee. Formation of Structure in an Axion Dominated Universe. *Phys. Lett.*, 125B:35, 1983. [doi]. [Erratum: Phys. Lett.125B,519(1983)].

[38] Michael S. Turner. Cosmic and Local Mass Density of Invisible Axions. *Phys. Rev.*, D33:889–896, 1986. [doi].

[39] David J. E. Marsh and Pedro G. Ferreira. Ultra-Light Scalar Fields and the Growth of Structure in the Universe. *Phys. Rev.*, D82:103528, 2010. [doi].

[40] Dieter Horns, Joerg Jaeckel, Axel Lindner, Andrei Lobanov, Javier Redondo, and Andreas Ringwald. Searching for WISPy Cold Dark Matter with a Dish Antenna. *JCAP*, 1304:016, 2013. [doi].

[41] Dmitry Budker, Peter W. Graham, Micah Ledbetter, Surjeet Rajendran, and Alex Sushkov. Proposal for a Cosmic Axion Spin Precession Experiment (CASPEr). *Phys. Rev.*, X4(2):021030, 2014. [doi].

[42] William DeRocco and Anson Hook. Axion interferometry. *Phys. Rev.*, D98(3):035021, 2018. [doi].

[43] Marco Farina, Duccio Pappadopulo, Fabrizio Rompineve, and Andrea Tesi. The photo-philic QCD axion. *JHEP*, 01:095, 2017. [doi].

[44] Prateek Agrawal, JiJi Fan, Matthew Reece, and Lian-Tao Wang. Experimental Targets for Photon Couplings of the QCD Axion. *JHEP*, 02:006, 2018. [doi].

[45] Wayne Hu, Rennan Barkana, and Andrei Gruzinov. Cold and fuzzy dark matter. *Phys. Rev. Lett.*, 85:1158–1161, 2000. [doi].

[46] Augusto Barroso and Gustavo C. Branco. CONSTRAINTS ON LIGHT AXIONS. *Phys. Lett.*, 116B:247–250, 1982. [doi].

[47] Richard Lynn Davis. Goldstone Bosons in String Models of Galaxy Formation. *Phys. Rev.*, D32:3172, 1985. [doi].

[48] Diego Harari and P. Sikivie. On the Evolution of Global Strings in the Early Universe. *Phys. Lett.*, B195:361–365, 1987. [doi].

[49] Alexander Vilenkin and Tanmay Vachaspati. Radiation of Goldstone Bosons From Cosmic Strings. *Phys. Rev.*, D35:1138, 1987. [doi].

[50] R. L. Davis and E. P. S. Shellard. DO AXIONS NEED INFLATION? *Nucl. Phys.*, B324:167–186, 1989. [doi].

[51] Atish Dabholkar and Jean M. Quashnock. Pinning Down the Axion. *Nucl. Phys.*, B333:815–832, 1990. [doi].

[52] R. A. Battye and E. P. S. Shellard. Global string radiation. *Nucl. Phys.*, B423:260–304, 1994. [doi].

[53] R. A. Battye and E. P. S. Shellard. Axion string constraints. *Phys. Rev. Lett.*, 73:2954–2957, 1994. [doi]. [Erratum: Phys. Rev. Lett.76,2203(1996)].

[54] Masahide Yamaguchi, M. Kawasaki, and Jun'ichi Yokoyama. Evolution of axionic strings and spectrum of axions radiated from them. *Phys. Rev. Lett.*, 82:4578–4581, 1999. [doi].

[55] C. Hagmann, Sanghyeon Chang, and P. Sikivie. Axion radiation from strings. *Phys. Rev.*, D63:125018, 2001. [doi].

[56] Sanghyeon Chang, C. Hagmann, and P. Sikivie. Studies of the motion and decay of axion walls bounded by strings. *Phys. Rev.*, D59:023505, 1999. [doi].

[57] Michiyasu Nagasawa and Masahiro Kawasaki. Collapse of axionic domain wall and axion emission. *Phys. Rev.*, D50:4821–4826, 1994. [doi].

[58] Leanne D. Duffy and Karl van Bibber. Axions as Dark Matter Particles. *New J. Phys.*, 11:105008, 2009. [doi].

[59] Nataliya K. Porayko et al. Parkes Pulsar Timing Array constraints on ultralight scalar-field dark matter. *Phys. Rev.*, D98(10):102002, 2018. [doi].

[60] N. Du et al. A Search for Invisible Axion Dark Matter with the Axion Dark Matter Experiment. *Phys. Rev. Lett.*, 120(15):151301, 2018. [doi].

[61] C. Boutan et al. Piezoelectrically Tuned Multimode Cavity Search for Axion Dark Matter. *Phys. Rev. Lett.*, 121(26):261302, 2018. [doi].

[62] B. M. Brubaker, L. Zhong, S. K. Lamoreaux, K. W. Lehnert, and K. A. van Bibber. HAYSTAC axion search analysis procedure. *Phys. Rev.*, D96(12):123008, 2017. [doi].

[63] L. Zhong, B. M. Brubaker, S. B. Cahn, and S. K. Lamoreaux. Recent Technical Improvements to the HAYSTAC Experiment. *Springer Proc. Phys.*, 211:105–109, 2018. [doi].

[64] S. Al Kenany et al. Design and operational experience of a microwave cavity axion detector for the 20–100 μeV range. *Nucl. Instrum. Meth.*, A854:11–24, 2017. [doi].

[65] B. M. Brubaker et al. First results from a microwave cavity axion search at 24 μeV. *Phys. Rev. Lett.*, 118(6):061302, 2017. [doi].

[66] L. Zhong et al. Results from phase 1 of the HAYSTAC microwave cavity axion experiment. *Phys. Rev.*, D97(9):092001, 2018. [doi].

[67] Makoto Minowa. Tokyo Axion Helioscope. *AIP Conf. Proc.*, 1274(1): 133–137, 2010. [doi].

[68] S. Andriamonje et al. An Improved limit on the axion-photon coupling from the CAST experiment. *JCAP*, 0704:010, 2007. [doi].

[69] E. Arik et al. Probing eV-scale axions with CAST. *JCAP*, 0902:008, 2009. [doi].

[70] S. Andriamonje et al. Search for 14.4-keV solar axions emitted in the M1-transition of Fe-57 nuclei with CAST. *JCAP*, 0912:002, 2009. [doi].

[71] S. Andriamonje et al. Search for solar axion emission from ^7Li and $D(p,\gamma)^3He$ nuclear decays with the CAST γ-ray calorimeter. *JCAP*, 1003:032, 2010. [doi].

[72] S. Aune et al. CAST search for sub-eV mass solar axions with 3He buffer gas. *Phys. Rev. Lett.*, 107:261302, 2011. [doi].

[73] K. Barth et al. CAST constraints on the axion-electron coupling. *JCAP*, 1305:010, 2013. [doi].

[74] M. Arik et al. Search for Solar Axions by the CERN Axion Solar Telescope with ^{3}He Buffer Gas: Closing the Hot Dark Matter Gap. *Phys. Rev. Lett.*, 112(9):091302, 2014. [doi].

[75] M. Arik, S. Aune, K. Barth, A. Belov, H. Bräuninger, J. Bremer, V. Burwitz, G. Cantatore, J. M. Carmona, S. A. Cetin, J. I. Collar, E. Da Riva, T. Dafni, M. Davenport, A. Dermenev, C. Eleftheriadis, N. Elias, G. Fanourakis, E. Ferrer-Ribas, J. Galán, J. A.

García, A. Gardikiotis, J. G. Garza, E. N. Gazis, T. Geralis, E. Georgiopoulou, I. Giomataris, S. Gninenko, M. Gómez Marzoa, M. D. Hasinoff, D. H. H. Hoffmann, F. J. Iguaz, I. G. Irastorza, J. Jacoby, K. Jakov***v***cić, M. Karuza, M. Kavuk, M. Kr***v***cmar, M. Kuster, B. Lakić, J. M. Laurent, A. Liolios, A. Ljubi***v***cić, G. Luzón, S. Neff, T. Niinikoski, A. Nordt, I. Ortega, T. Papaevangelou, M. J. Pivovaroff, G. Raffelt, A. Rodríguez, M. Rosu, J. Ruz, I. Savvidis, I. Shilon, S. K. Solanki, L. Stewart, A. Tomás, T. Vafeiadis, J. Villar, J. K. Vogel, S. C. Yildiz, and K. Zioutas. New solar axion search using the cern axion solar telescope with ^{4}He filling. *Phys. Rev. D*, 92:021101, Jul 2015. [doi]. URL https://link.aps.org/doi/10.1103/PhysRevD.92.021101.

[76] V. Anastassopoulos et al. New CAST Limit on the Axion-Photon Interaction. *Nature Phys.*, 13:584–590, 2017. [doi].

[77] K. Zioutas et al. First results from the CERN Axion Solar Telescope (CAST). *Phys. Rev. Lett.*, 94:121301, 2005. [doi].

[78] I. G. Irastorza et al. Towards a new generation axion helioscope. *JCAP*, 1106:013, 2011. [doi].

[79] E. Armengaud et al. Conceptual Design of the International Axion Observatory (IAXO). *JINST*, 9:T05002, 2014. [doi].

[80] Theopisti Dafni, Ciaran A. J. O'Hare, Biljana Lakić, Javier Galán, Francisco J. Iguaz, Igor G. Irastorza, Kre ***v***simir Jakov***v***cić, Gloria Luzón, Javier Redondo, and Elisa Ruiz Chóliz. Weighing the solar axion. *Phys. Rev. D*, 99:035037, Feb 2019. [doi]. URL https://link.aps.org/doi/10.1103/PhysRevD.99.035037.

[81] E. Armengaud et al. Physics potential of the International Axion Observatory (IAXO). *JCAP*, 1906(06):047, 2019. [doi].

[82] R. J. Gaitskell. Direct detection of dark matter. *Ann. Rev. Nucl. Part. Sci.*, 54:315–359, 2004. [doi].

[83] J. Angle et al. First Results from the XENON10 Dark Matter Experiment at the Gran Sasso National Laboratory. *Phys. Rev. Lett.*, 100:021303, 2008. [doi].

[84] E. Aprile et al. First Axion Results from the XENON100 Experiment. *Phys. Rev.*, D90(6):062009, 2014. [doi]. [Erratum: Phys. Rev.D95,no.2,029904(2017)].

[85] D. S. Akerib et al. The Large Underground Xenon (LUX) Experiment. *Nucl. Instrum. Meth.*, A704:111–126, 2013. [doi].

[86] D. S. Akerib et al. First Searches for Axions and Axionlike Particles with the LUX Experiment. *Phys. Rev. Lett.*, 118(26):261301, 2017. [doi].

[87] Klaus Ehret et al. Resonant laser power build-up in ALPS: A 'Light-shining-through-walls' experiment. *Nucl. Instrum. Meth.*, A612:83–96, 2009. [doi].

[88] Klaus Ehret, Maik Frede, Samvel Ghazaryan, Matthias Hildebrandt, Ernst-Axel Knabbe, Dietmar Kracht, Axel Lindner, Jenny List, Tobias Meier, Niels Meyer, Dieter Notz, Javier Redondo, Andreas Ringwald, Günter Wiedemann, and Benno Willke. New alps results on hidden-sector lightweights. *Physics Letters B*, 689(4):149 – 155, 2010. ISSN 0370-2693. [doi]. URL http://www.sciencedirect.com/science/article/pii/S0370269310005526.

[89] K. Baker et al. The quest for axions and other new light particles. *Annalen Phys.*, 525:A93–A99, 2013. [doi].

[90] Dieter Horns, Axel Lindner, Andrei Lobanov, and Andreas Ringwald. WISPers from the Dark Side: Radio Probes of Axions and Hidden Photons. In *Proceedings, 9th Patras Workshop on Axions, WIMPs and WISPs (AXION-WIMP 2013): Mainz, Germany, June 24-28, 2013*, pages 81–84, 2013. [doi].

[91] S. Borsanyi, M. Dierigl, Z. Fodor, S. D. Katz, S. W. Mages, D. Nogradi, J. Redondo, A. Ringwald, and K. K. Szabo. Axion cosmology, lattice QCD and the dilute instanton gas. *Phys. Lett.*, B752:175–181, 2016. [doi].

[92] Andreas Ringwald and Ken'ichi Saikawa. Axion dark matter in the post-inflationary Peccei-Quinn symmetry breaking scenario. *Phys. Rev.*, D93(8):085031, 2016. [doi]. [Addendum: Phys. Rev.D94,no.4,049908(2016)].

[93] Maurizio Giannotti, Igor Irastorza, Javier Redondo, and Andreas Ringwald. Cool WISPs for stellar cooling excesses. *JCAP*, 1605(05): 057, 2016. [doi].

[94] Peter W. Graham, Igor G. Irastorza, Steven K. Lamoreaux, Axel Lindner, and Karl A. van Bibber. Experimental Searches for the Axion and Axion-Like Particles. *Ann. Rev. Nucl. Part. Sci.*, 65:485–514, 2015. [doi].

[95] Andrei Khmelnitsky and Valery Rubakov. Pulsar timing signal from ultralight scalar dark matter. *JCAP*, 1402:019, 2014. [doi].

[96] R N Manchester. The Parkes Pulsar Timing Array. *Submitted to: Chin. J. Astron. Astrophys.*, 2006. [Chin. J. Astron. Astrophys. Suppl.6,02139(2006)].

[97] RENDONG NAN, DI LI, CHENGJIN JIN, QIMING WANG, LICHUN ZHU, WENBAI ZHU, HAIYAN ZHANG, YOULING YUE, and LEI QIAN. The five-hundred-meter aperture spherical radio telescope (fast) project. *International Journal of Modern Physics D*, 20(06):989–1024, Jun 2011. ISSN 1793-6594. [doi]. URL http://dx.doi.org/10.1142/S0218271811019335.

[98] Pau Amaro-Seoane et al. eLISA/NGO: Astrophysics and cosmology in the gravitational-wave millihertz regime. *GW Notes*, 6:4–110, 2013.

[99] Arata Aoki and Jiro Soda. Detecting ultralight axion dark matter wind with laser interferometers. *Int. J. Mod. Phys.*, D26(07):1750063, 2016. [doi].

[100] Asimina Arvanitaki, Masha Baryakhtar, and Xinlu Huang. Discovering the QCD Axion with Black Holes and Gravitational Waves. *Phys. Rev.*, D91(8):084011, 2015. [doi].

[101] Richard Brito, Vitor Cardoso, and Paolo Pani. Superradiance. *Lect. Notes Phys.*, 906:pp.1–237, 2015. [doi].

[102] Hirotaka Yoshino and Hideo Kodama. Bosenova collapse of axion cloud around a rotating black hole. *Prog. Theor. Phys.*, 128:153–190, 2012. [doi].

[103] Cari Powell. Multi-Field Evolution during Cosmological Inflation. Master's thesis, Swansea University, Singleton Campus, Swansea University, Swansea, SA2 8PP, 6 2016.

[104] Vincent Vennin. *Cosmological Inflation: Theoretical Aspects and Observational Constraints*. PhD thesis, Paris, Inst. Astrophys., 2014. URL https://tel.archives-ouvertes.fr/tel-01094199.

[105] Sean M. Carroll. *Spacetime and Geometry*. Cambridge University Press, 2019. ISBN 0805387323, 9780805387322, 9781108488396, 9781108775557. URL http://www.slac.stanford.edu/spires/find/books/www?cl=QC6:C37:2004.

[106] M. P. Hobson, G. P. Efstathiou, and A. N. Lasenby. *General relativity: An introduction for physicists*. 2006.

[107] Alan H. Guth. *The inflationary universe: The quest for a new theory of cosmic origins*. 1997.

[108] Andrew R. Liddle. An Introduction to cosmological inflation. In *Proceedings, Summer School in High-energy physics and cosmology: Trieste, Italy, June 29-July 17, 1998*, pages 260–295, 1999.

[109] Edward W. Kolb and Michael S. Turner. The Early Universe. *Front. Phys.*, 69:1–547, 1990.

[110] C. B. Collins and S. W. Hawking. Why is the Universe isotropic? *Astrophys. J.*, 180:317–334, 1973. [doi].

[111] Daniel Baumann. The physics of inflation. 2011.

[112] Mark Trodden and Sean M. Carroll. TASI lectures: Introduction to cosmology. In *Progress in string theory. Proceedings, Summer School, TASI 2003, Boulder, USA, June 2-27, 2003*, pages 703–793, 2004. [,703(2004)].

[113] Cornell university astrophysics lecture notes. wmap - values of the density parameters. Accessed: 2016-05-05.

[114] P. A. R. Ade et al. Planck 2013 results. XVI. Cosmological parameters. *Astron. Astrophys.*, 571:A16, 2014. [doi].

[115] P. A. R. Ade et al. Planck 2013 results. XXII. Constraints on inflation. *Astron. Astrophys.*, 571:A22, 2014. [doi].

[116] P. A. R. Ade et al. Planck 2015 results. XIII. Cosmological parameters. *Astron. Astrophys.*, 594:A13, 2016. [doi].

[117] P. A. R. Ade et al. Planck 2015 results. XX. Constraints on inflation. *Astron. Astrophys.*, 594:A20, 2016. [doi].

[118] Nils Fischer Oscar Garcia. QFT in Curved Spacetime: Introducing Inflation., May 2015.

[119] Scott Dodelson. *Modern Cosmology*. Academic Press, Amsterdam, 2003. ISBN 9780122191411. URL `http://www.slac.stanford.edu/spires/find/books/www?cl=QB981:D62:2003`.

[120] David Langlois. Inflation, quantum fluctuations and cosmological perturbations. In *Particle physics and cosmology: The interface. Proceedings, NATO Advanced Study Institute, School, Cargese, France, August 4-16, 2003*, pages 235–278, 2004.

[121] Daniel Baumann and Hiranya V. Peiris. Cosmological Inflation: Theory and Observations. *Adv. Sci. Lett.*, 2:105–120, 2009. [doi].

[122] M. C. Guzzetti, N. Bartolo, M. Liguori, and S. Matarrese. Gravitational waves from inflation. *Riv. Nuovo Cim.*, 39(9):399–495, 2016. [doi].

[123] Maria Mylova, Ogan Özsoy, Susha Parameswaran, Gianmassimo Tasinato, and Ivonne Zavala. A new mechanism to enhance primordial tensor fluctuations in single field inflation. *JCAP*, 1812(12):024, 2018. [doi].

[124] Dmitry S. Gorbunov and Valery A. Rubakov. *Introduction to the theory of the early universe: Cosmological perturbations and inflationary theory*. 2011. [doi]. URL `http://www.DESY.eblib.com/patron/FullRecord.aspx?p=737613`.

[125] G. Hobbs, F. Jenet, K. J. Lee, J. P. W. Verbiest, D. Yardley, R. Manchester, A. Lommen, W. Coles, R. Edwards, and C. Shettigara. TEMPO2, a new pulsar timing package. III: Gravitational wave simulation. *Mon. Not. Roy. Astron. Soc.*, 394:1945, 2009. [doi].

[126] Lam Hui, Jeremiah P. Ostriker, Scott Tremaine, and Edward Witten. Ultralight scalars as cosmological dark matter. *Phys. Rev.*, D95(4): 043541, 2017. [doi].

[127] Christopher Eling, Ted Jacobson, and David Mattingly. Einstein-Aether theory. In *Deserfest: A celebration of the life and works of Stanley Deser. Proceedings, Meeting, Ann Arbor, USA, April 3-5, 2004*, pages 163–179, 2004.

[128] Peter Adshead, Diego Blas, C. P. Burgess, Peter Hayman, and Subodh P Patil. Magnon Inflation: Slow Roll with Steep Potentials. *JCAP*, 1611(11):009, 2016. [doi].

[129] Jessica L. Cook and Lorenzo Sorbo. Particle production during inflation and gravitational waves detectable by ground-based interferometers. *Phys. Rev.*, D85:023534, 2012. [doi]. [Erratum: Phys. Rev.D86,069901(2012)].

[130] Leonardo Senatore, Eva Silverstein, and Matias Zaldarriaga. New Sources of Gravitational Waves during Inflation. *JCAP*, 1408:016, 2014. [doi].

[131] Daniel Carney, Willy Fischler, Ely D. Kovetz, Dustin Lorshbough, and Sonia Paban. Rapid field excursions and the inflationary tensor spectrum. *JHEP*, 11:042, 2012. [doi].

[132] Matteo Biagetti, Matteo Fasiello, and Antonio Riotto. Enhancing Inflationary Tensor Modes through Spectator Fields. *Phys. Rev.*, D88:103518, 2013. [doi].

[133] Matteo Biagetti, Emanuela Dimastrogiovanni, Matteo Fasiello, and Marco Peloso. Gravitational Waves and Scalar Perturbations from Spectator Fields. *JCAP*, 1504:011, 2015. [doi].

[134] Cody Goolsby-Cole and Lorenzo Sorbo. Nonperturbative production of massless scalars during inflation and generation of gravitational waves. *JCAP*, 1708(08):005, 2017. [doi].

[135] Lorenzo Sorbo. Parity violation in the Cosmic Microwave Background from a pseudoscalar inflaton. *JCAP*, 1106:003, 2011. [doi].

[136] Mohamed M. Anber and Lorenzo Sorbo. Non-Gaussianities and chiral gravitational waves in natural steep inflation. *Phys. Rev.*, D85: 123537, 2012. [doi].

[137] Neil Barnaby and Marco Peloso. Large Nongaussianity in Axion Inflation. *Phys. Rev. Lett.*, 106:181301, 2011. [doi].

[138] Neil Barnaby, Jordan Moxon, Ryo Namba, Marco Peloso, Gary Shiu, and Peng Zhou. Gravity waves and non-Gaussian features from particle production in a sector gravitationally coupled to the inflaton. *Phys. Rev.*, D86:103508, 2012. [doi].

[139] Ogan Ozsoy. On Synthetic Gravitational Waves from Multi-field Inflation. *JCAP*, 1804(04):062, 2018. [doi].

[140] A. Maleknejad and M. M. Sheikh-Jabbari. Gauge-flation: Inflation From Non-Abelian Gauge Fields. *Phys. Lett.*, B723:224–228, 2013. [doi].

[141] Emanuela Dimastrogiovanni and Marco Peloso. Stability analysis of chromo-natural inflation and possible evasion of Lyth's bound. *Phys. Rev.*, D87(10):103501, 2013. [doi].

[142] Peter Adshead, Emil Martinec, and Mark Wyman. Gauge fields and inflation: Chiral gravitational waves, fluctuations, and the Lyth bound. *Phys. Rev.*, D88(2):021302, 2013. [doi].

[143] Peter Adshead, Emil Martinec, and Mark Wyman. Perturbations in Chromo-Natural Inflation. *JHEP*, 09:087, 2013. [doi].

[144] Ippei Obata, Takashi Miura, and Jiro Soda. Chromo-Natural Inflation in the Axiverse. *Phys. Rev.*, D92(6):063516, 2015. [doi]. [Addendum: Phys. Rev.D95,no.10,109902(2017)].

[145] Azadeh Maleknejad. Axion Inflation with an SU(2) Gauge Field: Detectable Chiral Gravity Waves. *JHEP*, 07:104, 2016. [doi].

[146] Emanuela Dimastrogiovanni, Matteo Fasiello, and Tomohiro Fujita. Primordial Gravitational Waves from Axion-Gauge Fields Dynamics. *JCAP*, 1701(01):019, 2017. [doi].

[147] Aniket Agrawal, Tomohiro Fujita, and Eiichiro Komatsu. Large tensor non-Gaussianity from axion-gauge field dynamics. *Phys. Rev.*, D97(10):103526, 2018. [doi].

[148] Peter Adshead and Evangelos I. Sfakianakis. Higgsed Gauge-flation. *JHEP*, 08:130, 2017. [doi].

[149] R. R. Caldwell and C. Devulder. Axion Gauge Field Inflation and Gravitational Leptogenesis: A Lower Bound on B Modes from the Matter-Antimatter Asymmetry of the Universe. *Phys. Rev.*, D97(2): 023532, 2018. [doi].

[150] Aniket Agrawal, Tomohiro Fujita, and Eiichiro Komatsu. Tensor Non-Gaussianity from Axion-Gauge-Fields Dynamics : Parameter Search. *JCAP*, 1806(06):027, 2018. [doi].

[151] José Ramón Espinosa, Davide Racco, and Antonio Riotto. A Cosmological Signature of the SM Higgs Instability: Gravitational Waves. *JCAP*, 1809(09):012, 2018. [doi].

[152] Solomon Endlich, Alberto Nicolis, and Junpu Wang. Solid Inflation. *JCAP*, 1310:011, 2013. [doi].

[153] Nicola Bartolo, Dario Cannone, Angelo Ricciardone, and Gianmassimo Tasinato. Distinctive signatures of space-time diffeomorphism breaking in EFT of inflation. *JCAP*, 1603(03):044, 2016. [doi].

[154] Angelo Ricciardone and Gianmassimo Tasinato. Primordial gravitational waves in supersolid inflation. *Phys. Rev.*, D96(2):023508, 2017. [doi].

[155] Angelo Ricciardone and Gianmassimo Tasinato. Anisotropic tensor power spectrum at interferometer scales induced by tensor squeezed non-Gaussianity. *JCAP*, 1802(02):011, 2018. [doi].

[156] Guillem Domènech, Takashi Hiramatsu, Chunshan Lin, Misao Sasaki, Maresuke Shiraishi, and Yi Wang. CMB Scale Dependent Non-Gaussianity from Massive Gravity during Inflation. *JCAP*, 1705(05): 034, 2017. [doi].

[157] Guillermo Ballesteros, Denis Comelli, and Luigi Pilo. Massive and modified gravity as self-gravitating media. *Phys. Rev.*, D94(12): 124023, 2016. [doi].

[158] Dario Cannone, Jinn-Ouk Gong, and Gianmassimo Tasinato. Breaking discrete symmetries in the effective field theory of inflation. *JCAP*, 1508(08):003, 2015. [doi].

[159] Chunshan Lin and Lance Z. Labun. Effective Field Theory of Broken Spatial Diffeomorphisms. *JHEP*, 03:128, 2016. [doi].

[160] Dario Cannone, Gianmassimo Tasinato, and David Wands. Generalised tensor fluctuations and inflation. *JCAP*, 1501(01):029, 2015. [doi].

[161] Mohammad Akhshik. Clustering Fossils in Solid Inflation. *JCAP*, 1505(05):043, 2015. [doi].

[162] Matteo Biagetti, Emanuela Dimastrogiovanni, and Matteo Fasiello. Possible signatures of the inflationary particle content: spin-2 fields. *JCAP*, 1710(10):038, 2017. [doi].

[163] Emanuela Dimastrogiovanni, Matteo Fasiello, and Gianmassimo Tasinato. Probing the inflationary particle content: extra spin-2 field. *JCAP*, 1808(08):016, 2018. [doi].

[164] Tomohiro Fujita, Sachiko Kuroyanagi, Shuntaro Mizuno, and Shinji Mukohyama. Blue-tilted Primordial Gravitational Waves from Massive Gravity. *Phys. Lett.*, B789:215–219, 2019. [doi].

[165] Nicola Bartolo et al. Science with the space-based interferometer LISA. IV: Probing inflation with gravitational waves. *JCAP*, 1612 (12):026, 2016. [doi].

[166] Alexei A. Starobinsky. Spectrum of adiabatic perturbations in the universe when there are singularities in the inflation potential. *JETP Lett.*, 55:489–494, 1992. [Pisma Zh. Eksp. Teor. Fiz.55,477(1992)].

[167] Shogo Inoue and Jun'ichi Yokoyama. Curvature perturbation at the local extremum of the inflaton's potential. *Phys. Lett.*, B524:15–20, 2002. [doi].

[168] Andrei D. Linde. Fast roll inflation. *JHEP*, 11:052, 2001. [doi].

[169] William H. Kinney. Horizon crossing and inflation with large eta. *Phys. Rev.*, D72:023515, 2005. [doi].

[170] Jerome Martin, Hayato Motohashi, and Teruaki Suyama. Ultra Slow-Roll Inflation and the non-Gaussianity Consistency Relation. *Phys. Rev.*, D87(2):023514, 2013. [doi].

[171] Hayato Motohashi, Alexei A. Starobinsky, and Jun'ichi Yokoyama. Inflation with a constant rate of roll. *JCAP*, 1509:018, 2015. [doi].

[172] Zhu Yi and Yungui Gong. On the constant-roll inflation. *JCAP*, 1803 (03):052, 2018. [doi].

[173] Konstantinos Dimopoulos. Ultra slow-roll inflation demystified. *Phys. Lett.*, B775:262–265, 2017. [doi].

[174] Chris Pattison, Vincent Vennin, Hooshyar Assadullahi, and David Wands. The attractive behaviour of ultra-slow-roll inflation. *JCAP*, 1808(08):048, 2018. [doi].

[175] Juan García-Bellido. Massive Primordial Black Holes as Dark Matter and their detection with Gravitational Waves. *J. Phys. Conf. Ser.*, 840(1):012032, 2017. [doi].

[176] Misao Sasaki, Teruaki Suyama, Takahiro Tanaka, and Shuichiro Yokoyama. Primordial black holes—perspectives in gravitational wave astronomy. *Class. Quant. Grav.*, 35(6):063001, 2018. [doi].

[177] Bernard Carr, Florian Kuhnel, and Marit Sandstad. Primordial Black Holes as Dark Matter. *Phys. Rev.*, D94(8):083504, 2016. [doi].

[178] Ryo Saito, Jun'ichi Yokoyama, and Ryo Nagata. Single-field inflation, anomalous enhancement of superhorizon fluctuations, and non-Gaussianity in primordial black hole formation. *JCAP*, 0806:024, 2008. [doi].

[179] Juan Garcia-Bellido and Ester Ruiz Morales. Primordial black holes from single field models of inflation. *Phys. Dark Univ.*, 18:47–54, 2017. [doi].

[180] Cristiano Germani and Tomislav Prokopec. On primordial black holes from an inflection point. *Phys. Dark Univ.*, 18:6–10, 2017. [doi].

[181] Hayato Motohashi and Wayne Hu. Primordial Black Holes and Slow-Roll Violation. *Phys. Rev.*, D96(6):063503, 2017. [doi].

[182] Guillermo Ballesteros and Marco Taoso. Primordial black hole dark matter from single field inflation. *Phys. Rev.*, D97(2):023501, 2018. [doi].

[183] Jose Maria Ezquiaga, Juan Garcia-Bellido, and Ester Ruiz Morales. Primordial Black Hole production in Critical Higgs Inflation. *Phys. Lett.*, B776:345–349, 2018. [doi].

[184] Michele Cicoli, Victor A. Diaz, and Francisco G. Pedro. Primordial Black Holes from String Inflation. *JCAP*, 1806(06):034, 2018. [doi].

[185] Ogan Özsoy, Susha Parameswaran, Gianmassimo Tasinato, and Ivonne Zavala. Mechanisms for Primordial Black Hole Production in String Theory. *JCAP*, 1807:005, 2018. [doi].

[186] Matteo Biagetti, Gabriele Franciolini, Alex Kehagias, and Antonio Riotto. Primordial Black Holes from Inflation and Quantum Diffusion. *JCAP*, 1807(07):032, 2018. [doi].

[187] David Wands. Duality invariance of cosmological perturbation spectra. *Phys. Rev.*, D60:023507, 1999. [doi].

[188] Juan Martin Maldacena. Non-Gaussian features of primordial fluctuations in single field inflationary models. *JHEP*, 05:013, 2003. [doi].

[189] Juan M. Maldacena and Guilherme L. Pimentel. On graviton non-Gaussianities during inflation. *JHEP*, 09:045, 2011. [doi].

[190] Jiro Soda, Hideo Kodama, and Masato Nozawa. Parity Violation in Graviton Non-gaussianity. *JHEP*, 08:067, 2011. [doi].

[191] Maresuke Shiraishi, Daisuke Nitta, and Shuichiro Yokoyama. Parity Violation of Gravitons in the CMB Bispectrum. *Prog. Theor. Phys.*, 126:937–959, 2011. [doi].

[192] Nicola Bartolo and Giorgio Orlando. Parity breaking signatures from a Chern-Simons coupling during inflation: the case of non-Gaussian gravitational waves. *JCAP*, 1707:034, 2017. [doi].

[193] Tao Zhu, Wen Zhao, Yongqing Huang, Anzhong Wang, and Qiang Wu. Effects of parity violation on non-gaussianity of primordial gravitational waves in Ho***v***rava-Lifshitz gravity. *Phys. Rev.*, D88:063508, 2013. [doi].

[194] Yongqing Huang, Anzhong Wang, Razieh Yousefi, and Tao Zhu. Primordial non-Gaussianity of gravitational waves in Ho***v***rava-Lifshitz gravity. *Phys. Rev.*, D88(2):023523, 2013. [doi].

[195] Jessica L. Cook and Lorenzo Sorbo. An inflationary model with small scalar and large tensor nongaussianities. *JCAP*, 1311:047, 2013. [doi].

[196] Juan Garcia-Bellido, Marco Peloso, and Caner Unal. Gravitational Wave signatures of inflationary models from Primordial Black Hole Dark Matter. *JCAP*, 1709(09):013, 2017. [doi].

[197] N. Bartolo, V. De Luca, G. Franciolini, M. Peloso, D. Racco, and A. Riotto. Testing primordial black holes as dark matter with LISA. *Phys. Rev.*, D99(10):103521, 2019. [doi].

[198] N. Bartolo, V. De Luca, G. Franciolini, A. Lewis, M. Peloso, and A. Riotto. The Primordial Black Hole Dark Matter - LISA Serendipity. *Phys. Rev. Lett.*, 122(21):211301, 2019. [doi].

[199] Nicola Bartolo, Valerie Domcke, Daniel G. Figueroa, Juan Garcia-Bellido, Marco Peloso, Mauro Pieroni, Angelo Ricciardone, Mairi Sakellariadou, Lorenzo Sorbo, and Gianmassimo Tasinato. Probing non-Gaussian Stochastic Gravitational Wave Backgrounds with LISA. *JCAP*, 1811(11):034, 2018. [doi].

[200] Paolo Creminelli, Jérôme Gleyzes, Jorge Noreña, and Filippo Vernizzi. Resilience of the standard predictions for primordial tensor modes. *Phys. Rev. Lett.*, 113(23):231301, 2014. [doi].

[201] Daniel Baumann, Hayden Lee, and Guilherme L. Pimentel. High-Scale Inflation and the Tensor Tilt. *JHEP*, 01:101, 2016. [doi].

[202] Tsutomu Kobayashi, Masahide Yamaguchi, and Jun'ichi Yokoyama. Generalized G-inflation: Inflation with the most general second-order field equations. *Prog. Theor. Phys.*, 126:511–529, 2011. [doi].

[203] Fabio Finelli and Robert Brandenberger. On the generation of a scale invariant spectrum of adiabatic fluctuations in cosmological models with a contracting phase. *Phys. Rev.*, D65:103522, 2002. [doi].

[204] M. Gasperini and G. Veneziano. The Pre - big bang scenario in string cosmology. *Phys. Rept.*, 373:1–212, 2003. [doi].

[205] Steven Gratton, Justin Khoury, Paul J. Steinhardt, and Neil Turok. Conditions for generating scale-invariant density perturbations. *Phys. Rev.*, D69:103505, 2004. [doi].

[206] Latham A. Boyle, Paul J. Steinhardt, and Neil Turok. A New duality relating density perturbations in expanding and contracting Friedmann cosmologies. *Phys. Rev.*, D70:023504, 2004. [doi].

[207] Yun-Song Piao. On the dualities of primordial perturbation spectrums. *Phys. Lett.*, B606:245–250, 2005. [doi].

[208] Laura E. Allen and David Wands. Cosmological perturbations through a simple bounce. *Phys. Rev.*, D70:063515, 2004. [doi].

[209] Justin Khoury and Federico Piazza. Rapidly-Varying Speed of Sound, Scale Invariance and Non-Gaussian Signatures. *JCAP*, 0907:026, 2009. [doi].

[210] Justin Khoury and Godfrey E. J. Miller. Towards a Cosmological Dual to Inflation. *Phys. Rev.*, D84:023511, 2011. [doi].

[211] Tristan L. Smith, Marc Kamionkowski, and Asantha Cooray. Direct detection of the inflationary gravitational wave background. *Phys. Rev.*, D73:023504, 2006. [doi].

[212] Clare Burrage, Claudia de Rham, David Seery, and Andrew J. Tolley. Galileon inflation. *JCAP*, 1101:014, 2011. [doi].

[213] Tsutomu Kobayashi, Masahide Yamaguchi, and Jun'ichi Yokoyama. G-inflation: Inflation driven by the Galileon field. *Phys. Rev. Lett.*, 105:231302, 2010. [doi].

[214] Shin'ichi Hirano, Tsutomu Kobayashi, and Shuichiro Yokoyama. Ultra slow-roll G-inflation. *Phys. Rev.*, D94(10):103515, 2016. [doi].

[215] Xian Gao, Tsutomu Kobayashi, Masahide Yamaguchi, and Jun'ichi Yokoyama. Primordial non-Gaussianities of gravitational waves in

the most general single-field inflation model. *Phys. Rev. Lett.*, 107: 211301, 2011. [doi].

[216] Xian Gao, Tsutomu Kobayashi, Maresuke Shiraishi, Masahide Yamaguchi, Jun'ichi Yokoyama, and Shuichiro Yokoyama. Full bispectra from primordial scalar and tensor perturbations in the most general single-field inflation model. *PTEP*, 2013:053E03, 2013. [doi].

[217] Mohammad Hossein Namjoo, Hassan Firouzjahi, and Misao Sasaki. Violation of non-Gaussianity consistency relation in a single field inflationary model. *EPL*, 101(3):39001, 2013. [doi].

[218] Xingang Chen, Hassan Firouzjahi, Mohammad Hossein Namjoo, and Misao Sasaki. A Single Field Inflation Model with Large Local Non-Gaussianity. *EPL*, 102(5):59001, 2013. [doi].

[219] Qing-Guo Huang and Yi Wang. Large Local Non-Gaussianity from General Single-field Inflation. *JCAP*, 1306:035, 2013. [doi].

[220] Xingang Chen, Hassan Firouzjahi, Eiichiro Komatsu, Mohammad Hossein Namjoo, and Misao Sasaki. In-in and δN calculations of the bispectrum from non-attractor single-field inflation. *JCAP*, 1312: 039, 2013. [doi].

[221] Emanuela Dimastrogiovanni, Matteo Fasiello, Gianmassimo Tasinato, and David Wands. Tensor non-Gaussianities from Non-minimal Coupling to the Inflaton. *JCAP*, 1902:008, 2019. [doi].

[222] Garrett Goon, Kurt Hinterbichler, Austin Joyce, and Mark Trodden. Shapes of gravity: Tensor non-Gaussianity and massive spin-2 fields. 2018.

[223] D. Anninos, V. De Luca, G. Franciolini, A. Kehagias, and A. Riotto. Cosmological Shapes of Higher-Spin Gravity. *JCAP*, 1904(04):045, 2019. [doi].

[224] Xingang Chen. Running non-Gaussianities in DBI inflation. *Phys. Rev.*, D72:123518, 2005. [doi].

[225] Christian T. Byrnes, Sami Nurmi, Gianmassimo Tasinato, and David Wands. Scale dependence of local $f_N L$. *JCAP*, 1002 : 034, 2010. [*doi*].

[226] Christian T. Byrnes, Mischa Gerstenlauer, Sami Nurmi, Gianmassimo Tasinato, and David Wands. Scale-dependent non-Gaussianity probes inflationary physics. *JCAP*, 1010:004, 2010. [doi].

[227] Daniel Babich, Paolo Creminelli, and Matias Zaldarriaga. The Shape of non-Gaussianities. *JCAP*, 0408:009, 2004. [doi].

[228] Bruce Allen and Adrian C. Ottewill. Detection of anisotropies in the gravitational wave stochastic background. *Phys. Rev.*, D56:545–563, 1997. [doi].

[229] Steven B. Giddings and Martin S. Sloth. Semiclassical relations and IR effects in de Sitter and slow-roll space-times. *JCAP*, 1101:023, 2011. [doi].

[230] Mischa Gerstenlauer, Arthur Hebecker, and Gianmassimo Tasinato. Inflationary Correlation Functions without Infrared Divergences. *JCAP*, 1106:021, 2011. [doi].

[231] Liang Dai, Donghui Jeong, and Marc Kamionkowski. Anisotropic imprint of long-wavelength tensor perturbations on cosmic structure. *Phys. Rev.*, D88(4):043507, 2013. [doi].

[232] Emanuela Dimastrogiovanni, Matteo Fasiello, Donghui Jeong, and Marc Kamionkowski. Inflationary tensor fossils in large-scale structure. *JCAP*, 1412:050, 2014. [doi].

[233] Lorenzo Bordin, Paolo Creminelli, Mehrdad Mirbabayi, and Jorge Noreña. Tensor Squeezed Limits and the Higuchi Bound. *JCAP*, 1609(09):041, 2016. [doi].

[234] Ben Thorne, Tomohiro Fujita, Masashi Hazumi, Nobuhiko Katayama, Eiichiro Komatsu, and Maresuke Shiraishi. Finding the chiral gravitational wave background of an axion-SU(2) inflationary model using CMB observations and laser interferometers. *Phys. Rev.*, D97(4):043506, 2018. [doi].

[235] Michele Maggiore. Gravitational wave experiments and early universe cosmology. *Phys. Rept.*, 331:283–367, 2000. [doi].

[236] Michele Maggiore. *Gravitational Waves. Vol. 1: Theory and Experiments*. Oxford Master Series in Physics. Oxford University Press, 2007. ISBN 9780198570745, 9780198520740. URL http://www.oup.com/uk/catalogue/?ci=9780198570745.

[237] Miguel Zumalacárregui and Juan García-Bellido. Transforming gravity: from derivative couplings to matter to second-order scalar-tensor theories beyond the Horndeski Lagrangian. *Phys. Rev.*, D89:064046, 2014. [doi].

[238] Jérôme Gleyzes, David Langlois, Federico Piazza, and Filippo Vernizzi. Healthy theories beyond Horndeski. *Phys. Rev. Lett.*, 114 (21):211101, 2015. [doi].

[239] David Langlois and Karim Noui. Degenerate higher derivative theories beyond Horndeski: evading the Ostrogradski instability. *JCAP*, 1602(02):034, 2016. [doi].

[240] Marco Crisostomi, Kazuya Koyama, and Gianmassimo Tasinato. Extended Scalar-Tensor Theories of Gravity. *JCAP*, 1604(04):044, 2016. [doi].

[241] Jibril Ben Achour, Marco Crisostomi, Kazuya Koyama, David Langlois, Karim Noui, and Gianmassimo Tasinato. Degenerate higher order scalar-tensor theories beyond Horndeski up to cubic order. *JHEP*, 12:100, 2016. [doi].

[242] Bruce Allen. The Stochastic gravity wave background: Sources and detection. In *Relativistic gravitation and gravitational radiation. Proceedings, School of Physics, Les Houches, France, September 26-October 6, 1995*, pages 373–417, 1996.

[243] Michele Maggiore. *Gravitational Waves. Vol. 2: Astrophysics and Cosmology*. Oxford University Press, 2018. ISBN 9780198570899.

[244] Chiara Caprini and Daniel G. Figueroa. Cosmological Backgrounds of Gravitational Waves. *Class. Quant. Grav.*, 35(16):163001, 2018. [doi].

[245] Tania Regimbau. The astrophysical gravitational wave stochastic background. *Res. Astron. Astrophys.*, 11:369–390, 2011. [doi].

[246] Chiara Caprini, Daniel G. Figueroa, Raphael Flauger, Germano Nardini, Marco Peloso, Mauro Pieroni, Angelo Ricciardone, and Gianmassimo Tasinato. Reconstructing the spectral shape of a stochastic gravitational wave background with LISA. 2019.

[247] Steve Drasco and Eanna E. Flanagan. Detection methods for non-Gaussian gravitational wave stochastic backgrounds. *Phys. Rev.*, D67:082003, 2003. [doi].

[248] Naoki Seto. Non-Gaussianity analysis of GW background made by short-duration burst signals. *Phys. Rev.*, D80:043003, 2009. [doi].

[249] Naoki Seto. Non-Gaussianity test for discriminating gravitational wave backgrounds around 0.1-1Hz. *Astrophys. J.*, 683:L95–L98, 2008. [doi].

[250] Etienne Racine and Curt Cutler. Gaussianity of LISA's confusion backgrounds. *Phys. Rev.*, D76:124033, 2007. [doi].

[251] Lionel Martellini and Tania Regimbau. Semiparametric approach to the detection of non-Gaussian gravitational wave stochastic backgrounds. *Phys. Rev.*, D89(12):124009, 2014. [doi].

[252] Peter Adshead and Eugene A. Lim. 3-pt Statistics of Cosmological Stochastic Gravitational Waves. *Phys. Rev.*, D82:024023, 2010. [doi].

[253] Emanuela Dimastrogiovanni, Matteo Fasiello, and Gianmassimo Tasinato. Searching for Fossil Fields in the Gravity Sector. 2019.

[254] N. Bartolo, D. Bertacca, S. Matarrese, M. Peloso, A. Ricciardone, A. Riotto, and G. Tasinato. Anisotropies and non-Gaussianity of the Cosmological Gravitational Wave Background. 2019.

[255] Michael Kramer and David J. Champion. The European Pulsar Timing Array and the Large European Array for Pulsars. *Class. Quant. Grav.*, 30:224009, 2013. [doi].

[256] Maura A. McLaughlin. The North American Nanohertz Observatory for Gravitational Waves. *Class. Quant. Grav.*, 30:224008, 2013. [doi].

[257] R. N. Manchester et al. The Parkes Pulsar Timing Array Project. *Publ. Astron. Soc. Austral.*, 30:17, 2013. [doi].

[258] J. P. W. Verbiest et al. The International Pulsar Timing Array: First Data Release. *Mon. Not. Roy. Astron. Soc.*, 458(2):1267–1288, 2016. [doi].

[259] Michael Kramer. Fundamental physics with the SKA: Strong-field tests of gravity using pulsars and black holes. 2004.

[260] R. w. Hellings and G. s. Downs. UPPER LIMITS ON THE ISOTROPIC GRAVITATIONAL RADIATION BACKGROUND FROM PULSAR TIMING ANALYSIS. *Astrophys. J.*, 265:L39–L42, 1983. [doi].

[261] Melissa Anholm, Stefan Ballmer, Jolien D. E. Creighton, Larry R. Price, and Xavier Siemens. Optimal strategies for gravitational wave stochastic background searches in pulsar timing data. *Phys. Rev.*, D79:084030, 2009. [doi].

[262] Gemma Janssen et al. Gravitational wave astronomy with the SKA. *PoS*, AASKA14:037, 2015. [doi].

[263] C. J. Moore, R. H. Cole, and C. P. L. Berry. Gravitational-wave sensitivity curves. *Class. Quant. Grav.*, 32(1):015014, 2015. [doi].

[264] Makoto Tsuneto, Asuka Ito, Toshifumi Noumi, and Jiro Soda. Searching for Bispectrum of Stochastic Gravitational Waves with Pulsar Timing Arrays. *JCAP*, 1903(03):032, 2019. [doi].

[265] NicolÃ¡s Yunes and Xavier Siemens. Gravitational-Wave Tests of General Relativity with Ground-Based Detectors and Pulsar Timing-Arrays. *Living Rev. Rel.*, 16:9, 2013. [doi].

[266] Sydney J. Chamberlin and Xavier Siemens. Stochastic backgrounds in alternative theories of gravity: overlap reduction functions for pulsar timing arrays. *Phys. Rev.*, D85:082001, 2012. [doi].

[267] Neil J. Cornish, Logan O'Beirne, Stephen R. Taylor, and NicolÃ¡s Yunes. Constraining alternative theories of gravity using pulsar timing arrays. *Phys. Rev. Lett.*, 120(18):181101, 2018. [doi].

[268] Bruce Allen and Joseph D. Romano. Detecting a stochastic background of gravitational radiation: Signal processing strategies and sensitivities. *Phys. Rev.*, D59:102001, 1999. [doi].

[269] Xingang Chen, Min-xin Huang, Shamit Kachru, and Gary Shiu. Observational signatures and non-Gaussianities of general single field inflation. *JCAP*, 0701:002, 2007. [doi].

[270] R. Holman and Andrew J. Tolley. Enhanced Non-Gaussianity from Excited Initial States. *JCAP*, 0805:001, 2008. [doi].

[271] Nicola Bartolo, Matteo Fasiello, Sabino Matarrese, and Antonio Riotto. Large non-Gaussianities in the Effective Field Theory Approach to Single-Field Inflation: the Bispectrum. *JCAP*, 1008:008, 2010. [doi].

[272] Sebastian Garcia-Saenz and Sébastien Renaux-Petel. Flattened non-Gaussianities from the effective field theory of inflation with imaginary speed of sound. *JCAP*, 1811(11):005, 2018. [doi].

[273] Steven Weinberg. Adiabatic modes in cosmology. *Phys. Rev.*, D67: 123504, 2003. [doi].

[274] Chiara Maria Francesca Mingarelli. *Gravitational wave astrophysics with pulsar timing arrays*. PhD thesis, Birmingham U., 2014. URL http://etheses.bham.ac.uk/5117/.

[275] D. M. Eardley, D. L. Lee, A. P. Lightman, R. V. Wagoner, and C. M. Will. Gravitational-wave observations as a tool for testing relativistic gravity. *Phys. Rev. Lett.*, 30:884–886, 1973. [doi].

[276] D. M. Eardley, D. L. Lee, and A. P. Lightman. Gravitational-wave observations as a tool for testing relativistic gravity. *Phys. Rev.*, D8: 3308–3321, 1973. [doi].

[277] Eric Thrane and Joseph D. Romano. Sensitivity curves for searches for gravitational-wave backgrounds. *Phys. Rev.*, D88(12):124032, 2013. [doi].

[278] Mathieu Isidro. On ligo, the hunt for gravitational waves and the ska. https://www.skatelescope.org/news/ligo-ska-gw/, February 2016.

[279] Michael Kramer and Ben Stappers. Pulsar Science with the SKA. *PoS*, AASKA14:036, 2015. [doi].

[280] Joseph D. Romano and Neil J. Cornish. Detection methods for stochastic gravitational-wave backgrounds: a unified treatment. *Living Rev. Rel.*, 20(1):2, 2017. [doi].

[281] Atsushi Nishizawa, Atsushi Taruya, Kazuhiro Hayama, Seiji Kawamura, and Masa-aki Sakagami. Probing non-tensorial polarizations

of stochastic gravitational-wave backgrounds with ground-based laser interferometers. *Phys. Rev.*, D79:082002, 2009. [doi].

[282] Fredrick A. Jenet and Joseph D. Romano. Understanding the gravitational-wave Hellings and Downs curve for pulsar timing arrays in terms of sound and electromagnetic waves. *Am. J. Phys.*, 83: 635, 2015. [doi].

[283] Steven Weinberg. Quantum contributions to cosmological correlations. *Phys. Rev.*, D72:043514, 2005. [doi].

[284] Guillem Domènech, Atsushi Naruko, and Misao Sasaki. Cosmological disformal invariance. *JCAP*, 1510(10):067, 2015. [doi].